STUDIES OF A XENON CHLORIDE LASER

By

ABDULHAKEM Y. ELEZZABI

B.Sc.(Hon.), Brock University, 1987

A THESIS SUBMITTED IN PARTIAL FULFILLMENT OF

THE REQUIREMENTS FOR THE DEGREE OF

MASTER OF SCIENCE

in

THE FACULTY OF GRADUATE STUDIES

PHYSICS

We accept this thesis as conforming

to the required standard

THE UNIVERSITY OF BRITISH COLUMBIA

September 1989

In presenting this thesis in partial fulfilment of the requirements for an advanced degree at the University of British Columbia, I agree that the Library shall make it freely available for reference and study. I further agree that permission for extensive copying of this thesis for scholarly purposes may be granted by the head of my department or by his or her representatives. It is understood that copying or publication of this thesis for financial gain shall not be allowed without my written permission.

Department of Physics

The University of British Columbia
Vancouver, Canada

Date Oct 4th 1989

ABSTRACT

A compact, transverse discharge $XeCl$ laser has been constructed. The laser employs an LC double inversion circuit, and is operated at an optimum gas mix containing 1.12% Xe, 0.56% HCl, and 98.32% He, at a maximum filling pressure of 80 Psi. The electrical efficiency of the laser is typically 0.3%, with an output energy of $\approx 95\ mj$ and an output laser pulse $FWHM$ of 13.5 $nsec$, resulting in an output power of $\approx 7\ MW$.
The discharge current reaches a peak value of 7.75 KA, with a rise time of 24 $nsec$, whereas the voltage reaches a maximum value of 29.1 KV, with a rise time of 111 $nsec$.

By using a CO_2 Mach-Zehnder interferometer, the electron density was measured for the optimum mix ($4.01 \pm \times 10^{15}\ cm^{-3}$). Several studies at different $Xe : HCl$ ratios showed that the dissociative attachment of HCl molecules is responsible for the electron loss during the discharge.
The electron temperature was calculated using the measured values of discharge resistance and the drift velocity. The results show that electrons cool by inelastic collisions with HCl molecules.

ACKNOWLEDGEMENTS

I especially would like to thank Professor Jochen Meyer, for his encouragement and continuous support.

Thanks to H. Houtman for his considerable technical assistance.

I also want to thank A. Cheuck, J. Bosma, and A. Schreinders for their help.

Special thanks to L. Cleven for helping with the thesis organization.

Finally, I would like to thank C.B.I.E. for the financial assistance.

Table of Contents

List of Figures

Chapter 1

Introduction

The following research is mainly a continuation of the work performed by Ford [1] in his research on $XeCl$ excimer lasers. It is aimed towards the construction of a more reliable, efficient $XeCl$ laser, and the study of two fundamental plasma parameters: the electron density in the discharge (n_e) and the electron temperature (T_e).

With this objective in mind, we constructed a simple discharge pumped $XeCl$ laser, using the same discharge circuit design as the one employed by Ford and a laser body resembling the design used by Stewart [2] for his CO_2 amplifier. Consequently, our newly constructed laser incorporates the advantages of the two developments.

The material in this thesis presents a study of a discharge pumped, u.v. preionized $XeCl$ excimer laser, using an LC double inversion circuit as an excitation scheme. It contains the results from a detailed investigation of the laser output energy under some parametric variations of, for example, the total filling pressure, charging voltage, gas mixture composition, and time delay between the main discharge and the preionization discharge. As a result of parameter optimization, the resultant laser has relatively short pulses, high energy, and excellent beam uniformity.

In the past, several numerical simulation models [3, 4, 5, 6] have been developed to predict, with satisfactory reliability, the overall performance of the $XeCl$ lasers. However, two crucial parameters of the $XeCl$ discharge plasma, n_e and T_e, were rarely predicted by these computer codes and were often reported as estimates. This is probably due to the uncertainties in the fundamental kinetic processes, and to the lack of sufficient

experimental data.

This thesis presents an experimental study of both n_e and T_e as functions of halogen donor concentration. To our knowledge, this is the first experimental attempt to determine T_e in $XeCl$ lasers. The method uses the evaluation of the drift velocity and the resistance of the discharge; by combining the two results, one can use an expression to calculate the electron temperature.

The electron density was measured by interferometric techniques. Using a Mach-Zehnder interferometer, one can measure the time varying electron refractivities in the discharge, permitting the determination of the electron density evolution.

By studying the variations of n_e and T_e for various halogen donor concentration, it was possible to propose mechanisms responsible for electron loss and cooling reactions in the discharge pumped $XeCl$ lasers.

1.1 Thesis Organization

This thesis is divided into seven chapters. Chapter 2 presents the background history of excimer lasers, focusing on $XeCl$ discharge pumped lasers and the reactions behind $XeCl^*$ formation. Chapter 3 contains a full description of the current $XeCl$ laser and solutions to some technical problems. In chapter 4, we present the investigations towards the determination of parameters permitting optimum output energy. Chapter 5 describes the electrical measurements of the discharge. In chapter 6, we describe the experimental setup and present the results form n_e and T_e measurements. Finally, in chapter 7, we present the discussion and the conclusion of the thesis.

Chapter 2

History of Rare Gas Halide Excimer Lasers

Since this research work is concerned with the study of the $XeCl$ excimer laser, a brief background history of excimer lasers is presented, with special emphasis placed on the development of discharge pumped $XeCl$ lasers.

It is surprising to find that the concept of excimer emission dates back to 1901, when Hartley [7] and Wood (1909) [8] first reported broad band emissions from the electric discharges of Hg, Cd, and Zn atomic vapours. This broad band emission was explained three decades later by Mrozowski [9]; he stated that the molecules must be in bound excited states and that they possess repulsive ground states. Another three decades passed without any progress on the excimer emissions. Then, in 1960, shortly after the laser invention, Houtermans [10] suggested that the emission from the Hg_2 molecule is a form of stimulated emission, similar to any stimulated emission occuring in atomic lasers. These molecules have repulsive molecular ground states, which make it easy for a population inversion to occur between the excited bound molecular states and the repulsive molecular ground states without any bottle-necking.

The work of Houtermans was the foundation for a new class of lasers providing the most promising source of u.v. photons at high output powers. However, attempts to obtain laser oscillations in excimers were not as simple as explained by Houtermans, and they were followed by failures [11].

In 1971, Basov et al. [12] presented the first experimental evidence of the possibility of having a noble liquid excimer laser; they realized that obtaining lasing action in excimers

requires high pumping powers; therefore, they used a relativistic electron beam to pump liquid Xe, and they observed a lasing wavelength of 176 nm.
Later, Koeher et al. (1972) [13] reported the same stimulated emission in Xe in a gaseous phase.

The first demonstration of the rare gas halide excimers was performed by Searles and Hart [14]. They reported a stimulated emission at 281.8 nm in an electron beam pumped $XeBr$ laser with a lasing mixture containing Xe and Br_2. Later, Ewing and Brau [15] observed a laser emission from XeI at a wavelength of 253.5 nm. The mixture used was composed of Ar, Xe, and I_2, irradiated with a high intensity electron beam pulsed with a Marx generator.
At the same time of Ewing's discovery, Velazco and Setser [16] confirmed the lasing spectra in $XeCl$, XeF, and $XeBr$.

The first evidence on the feasibility of the $XeCl$ laser, using electron beam pumping, was reported by Ewing and Brau [17]. Cl_2 was used as a halogen donor for the $XeCl$ laser mixture, and the laser produced an output energy of $\leq 50\ \mu j$.

Since then, most of the research and development of excimer lasers was directed towards the fluoride lasers, especially KrF lasers, which promised higher energies and efficiencies than any other rare gas halide lasers.

Using electron beam pumping has many disadvantages. For instance, the electron beam gun and energy storage systems were large in size, expensive, awkward in the pulse repetitivity, and, clearly, the scaling of these kind of lasers is difficult because of numerous factors involved in the electron beam pumping mechanism.
An alternative solution was to use electric discharge pumping; but there was a difficulty in sustaining the glow discharge at high pressures necessary for any excimer laser operation. A substantial effort went into solving this problem. Efficient electrical excitation of excimers in transient high pressure glow discharges can now be accomplished with the

help of preionization (preconditioning) of the discharge gas, using u.v. preionization [1, 18, 19, 20, 21, 22], corona preionization [23, 24], photoionization [25], or X- ray preionization [26, 27].

The discharge pumped rare gas halide excimer lasers have employed fast discharge devices, for example, LC inversion circuits [1, 18, 19, 20], Blumlein circuits [28, 29] and pulse forming networks (PFN) [22, 30, 31]. All of these were more convenient than the electron beam pumped devices because of their simple, compact designs, smaller sizes, simpler operations, high repetition rates, and high output energies per unit volume.

With the preionization techniques, $XeCl$ proved to be a laser medium as powerful and as effective as KrF, once the appropriate chlorine donor was used. As a halogen donor, Cl_2 was undesirable because it shows strong photodissociation in the u.v. range. The search for a suitable halogen donor was on. Kudryatsev et al. [32] reported $XeCl$ lasing (308 nm) in an electric discharge, with an output energy of 1 mj in various halogen donors: CF_2Cl_2, CCl_4, and BCl_3. Ishchenko et al. [33] reported higher energy (3.4 mj) in $XeCl$, using BCl_3 as a chlorine donor.

A year later (1978), Burnham [34] announced lasing in $XeCl$ discharge, with HCl as a halogen donor, resulting in a maximum output energy of 110 mj. In the same year, Sze and Scott [35] reported even more output energy in $XeCl$ (180 mj) in 48 Psi mixture containing (0.2% HCl, 5%Xe, 94.8%He).
Obviously, HCl appeared to be the best halogen donor for $XeCl^*$ lasers because it does not absorb at the lasing wavelength and it provides higher output energies.

In his paper [36], Sze summarized a series of studies directed towards the behaviour of $XeCl$ lasers under some parametric variations (charging voltage, pressure, etc.) including the optimization of the lasing output energy.

Jianwen et al. [37] reported an even higher output energy of 400 mj using a Blumlein discharge excited $XeCl$ laser having a total filling pressure of 3 atmospheres and a

charging voltage of 42 KV. The specific output energy per unit volume for this laser was 5 j/l.

Sze [38] continued his work on $XeCl$ lasers by demonstrating that the high performance and repetition rate (1 KHz) is feasible with a discharge Blumlein circuit. He reported an output energy of 0.5 mj from a small discharge volume of $10cm \times 4mm \times 2mm$, with a laser pulse $FWHM$ of 40 $nsec$.

Until then, the highest output energy reported from discharge pumped $XeCl$ lasers was of the order of half a joule; that was until the work of Watenbe and Endoh [39] was published. They measured an output energy of 13.8 J ($FWHM$ of 70 $nsec$) in the $XeCl$ mixture with an active volume of 4 l pressurized to 5 atm. The circuit they used consisted of a pulse forming line (PFL), with a characteristic impedance and capacitance of 0.5 Ω, 51 nF, respectively.

Later, Takahashi et al. [40] published a paper on the short pulse generation in a $XeCl$ discharge pumped laser. Using a Blumlein circuit and a short laser cavity of 8 cm long, they were able to obtain the shortest $XeCl$ laser pulse with a $FWHM$ duration of 1 $nsec$.

Baranov et al. [41] constructed a wide aperture (13×10 cm^2) electric discharge $XeCl$ laser with an active discharge volume of 8.5 l pressurized to 5 atm. And by employing u.v. preionization, they were able to extract a maximum laser energy of $20J$ in 100 $nsec$ $FWHM$ pulses.

Recently, Yamada et al. [42] designed a $XeCl$ laser oscillator with the highest specific power per unit volume of 2 GW/l, from an effective discharge volume of $1.5 \times 3.2 \times 100$ mm^3, which is an order of magnitude larger than what is obtained from conventional $XeCl$ discharge lasers. The laser circuit consisted of a Blumlein type discharge operated at 500 Hz repetition rate, and gave pulses of 1 $nsec$ $FWHM$, with an output power of more than 1 MW.

2.1 The $XeCl^*$ Molecule and Laser Action

Excimers (excited dimers, trimers) are not simple systems; in fact, they are weakly bound, short lived (a few nanoseconds) excited states of molecules, which under normal conditions, do not form stable molecular ground states. The excimer molecule is relatively bound only in an excited electronic state, whereas the ground state may be either repulsive, as in the case if the KrF molecule, or in a weakly bound state dissociating at room temperature, as in the $XeCl$ excimer molecule.

The ground state of the $XeCl$ molecule is a result of the combination of S^1 rare gas and P^2 halogen atoms. This state is split into two states: a weakly bound state (Σ^2) known as the X and a repulsive state (Π^2) known as the A state. The upper laser level is ionic in nature, and consists of a positively charged rare gas ion in the P^2 state (Xe^+), and a negatively charged halogen ion (Cl^-) in the S^1 state held together by the electrostatic coulomb force. The upper laser level is split into two levels: Σ^2 and Π^2 states, known as the B and C states, respectively [43, 44, 45].

Population inversion and lasing action are easy to achieve in $XeCl$ lasers. Lasing is possible, since the lifetime of bound excited upper electronic states is much higher than the dissociative time for the molecular ground states; therefore, it gives an effective pumping time to form the $XeCl^*$ molecules.

The $XeCl$ laser operates on the B-X, near 308 nm, bound-bound transition of the diatomic excimer molecule. There is also another, but weaker in gain, C-A bound-free transition near 345 nm . These transitions are possible because the decay of the $XeCl^*$ molecule to the ground state has to be completed through a radiative channel, since no thermal relaxation is possible [43].

2.1.1 Formation of the $XeCl^*$ molecule

The steps leading to the formation of the excited $XeCl$ molecule are very complicated in that they involve many reaction channels and reaction rates. The first and most important steps in the formation of the $XeCl^*$ excimer molecule are the formation of Xe^+, Cl^-, Xe^*, He^*, He^+, and $HCl(v)$ by the following reactions [3, 4, 5, 6]. Here the symbols +, -, *, and (v) denote positive ion, negative ion, excited state, and an excited vibrational state, respectively.

$$e + He \longrightarrow He^* + e \tag{2.1}$$

$$e + He \longrightarrow He^+ + 2e \tag{2.2}$$

$$e + He^* \longrightarrow He^+ + 2e \tag{2.3}$$

$$e + Xe \longrightarrow Xe^+ + 2e \tag{2.4}$$

$$e + Xe \longrightarrow Xe^* + e \tag{2.5}$$

$$e + Xe^* \longrightarrow Xe^+ + 2e \tag{2.6}$$

$$e + HCl \longrightarrow H + Cl^- \tag{2.7}$$

$$e + HCl \longrightarrow HCl(v) + e \tag{2.8}$$

$$e + HCl(v) \longrightarrow H + Cl^- \tag{2.9}$$

The formation of such species depends on the electron number density during the duration of the discharge.

Penning ionization may also contribute to the formation of the Xe^+ ion via:

$$Xe^* + Xe^* \longrightarrow Xe^+ + Xe + e \tag{2.10}$$

$$He^* + Xe \longrightarrow He + Xe^+ + e \tag{2.11}$$

Once these ions and excited atoms are present, the formation of the $XeCl^*$ excimer molecule occures via many channels, but the most effective of all is the ion-ion recombination channel, where this process involves a third body (He/Xe) to take on the extra momentum [43].

$$Xe^+ + Cl^- + He/Xe \longrightarrow XeCl^* + He/Xe \tag{2.12}$$

or through the reaction:

$$Xe^+ + Xe + He \longrightarrow Xe_2^+ + He \tag{2.13}$$

followed by

$$Xe_2^+ + Cl^- \longrightarrow XeCl^* + Xe \tag{2.14}$$

In all of the above reactions, the rate of formation of the excimer molecule is governed by the rate of formation of the halogen ion Cl^- by dissociative attachment of the HCl molecules.

Another possible way leading to the formation of the $XeCl^*$ is the neutral reaction of $HCl(v)$ with excited Xe atoms:

$$HCl(v) + Xe^* \longrightarrow XeCl^* + H \tag{2.15}$$

Once $XeCl^*$ is formed, it decays back to Xe and Cl, with the result of 308 nm photons being emitted.

$$XeCl^* \longrightarrow Xe + Cl + h\nu(308nm) \tag{2.16}$$

Chapter 3

Description of the $XeCl$ Laser

In this chapter, a brief description of the constructed $XeCl$ laser is presented. A schematic diagram of the laser is shown in figure (3.1).

3.1 Laser Chamber

Since the goals of this work are to construct a high pressure $XeCl$ excimer laser and to study the variations of the output laser energy with pressure, it is desirable that the laser tube be constructed to withstand high pressures. Also, due to the corrosiveness of the gas mixture, we require that the tube material not react with the HCl gas.

The laser tube was constructed from a 45.72 *cm* polyvinal chloride (PVC) rod, which was bored to a tube with inner diameter of 5.72 *cm* and outer diameter of 7.62 *cm*. The laser tube has two end flanges which seal against the laser windows with O-rings. Twelve holes, which permit the connections for the discharge electrodes, were drilled on opposite sides of the tube. The laser can be pumped down by using a small roughing pump before introducing the laser mixture.

3.2 Discharge Electrodes and their Profile

In order to have long lasting electrodes, the two laser main discharge electrodes were made out of solid brass of 35 *cm* in length, and 2.5 *cm* in width and they were placed 1.5 *cm* apart. Each electrode has 12 connections which connect (through the laser discharge

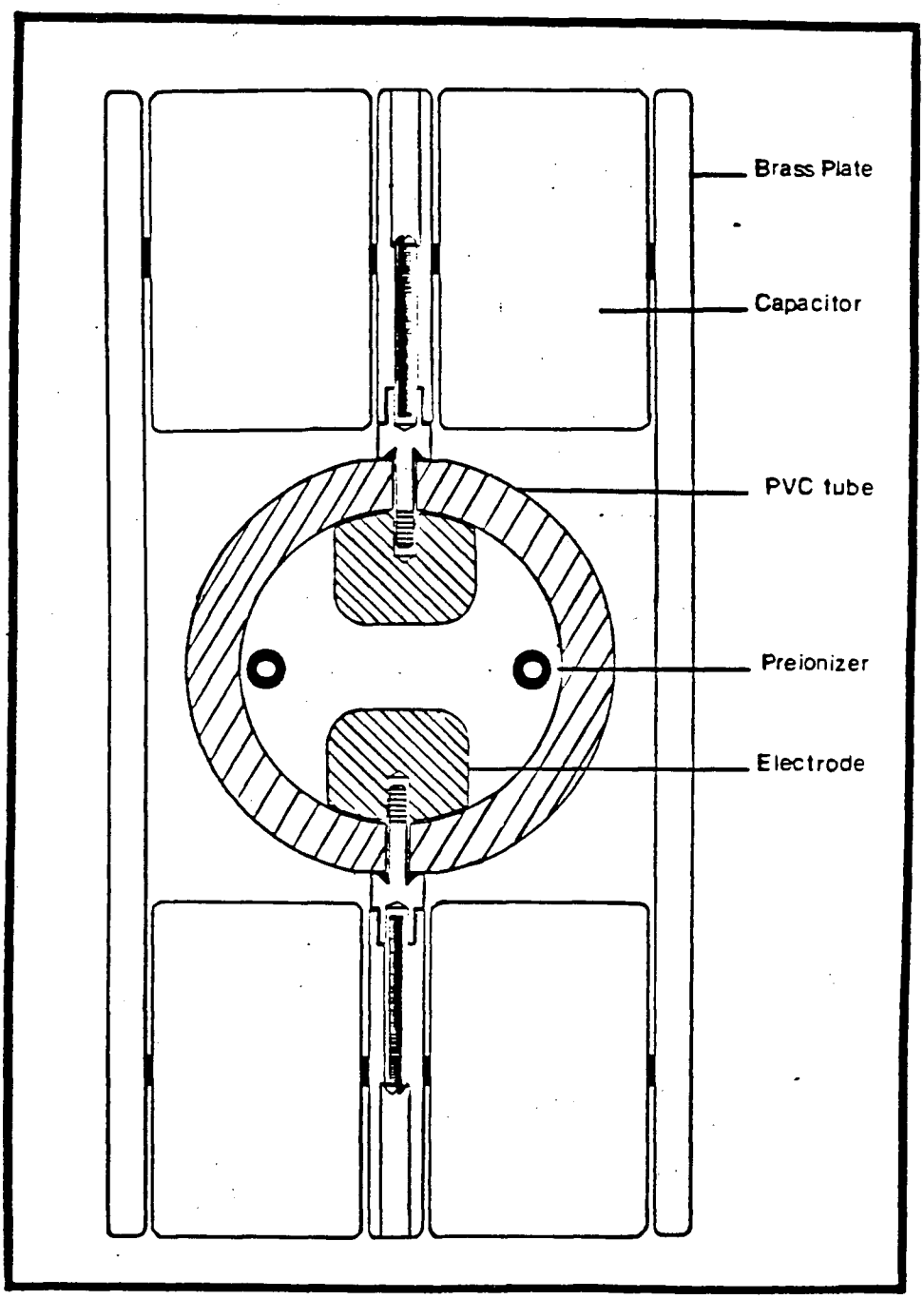

Figure 3.1: A transverse cross section of the XeCl laser

tube and seal with O-rings) to the capacitor's middle brass plate. See figure (3.1) for more details. The reason for having so many connections is to reduce the inductance of the discharge circuit.

Obtaining a stable glow discharge with a maximum possible energy density deposition requires a very uniform energy loading in the lasing gas mixture. Such uniform energy deposition can be achieved by having a very uniform electric field distribution over the discharge surface area of the electrodes; hence, we constructed Chang [46] profile electrodes with $k = 11 \times 10^{-6}$. However, the ideal profile design was followed by somewhat empirical retouchings as shown in figure (3.2). Due to the lack of numerically controlled milling machines, the electrodes were smoothly countoured by hand, and were taken in and out of the discharge for possible repolishing after visual observations of discharge inhomogeneties.

The helium discharge appeared to be spatially uniform with no observable streamers. Figure (3.3) shows a uniform discharge in helium as seen along the optical axis. However, it proved to be impossible to have a uniform arc-free glow discharge in the XeCl mixture with the electrode profile used by Stewart [2]. With his profile, the main discharge took place along both sides, instead of the central parts, of the electrodes. This resulted in a laser beam profile consisting of two stripes separated by a central dark region.

Using the modified Chang profile reduced the effective discharge volume to $0.5 \times 1.5 \times 35\ cm^3$, estimating the discharge width of the laser volume from the burn spot of the laser beam on the back of 667 Polaroid film.

3.3 Brewster Windows

Minimizing the optical losses, due to surface reflections and the corrosive nature of the lasing gas to the optical resonator, requires the use of Brewster windows where the

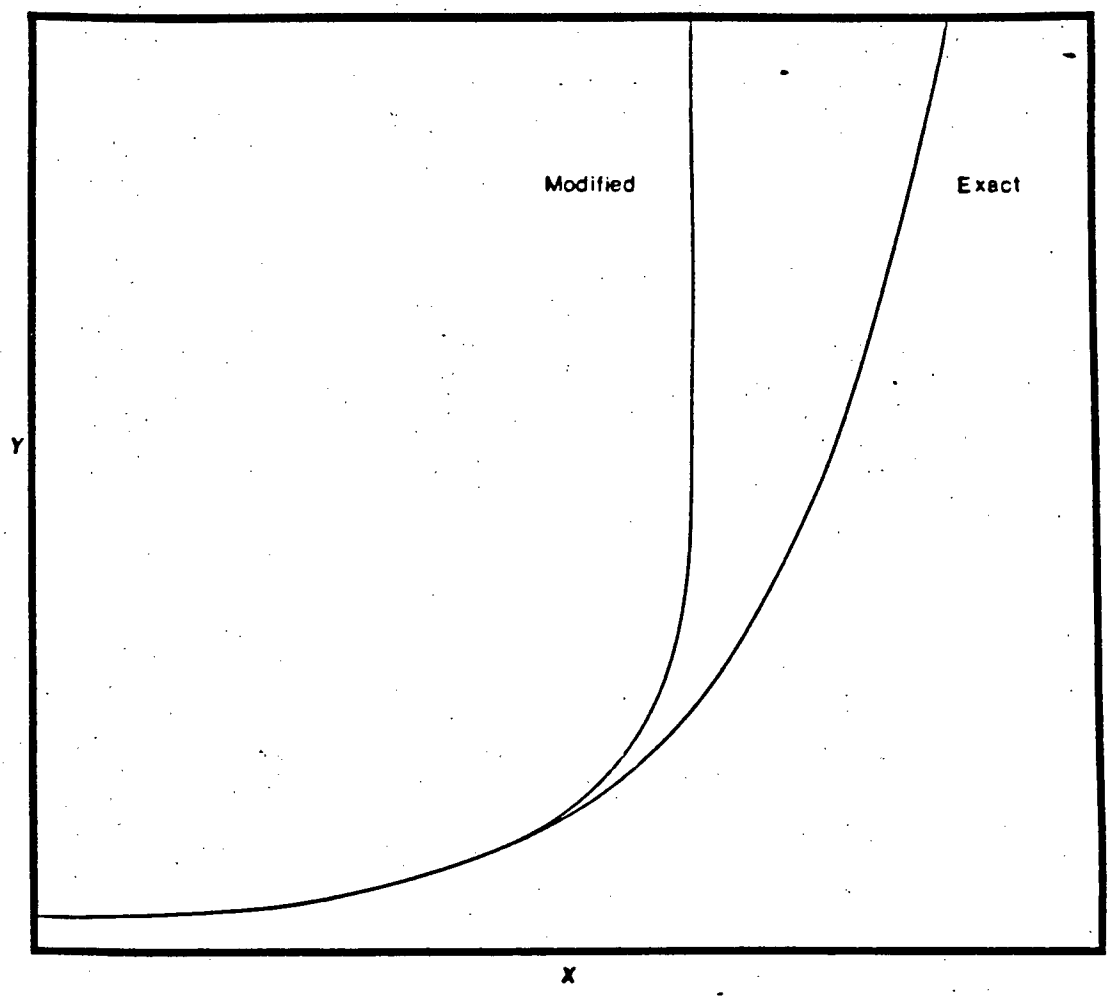

Figure 3.2: The ideal and the modified Chang profiles.

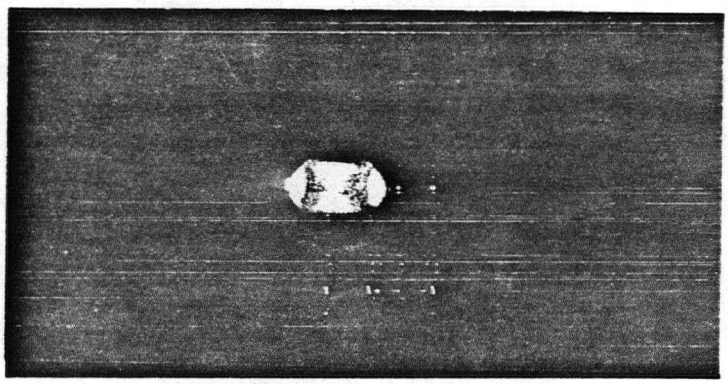

Figure 3.3: He glow discharge at 50 Psi, 22 KV, and $\triangle$t=600 ns.

resonator mirrors are placed outside the discharge chamber.

Mounted on both ends of the discharge chamber, both of the Brewster windows were made to withstand high pressure operations. The window flanges were machined out of transparent lucite 0.25 inches thick; the output windows were 2 inches in diameter, 0.5 inches thick quartz plates tilted at Brewster angle of 55.5° (see figure (3.4) for more details) attached directly to the housing of the windows, thus exposing the quartz plates directly to the corrosive lasing gas and the discharge. This led to a deposition of dust-like particulates on the optical windows and, as a result, they have to be removed for cleaning after several shots.

3.4 U.V. Preionization Rods

Preionization of the main discharge was provided by arrays of u.v. sparks. Two preionization rods were used; each one was made out of a series of seventeen (2.4 *cm* long each) stainless steel tubes. The end edges of the stainless steel tubes were cut at 30° to the axis of the tube, and were fitted through a 5 *mm* diameter glass tubing of 44.45 *cm* in length so that the protruding edges were spaced 1 *mm* apart from each other. High voltage was applied to the first stainless steel tube, and was returned by a high voltage wire running through the glass tubing. Both preionization rods were placed along the sides of the main discharge parallel to the laser electrodes, and were placed 2.54 *cm* apart. This mechanical design ensures a uniform u.v. distribution all along the discharge volume.

The spark discharges were powered by a separate RLC circuit, and charged by the same power supply.

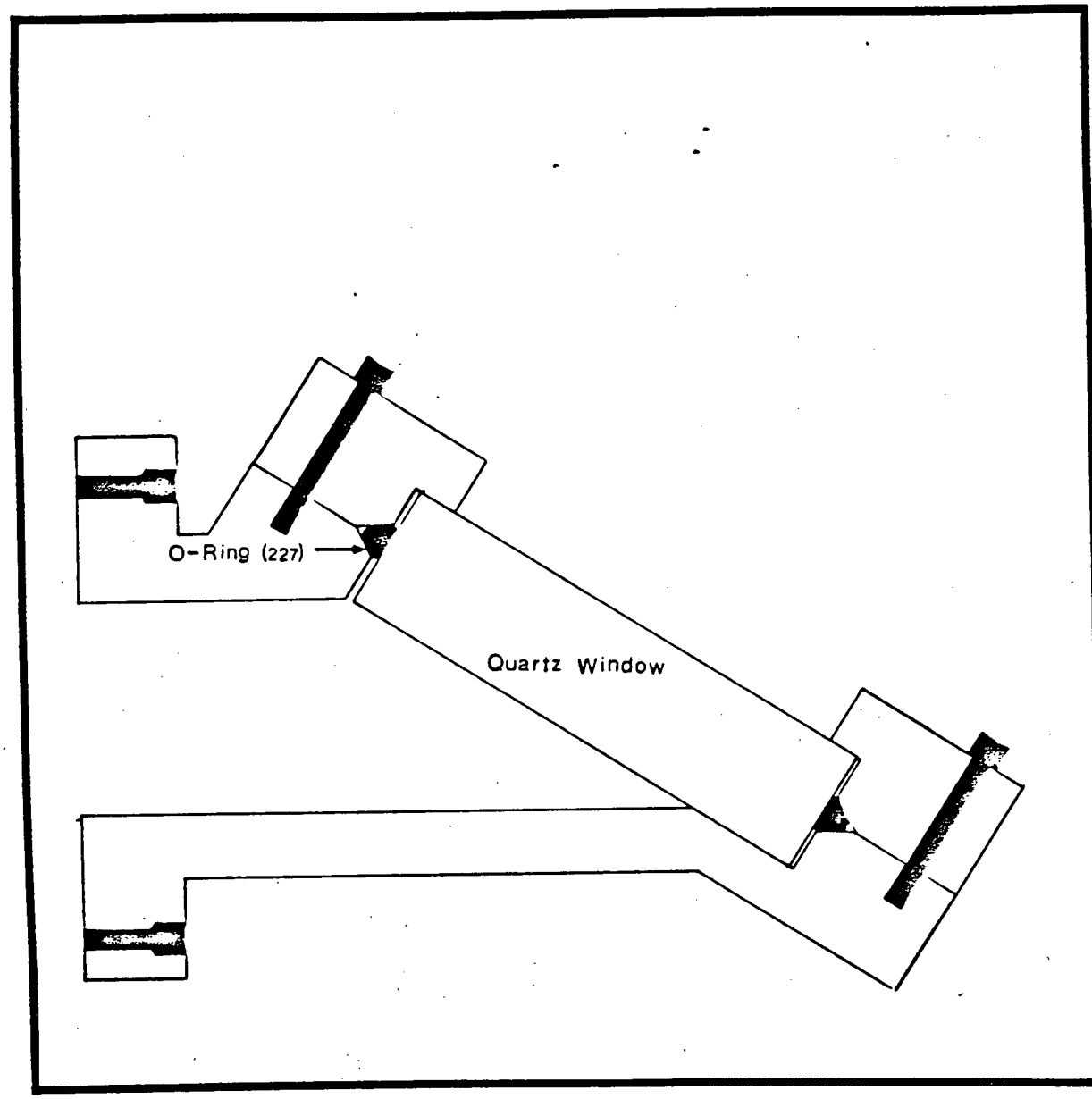

Figure 3.4: Laser Brewster window.

3.5 The Optical Resonator

In general, excimer lasers have such high internal gain compared to other TE discharge lasers that they can be operated as superradiant lasers. Both high optical gain and possible superradiance are important factors in designing the appropriate optical resonator for such lasers.

Excimer laser resonator cavities are, in general, under one metre long. In the present case, the resonator cavity was about $\approx 75cm$ long, with the output coupler mounted in a standard configuration of a plano-plano marginally stable optical resonator. As in most discharge lasers, the rear resonator mirror (2 inches in diameter) is coated (aluminum in this case) for maximum reflectance. However, because of the high internal optical gain, there is no need to coat the output coupler; thus, we have used uncoated quartz flat 2 inches in diameter and 0.5 inches thick.

3.6 Gas Handling System and Gas Mixture Life Time

The gas handling system includes a high pressure mixing bottle, in which high quality research grade HCl, Xe, and He gases could be mixed. The gases were fed to the mixing bottle through copper tubings in combination with poly-flo tubings. The gases were mixed to desired concentration by adjusting their partial pressures in the mixing bottle. The minor constituents (Xe and HCl) were fed first to make precise pressure measurements easier with the vacuum gage, whereas the buffer gas was fed slowly so that the Xe and HCl gases trapped in the poly-flo and copper tubing could mix evenly with He. In order to ensure even mixing, the gas mixture was allowed to sit for 15 minutes before use.

In some experiments, the gas was mixed in the discharge chamber. And since no noticeable reduction in output energy was observed, we mixed the gases in the chamber

or the mixing bottle interchangeably.

The disadvantage in working with *XeCl* lasers is the handling of the corrosive HCl gas. The halogen donor gas (HCl) reacts strongly with the laser building materials [47, 48, 49]; these reactions create impurities in the laser gas mixture that may cause arcs to develop, absorption of the laser photons or of u.v. radiation generated from preioization, and optical damage or degradation to the quartz windows.

The u.v. preionizers can also produce some impurities in the gas. The u.v. light, upon impact on the *PVC* tube, O-ring seals, or lucite flanges can lead to the formation of chlorocarbons which can absorb light at the laser wavelength [47]. Also, arcing of the main discharge results in the heating of certain spots on the brass electrodes, leading to the release of chemicals into the discharge region.

One severe problem we faced consists in the optical degradation of the quartz windows due to the deposition and build up of particulates from the discharge gas on the inner surface of the windows and the formation of thin film on them. A burn spot on the film was observed on the inner face of the quartz windows. The spot has the same shape and dimensions as the lasing aperture. One way to prevent this coating from forming is to redesign the laser gas inlet where the laser gas mix can be fed to the laser chamber in a tangential direction to the quartz windows, as a result, flushing the windows each time the gas mixture is added.

The sealed off life of the gas mixture is found to be short (a few days); therefore, we may consider the gas to be consumable. A significant reduction in the laser output energy of $\approx 40\%$ is observed when the lasing mixture has been left in the mixing bottle for over a day. This suggests that the laser gas mixing bottle is not HCl compatable; therefore, all the parametric studies were performed in fresh laser mixes a few hours old.

The accumulation of impurities results in a gradual decrease in the laser pulse energy, the lifetime of the lasing gas mixture, and the performance of the laser. However, the

laser is restored back to its normal full power operation once the lasing gas mixture has been replaced with fresh mixture.

The most effective and satisfactory solution to the gas life time problem is to consider a flowing gas system. Circulating the laser gas mixture through the discharge region helps to sustain constant output energies, to reduce impurities, and to remove the excess discharge heat when a high repetition firing rate is required. But due to the small fixed diameter of the laser gas inlet ($\frac{1}{4}inch$), it proved to be impossible to use a circulating fan to maintain a satisfactory gas flow.

3.7 Discharge Driving Circuit

In order to form the lasing $XeCl^*$ molecule, the deposition of the electrical excitation energy must be fast enough so that the transient glow discharge does not constrict into arcs. Therefore, the pumping circuit has to be fast. The LC double inversion circuit is one of the most simple and efficient ways to excite a rare gas halide lasers [1]. Efficient operation of such lasers depends strongly on the low inductance of the driving circuit and on the density and distribution of the initial electrons produced by the preionization process.

The principle behind an LC inversion circuit is that the capacitors (i.e. C^*, and C^{**} in figure 3.6a) are charged in parallel. When the spark gap switch, R_1, is closed, the voltage across the capacitor (C^{**}) reverses direction: the voltage across the laser at this time becomes double the charging voltage of the capacitors. If the laser discharge breaks down at this time, then the equivalent circuit of the discharge circuit reduces to the one shown in figure (3.6b).

The discharge circuit is composed of two independent circuits: The main discharge circuit and the preioization circuit as shown in figure (3.5). The main discharge circuit

consists of the energy storage capacitors. Twenty four ceramic doorknob capacitors, each having a capacitance of 2.7 nF, were divided symmetrically between both sides of the discharge chamber and as close as possible to it, therefore, minimizing the inductance of the discharge circuit, and giving a total capacitance of 16.2 nF. On each side, the two rows of the capacitors were connected with a 21.1×33.2 cm^2 0.65 cm thick brass plate, again to minimize the inductance of the circuit. These plates were connected directly to the charging power supply via a 50 $M\Omega$ TRW high voltage charging resistor. It should be noted that the plates were covered around the edges with kepton tape for high voltage insulation to prevent corona sparks from jumping across the capacitor banks.

The switchings of the main and the preionization discharges were made possible by two low inductance spark gaps, which were pressurized with dry air to withstand the charging voltage. Each spark gap was triggered by a triggering pin connected to a separate Krytron unit through a 4:1 step-up transformer. Each Krytron unit uses an EG&G Krytron and gives a triggering pulse of 10 KV.

We have tried coupling the preionizers to the main discharge circuit (i.e. automatic preioization), which is similar to the design reported by Houtman et al. [50], where the main and the preionization discharges were supplied from common capacitors. Unfortunately, this technique did not work due to the development of discharges jumping from the electrodes to the preionization rods, which was followed by an arc-like discharge. This suggests that the preionization rods were sitting at a different potential than the half way potential between the main discharge electrodes.

The preionization circuit is composed of four 2.7 nF ceramic doorknob capacitors, two for each preionization rod, charged up from the same power supply via 50 $M\Omega$ high voltage TRW resistor. To minimize the chances of the main discharge voltage jumping to the preionizers, the preionization rods were capacitivally coupled, through four 0.5 nF capacitors, to both main discharge electrodes. This ensures that the preionizers are

always kept at half way potential during the main discharge voltage switching.

For a high pressure volume dominant glow discharge, one requires a delay between the preionization and the main discharge. Such a delay is important for the initial electron concentration to grow and reach a maximum value $\approx 10^7\ cm^{-3}$ (as reported by Taylor [51]) creating the ideal conditions for uniform main glow discharge. The time delay between the preionization and the main triggering pulses can be varied electronically. It turned out that this delay could be varied anywhere between 400 *nsec* and 800 *nsec*, without having any significant effect on the output of the laser energy. It was decided to operate the laser main discharge at 600 *nsec* time delay.

3.7.1 Discharge Circuit Analysis

Figure (3.6a) shows one side of the discharge circuit, where R_1, R_2 are the resistances of the spark gap and the laser discharge, respectively, and L_1, L_2 are the inductances of the circuit and the laser head, respectively. As the spark gap fires (R_1) the voltage across capacitor C^{**} inverts, and current I_1 will start to flow through L_1 until the voltage across the laser reaches the breakdown voltage of the gas, then current I_3 will start to flow through the laser discharge (R_2); at the same time, the capacitor C^* starts to discharge through the laser head.

The inductance L_2 was measured from the ringing frequency of the voltage trace (without firing the main discharge), and was found to be equal to 220 nH.

The circuit in figure (3.6a) can be described by the following set of equations:

$$I_1 = I_2 + I_3 \tag{3.1}$$

$$C^* L_1 \frac{d^2 I_1}{dt^2} + C^* R_1 \frac{dI_1}{dt} + I_2 = 0 \tag{3.2}$$

and

$$C^* L_2 \frac{d^2 I_3}{dt^2} + C^* R_2 \frac{dI_3}{dt} + I_3 - I_2 = 0 \tag{3.3}$$

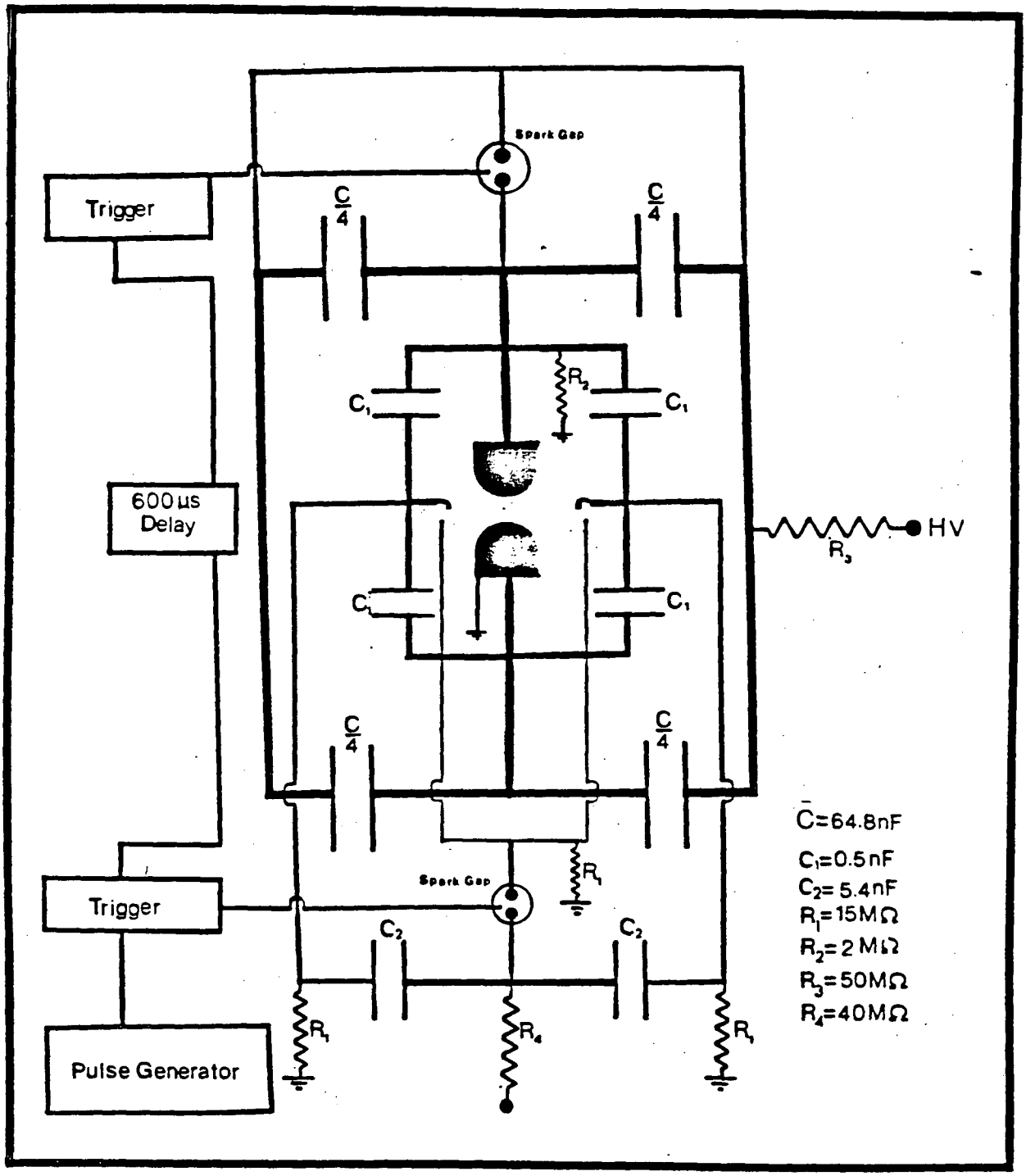

Figure 3.5: The laser discharge circuit diagram.

where $C^* = C^{**} = C/4$ =16.2 nF. The initial conditions are: the total charge $Q(t=0)$ =C^*V_c where V_c is the charging voltage, $I_3(t=0) = 0$, and $\frac{dI_3(t=0)}{dt} = -\frac{V_b}{L_2}$, where V_b is the breakdown voltage. To find the frequencies of oscillations, one can treat the circuit as two coupled oscillators with two oscillation frequencies ω_1 and ω_2. Since the resistances R_1 and R_2 contribute only to the damping term in $I_3(t)$, they can be ignored while solving for the frequencies. Therefore, solving equations (3.1) to (3.3) gives the following differential equation for $I_3(t)$

$$C^*L_1L_2\frac{d^4I_3}{dt^4} + C^*(2L_1 + L_2)\frac{d^2I_3}{dt^2} + I_3 = 0 \tag{3.4}$$

By assuming a plane wave solution (for $L_2 \ll L_1$), one can get the two oscillation frequencies ω_1 and ω_2:

$$\omega_1 = \pm\sqrt{\frac{1}{2C^*L_1}} \tag{3.5}$$

$$\omega_2 = \pm\sqrt{\frac{2}{C^*L_2}} \tag{3.6}$$

with the use of the initial conditions one can obtain an expression for the current I_3

$$I_3(t) = \sqrt{\frac{2C^*}{L_2}}(V_b + \frac{L_2V_c}{L_1})sin(\sqrt{\frac{2C^*}{L_2}}t) - \sqrt{\frac{2C^*}{L_1}}(\frac{V_b}{2} + V_c)sin(\sqrt{\frac{1}{2C^*L_1}}t) \tag{3.7}$$

The above expression was multiplied by two to account for the other half of the circuit. For the times when t is less than $\pi\sqrt{C^*L_2}$, the second term is negligable, and the expression for $I_3(t)$ is reduced to

$$I_3(t) = \sqrt{\frac{2C^*}{L_2}}(V_b + \frac{L_2V_c}{L_1})sin(\sqrt{\frac{2C^*}{L_2}}t) \tag{3.8}$$

Equation (3.8) shows that the amount of current deposited in the discharge increases with increasing charging voltage. The way to gain any insight into the discharge circuit

is to consider the circuit to be simply an ohmic circuit (see figure (3.6b)). Consider the laser discharge head having a resistance R_2; we then can come up with an estimate of the discharge circuit impedance.

Next, consider a single current loop on one side of the laser going from the capacitor bank through the discharge region and back to the same capacitor bank. Such a current loop encloses an effective area of 75 cm^2; hence, the inductance can be found from the relation of a single coil inductor, so that:

$$L_2 = N^2 \mu_o A/l \tag{3.9}$$

Where N is the number of turns =1,
A is the cross sectional area enclosed by the current loop =75 cm^2,
l is the discharge length which is equal to the length of the electrode =35 cm, and
μ_o is the permeability of free space.

This gives a one side inductance of 27 nH. With this analysis, we can also estimate the impedance match of the discharge. For a critically damped circuit, the condition for impedance matching is:

$$R_2 = 2\sqrt{L_t/C} \tag{3.10}$$

Where L_t is the total inductance of the laser circuit, which is half the inductance of one side of the discharge =13.5 nH, and C =16.2 nF. The calculated R_2 =1.83 Ω.

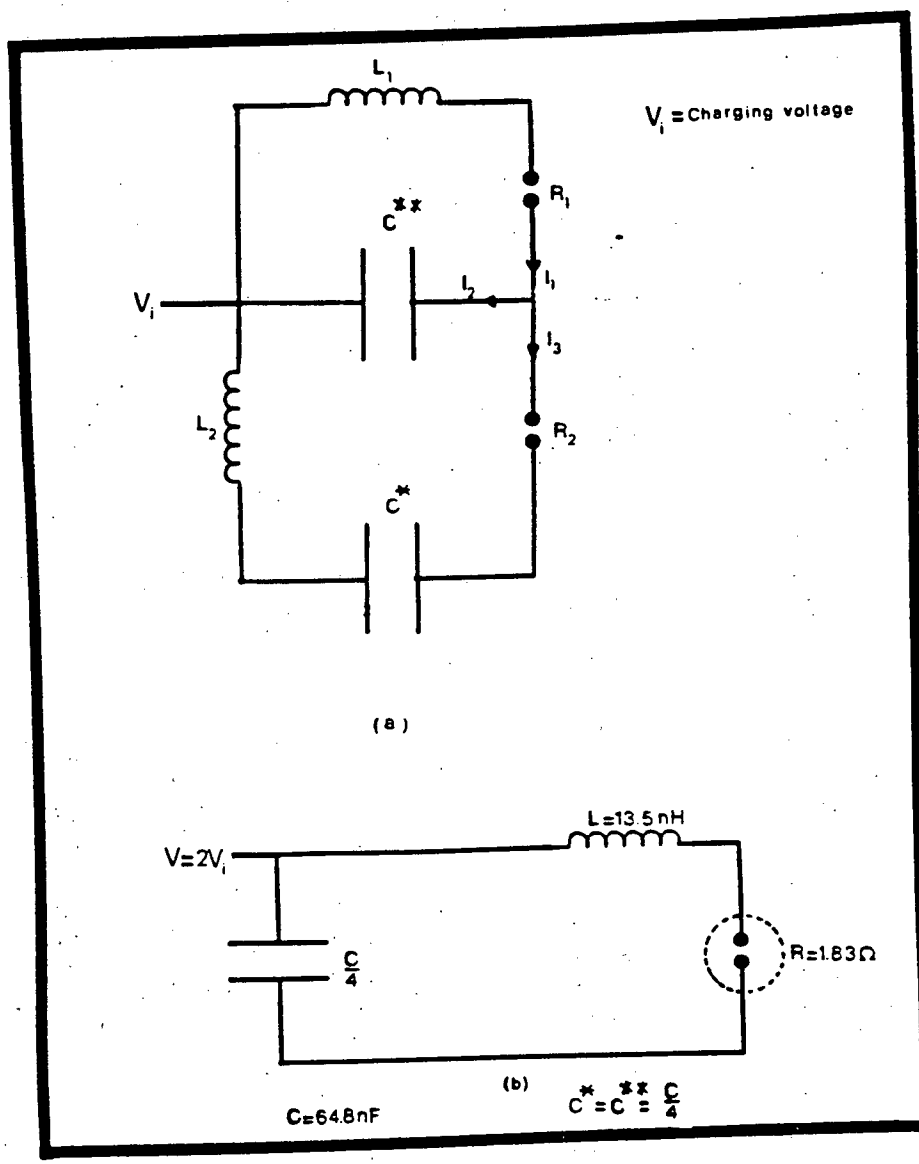

Figure 3.6: (a) One side of the dicharge circuit, (b) equivalent circuit.

Chapter 4

$XeCl$ Laser Output Energy Optimization

The need to optimize the laser energy is an essential step before proceeding with any kind of laser parameter measurements, for example, the discharge breakdown voltage, discharge current, pulse duration, and electron density. The measurements of these parameters should improve the understanding of the $XeCl^*$ kinetics in the discharge, and may help in the development of more efficient, large scale $XeCl$ lasers. Therefore, one should investigate the laser output energy and its behaviour as a function of different parameters, such as the charging voltage, the total lasing mixture pressure, the concentration of the lasing components (i.e. Xe, and HCl), the buffer gas (He), and the timing delay between the preionizing u.v. light and the main discharge.

The laser output energy was measured with a *Gentec ED200* joulemeter. The output energy was found to be sensitive to the alignment of the optical resonator. As much as a factor of two is lost due to slight misalignment. This was demonstrated by slightly misaligning the output coupler.

4.1 Variations of the Laser Energy with the Charging Voltage

A study of the laser output energy and its dependence on the charging voltage was carried out for different Xe and HCl concentrations and various total filling pressures. However, because of the 40 KV maximum ratings on both the power supply and the charging capacitors, it was not possible to go beyond this limit in carrying out the laser energy measurements. In all the experiments, the maximum possible operating voltage

was 35 KV; trying to exceed this voltage resulted in the breakdown of the capacitors.

In general, it was found that the laser output energy increases (at high pressures) as the charging voltage increases. This increase in the energy can be explained from equation (3.8). Since the current deposited in the laser (I_3) increases as the charging voltage increases, the electric energy deposited in the gas rises; as a result, more energy is obtained from the laser. Figures (4.1) to (4.10) show how the laser output energy changes with the charging voltage for various gas mixes. Each plotted point was averaged over more than ten runs taken in sequence.

The largest output energy was 96 mj at 30 to 35 KV, measured in a mixture consisting of $Xe(5\%), HCl(1\%)$, and $He(94\%)$; however, even though this was the highest energy measured, the glow discharge was unstable for long term operation.

4.2 Pressure Optimization for Higher Efficiency Operations

In our current study, we have studied the variations of the laser output energy with the total gas filling pressures for several Xe, HCl, and He concentrations, and different charging voltages, with the objective to find the optimum laser gas filling pressure for efficient operation.

The most dominant channel in the $XeCl^*$ formation is the ionic recombination which depends mainly on the density of a third body [43], such as He. Therefore, as the total gas pressure increases, the density of He atoms increases, which, as a result, helps in the formation of $XeCl^*$ molecules.

Figures (4.11) to (4.20) show the behaviour of the laser output as a function of the total gas filling pressure ranging from 40 Psi up to 90 Psi. However, rapid arc formation developed in the discharge at a laser gas pressure exceeding 90 Psi, which may be due to the instability of glow discharge at high pressures.

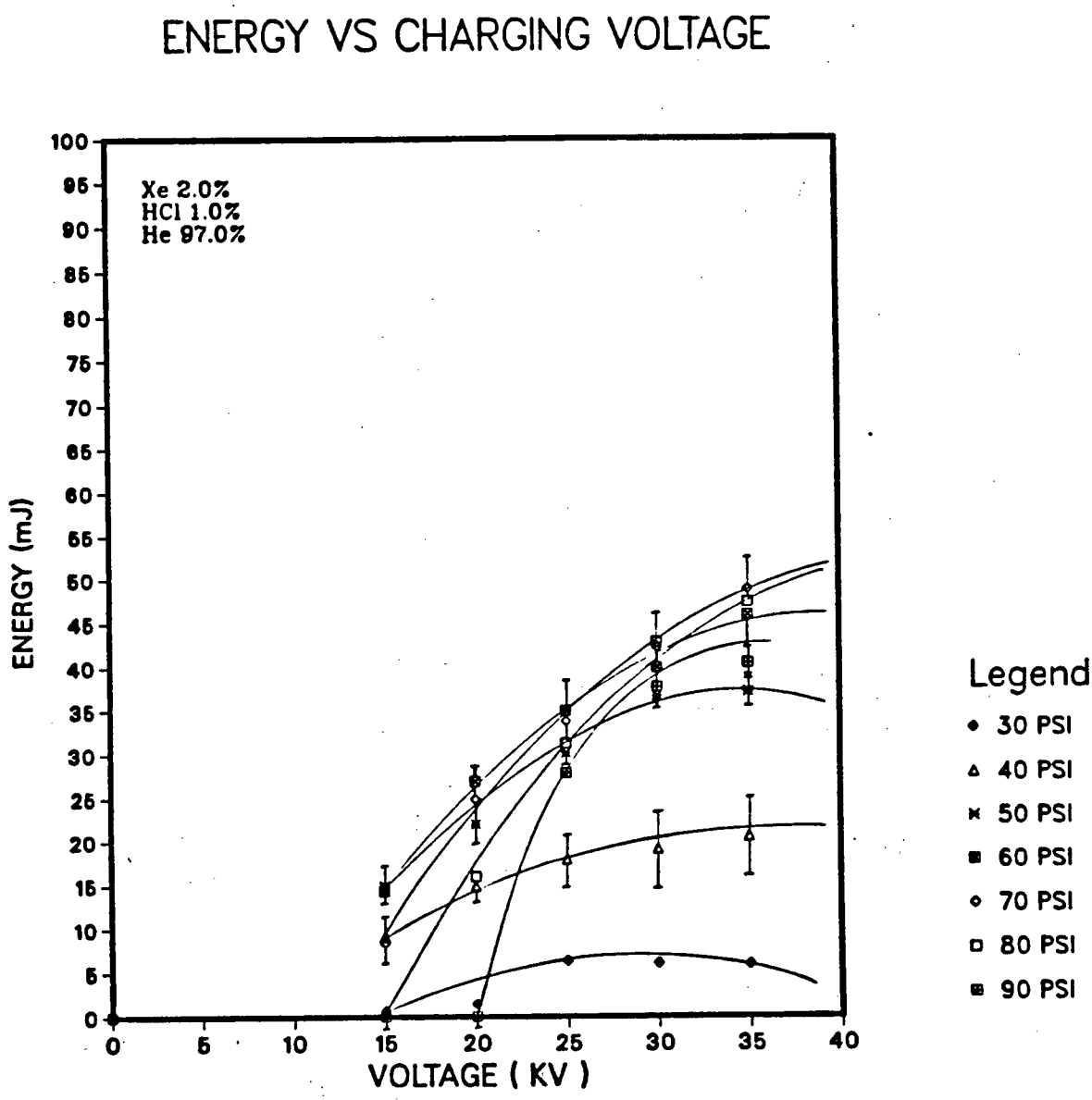

Figure 4.1: Output energy versus charging voltage.

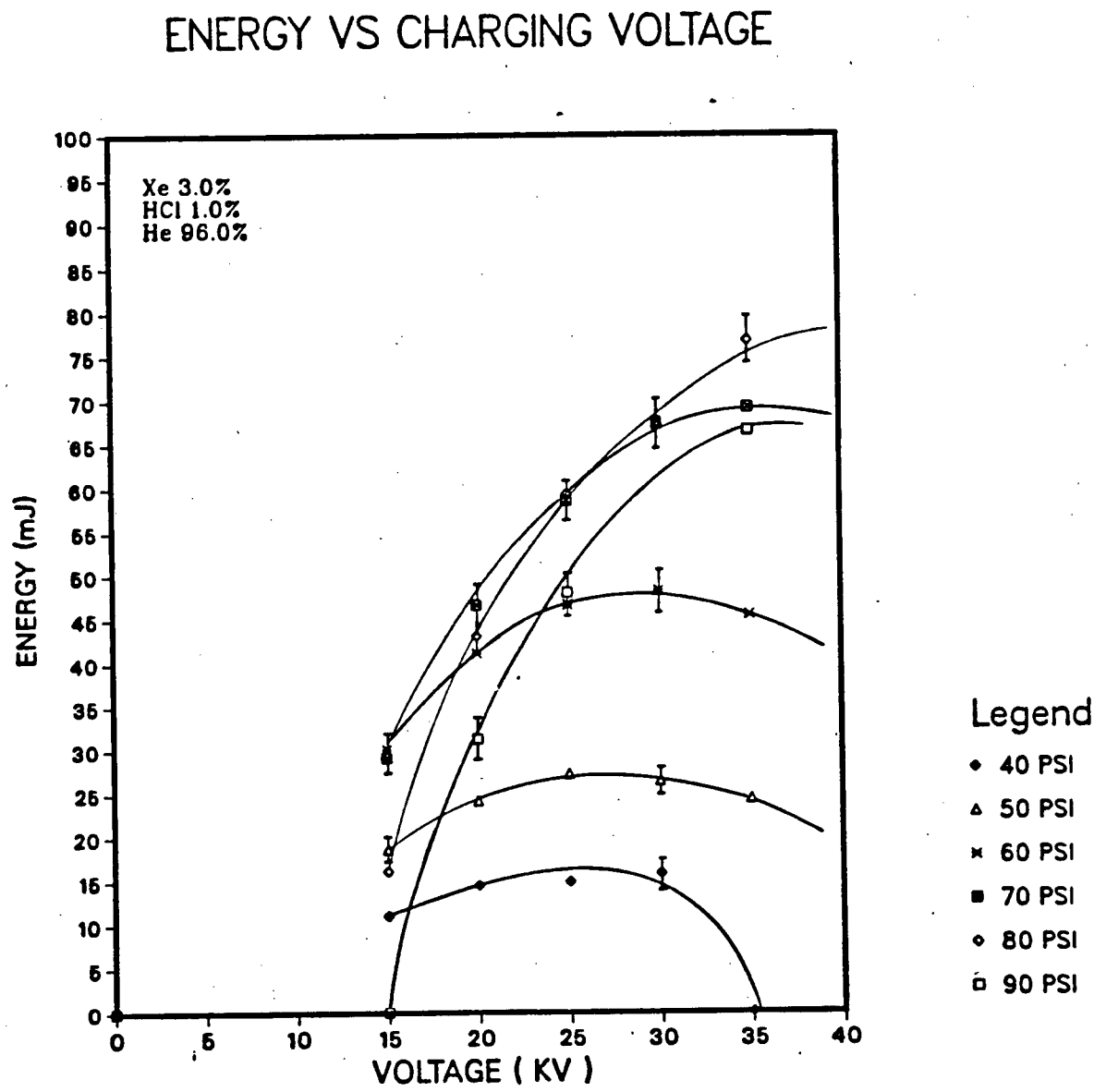

Figure 4.2: Output energy versus charging voltage.

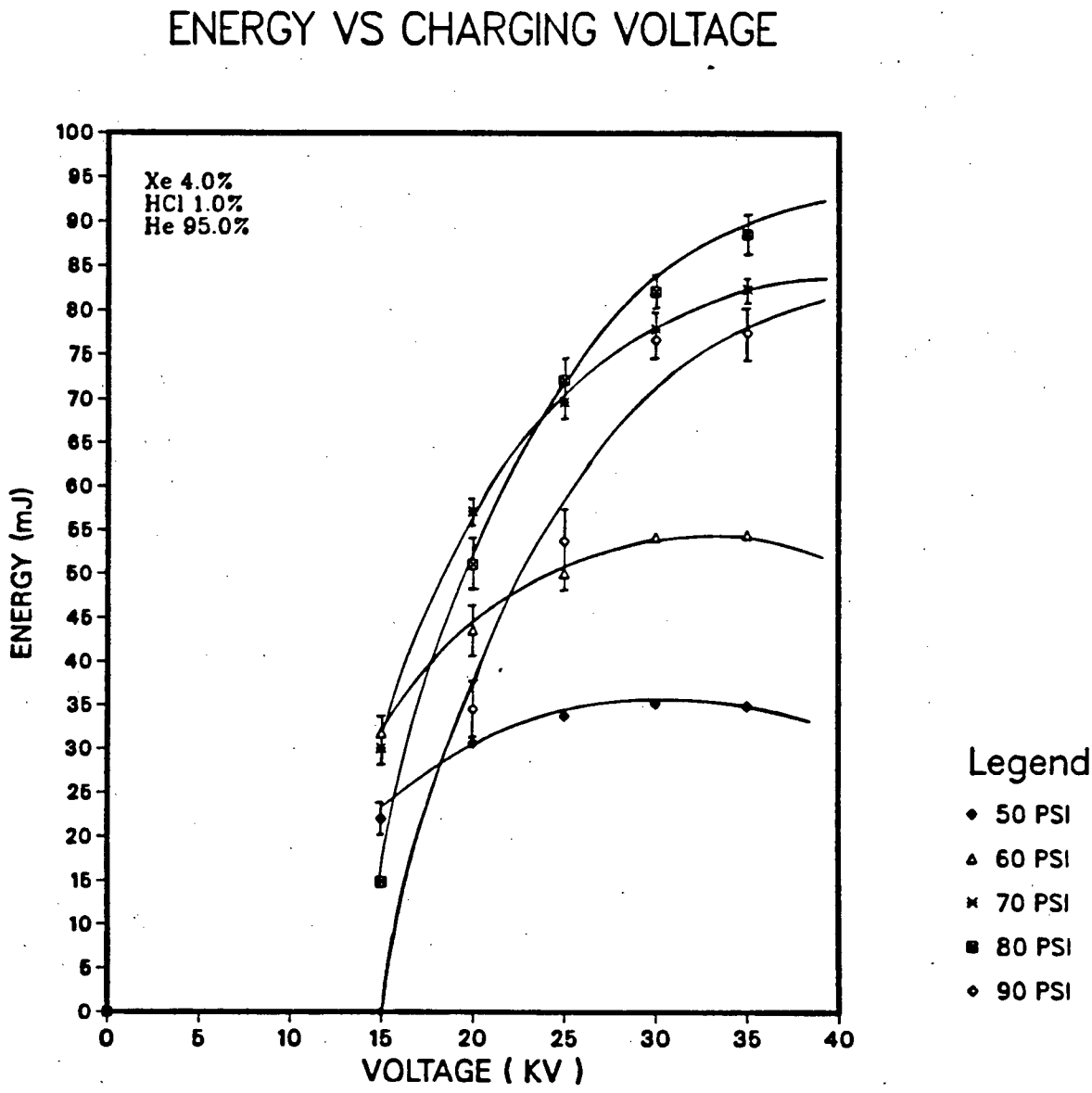

Figure 4.3: Output energy versus charging voltage.

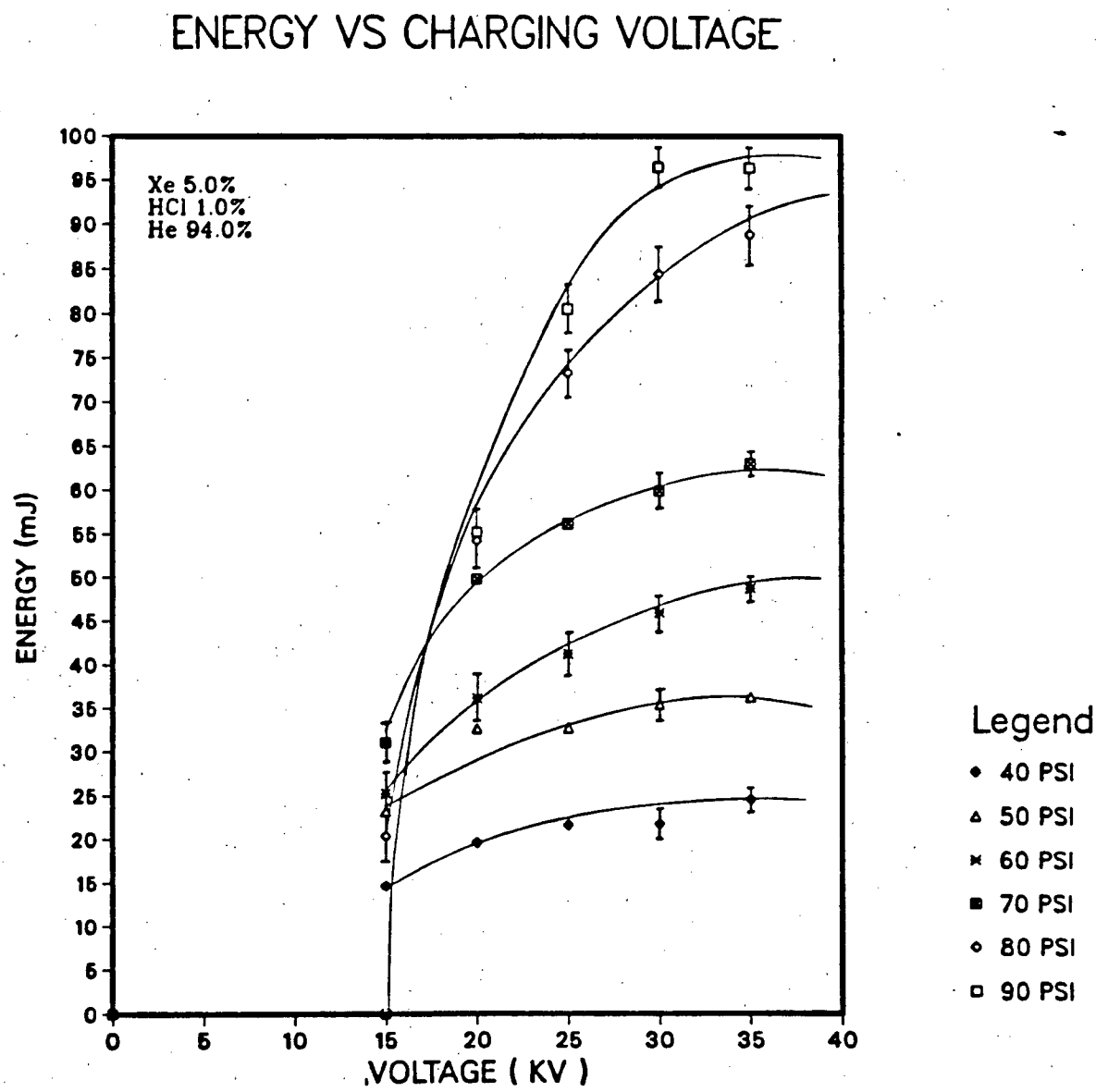

Figure 4.4: Output energy versus charging voltage.

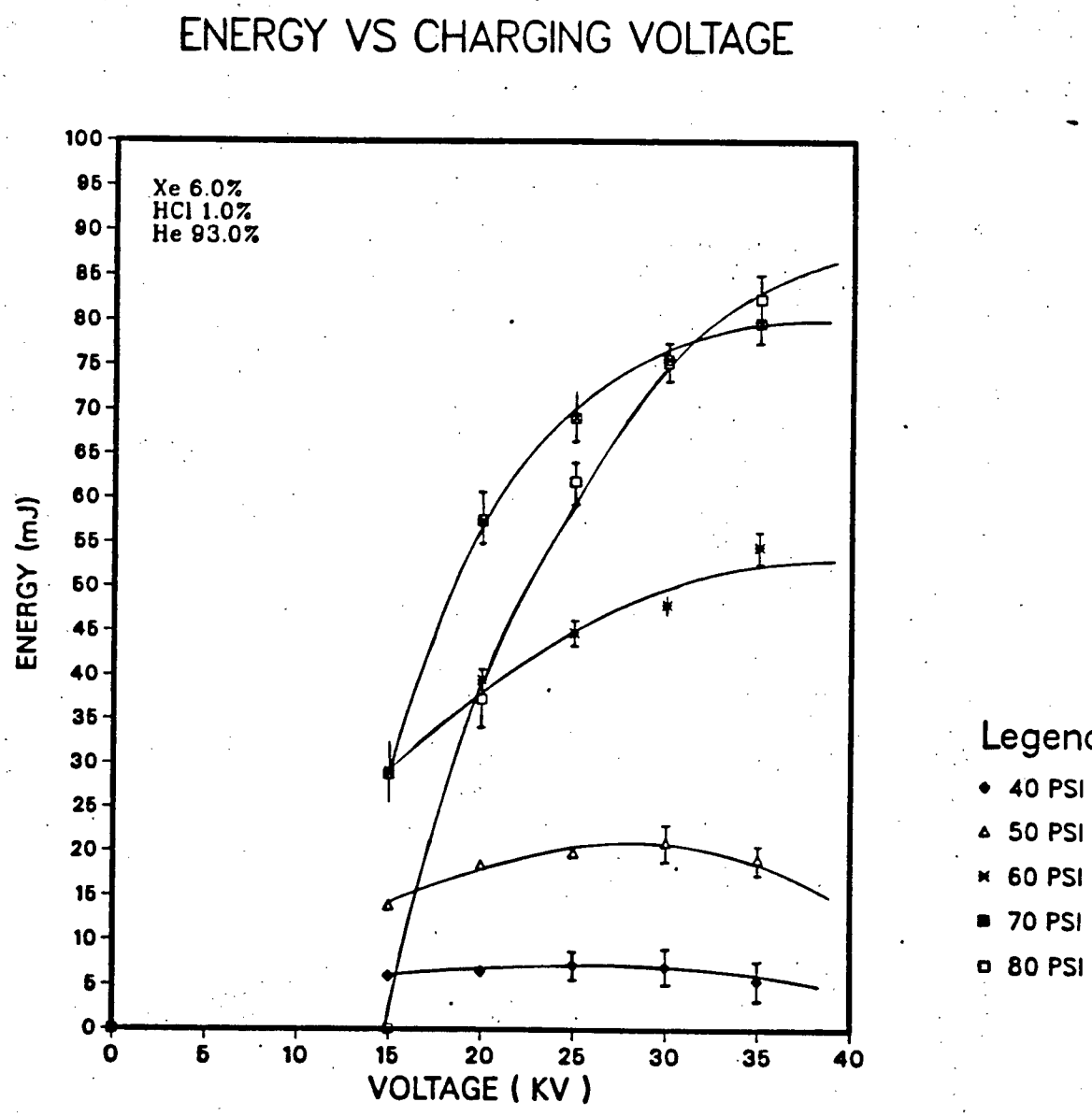

Figure 4.5: Output energy versus charging voltage.

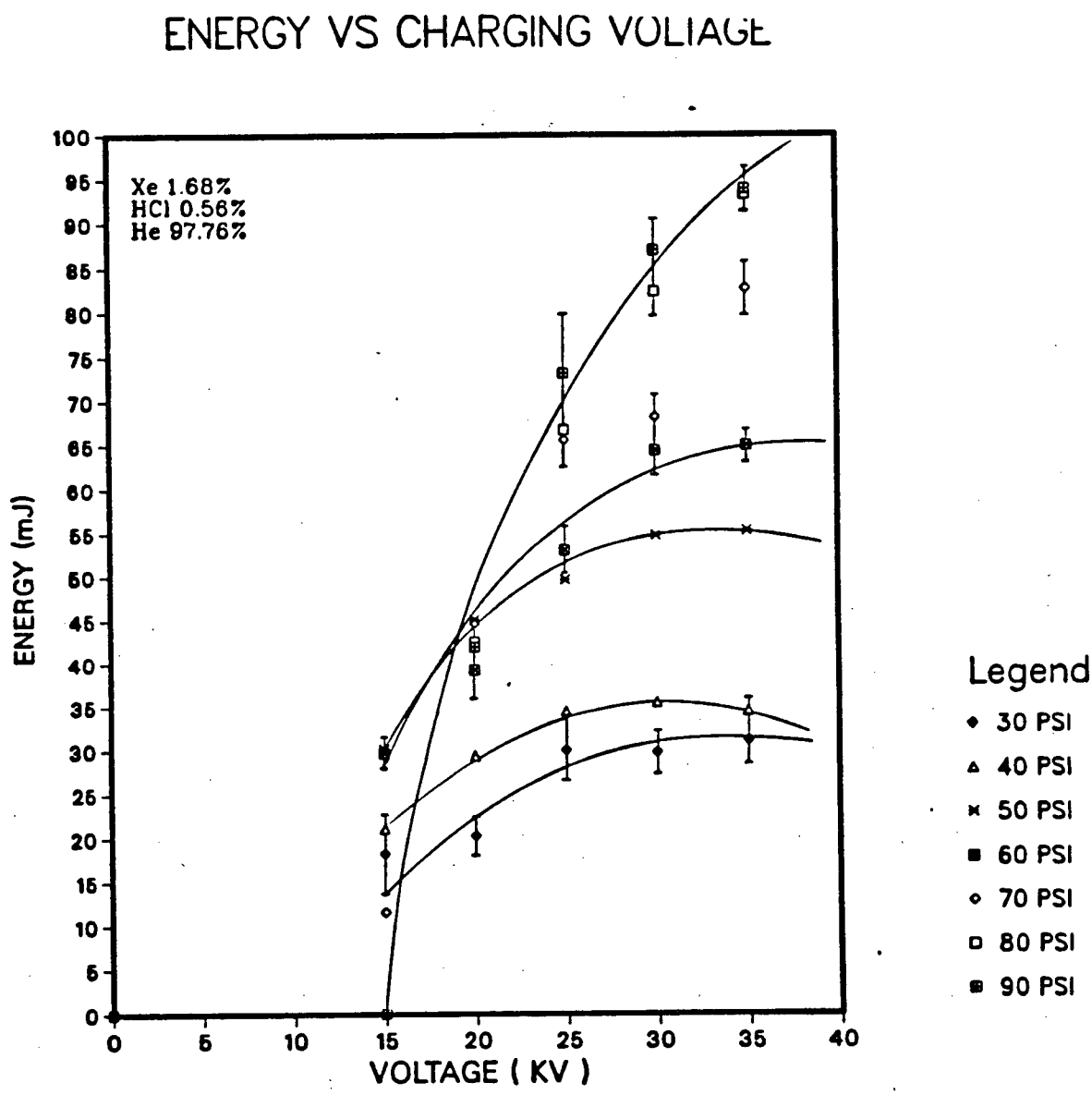

Figure 4.6: Output energy versus charging voltage.

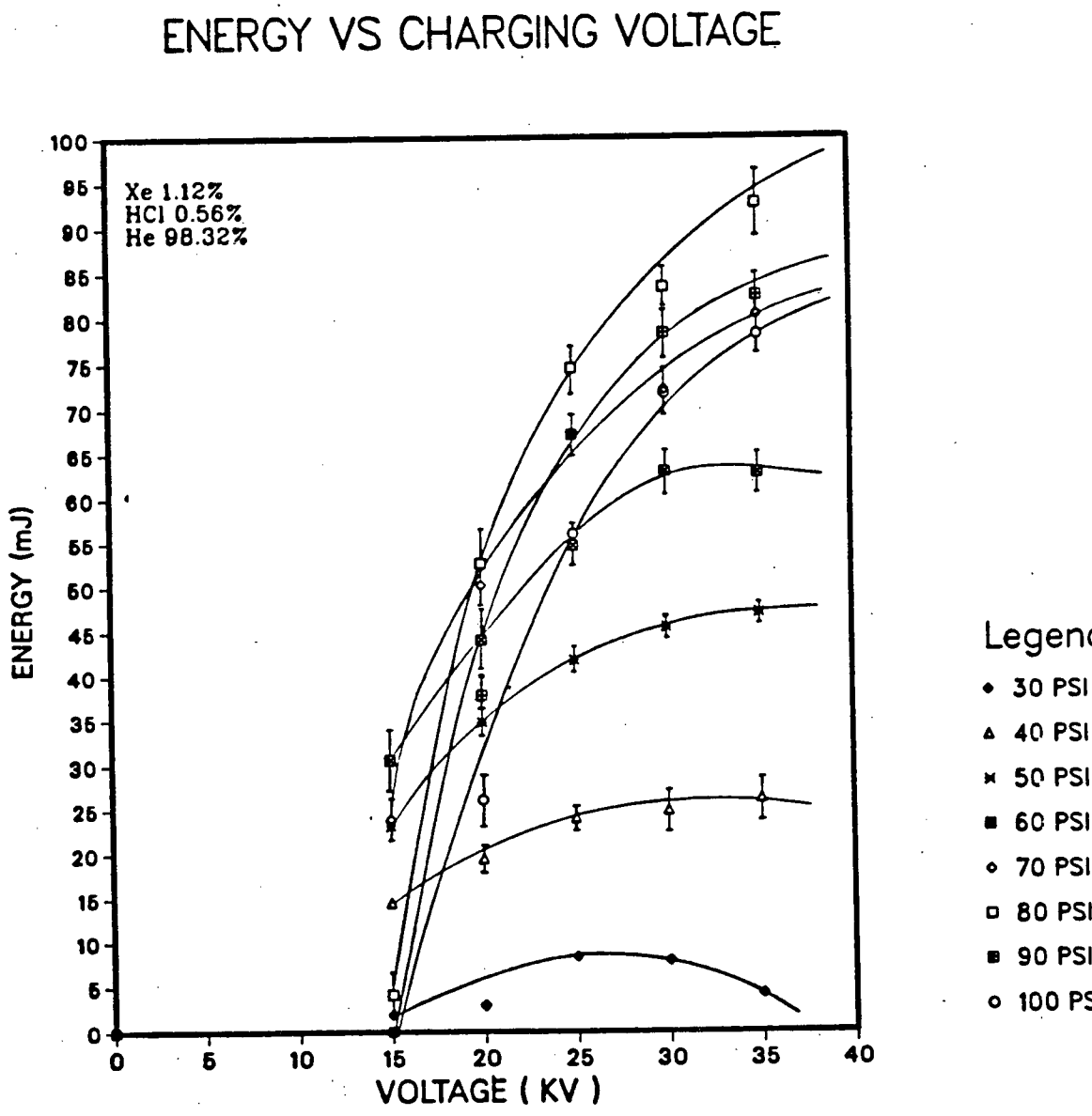

Figure 4.7: Output energy versus charging voltage.

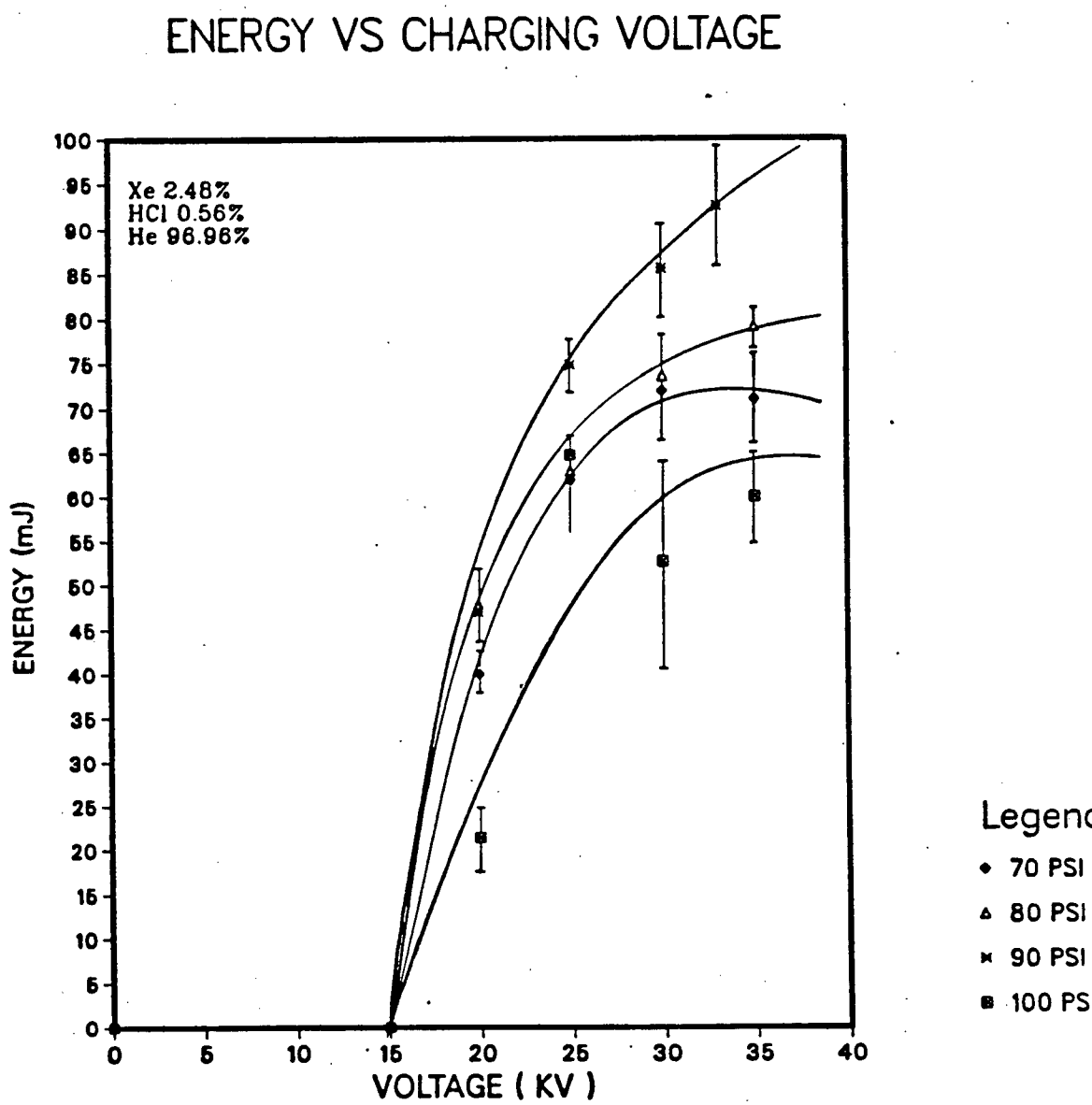

Figure 4.8: Output energy versus charging voltage.

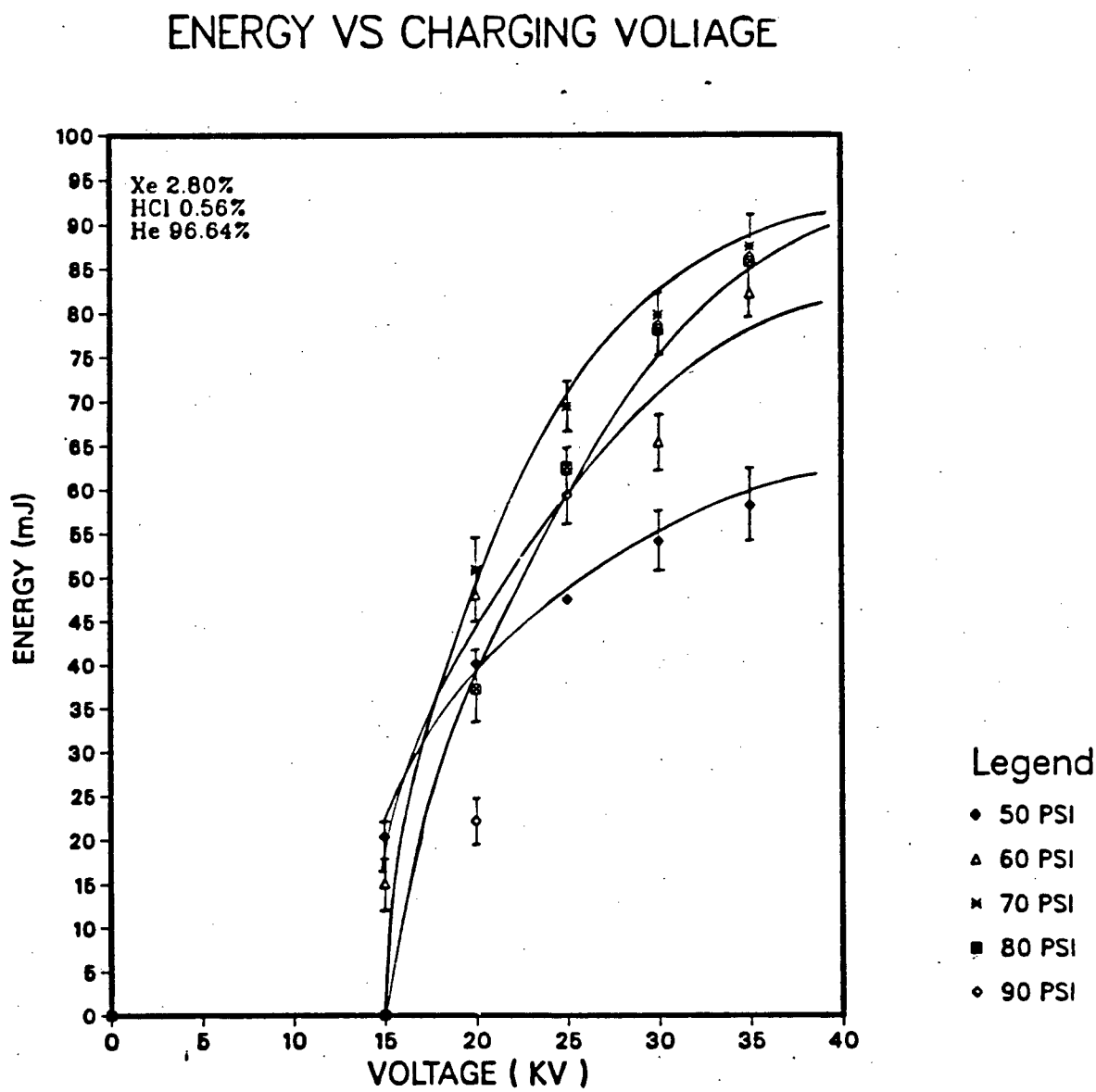

Figure 4.9: Output energy versus charging voltage.

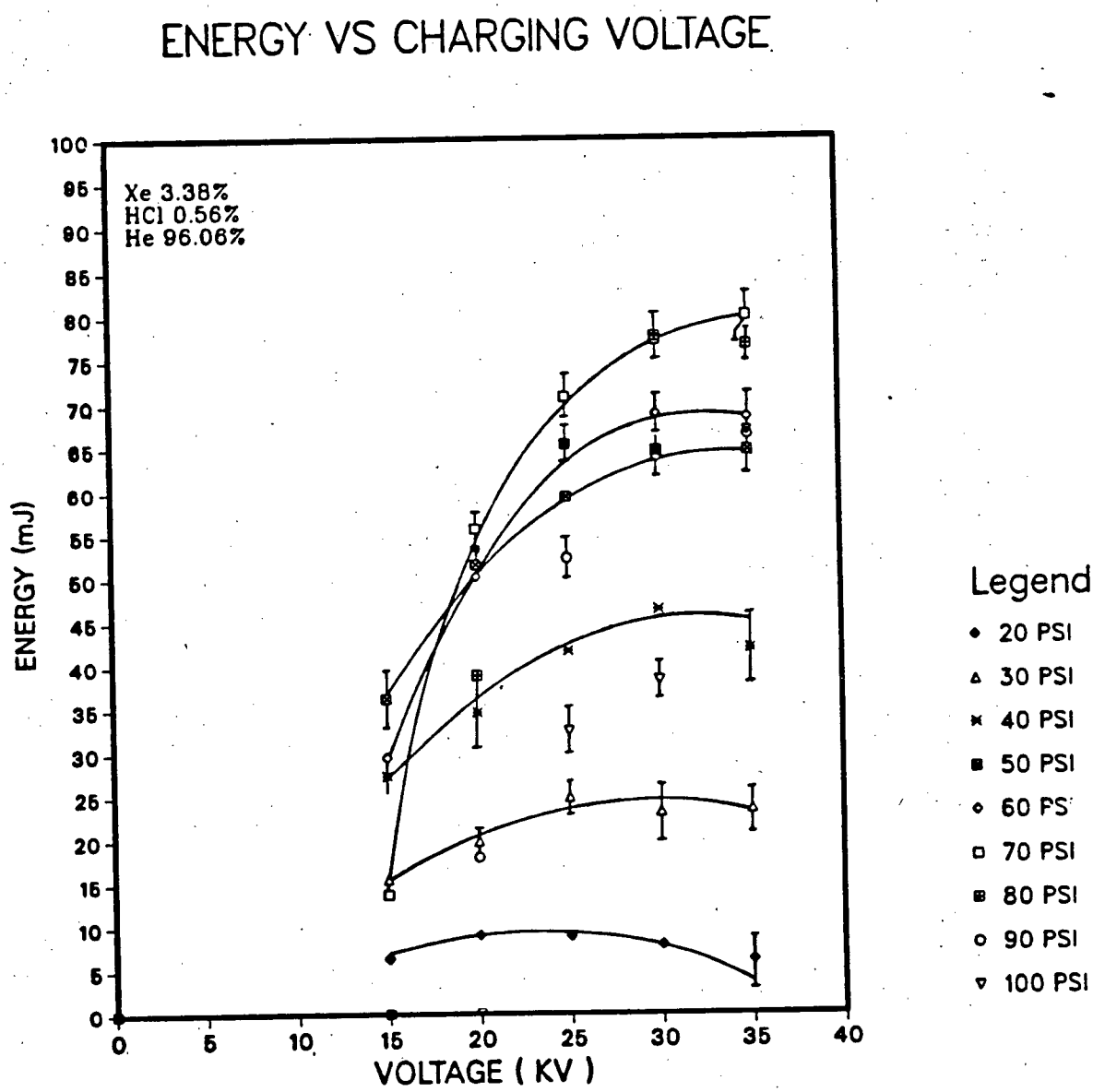

Figure 4.10: Output energy versus charging voltage.

For some concentrations and charging voltages, there is a maximum filling pressure above which the laser output energy starts to roll over. And the divergence of the curves, in some mixes, at a high pressure, suggests a relatively small change in the gas pressure or charging voltage results in large changes of the output energy.

The optimum pressure chosen for the parametric studies was 80 Psi. At such a pressure, the laser showed uniform glow discharges and higher output energies for all the concentrations.

Most likely, one can attribute the decrease in the output energies at higher pressures to the formation of the triatomic molecule Xe_2Cl^* via this reaction:

$$XeCl^* + Xe + He \longrightarrow Xe_2Cl^* + He \tag{4.1}$$

The Xe_2Cl^* forms via collisions of three bodies (Xe, He, and $XeCl^*$), which increases with increasing the total filling pressure. The triatomic molecule absorbs at the laser wavelength [6]; therefore, at high pressures, Xe_2Cl^* may build up to a sufficient density to reduce the laser output energy.

4.3 Variations of Energy with Xe/HCl/He Concentrations

The concentrations of Xe and HCl are key factors in the kinetics of the $XeCl$ laser. The energy deposition rate, the glow discharge stability, and the output energy all depend on the concentration of Xe and HCl. For example, changing the concentration of HCl will alter the rate of energy transfer to the lasing gas. This is a result of changing the discharge impedance; therefore, the impedance coupling between the laser discharge load and the electric circuit will vary accordingly, thus, decreasing the efficiency of the energy transfer from the capacitor banks to the lasing gas. In regard to the electrical efficiency,

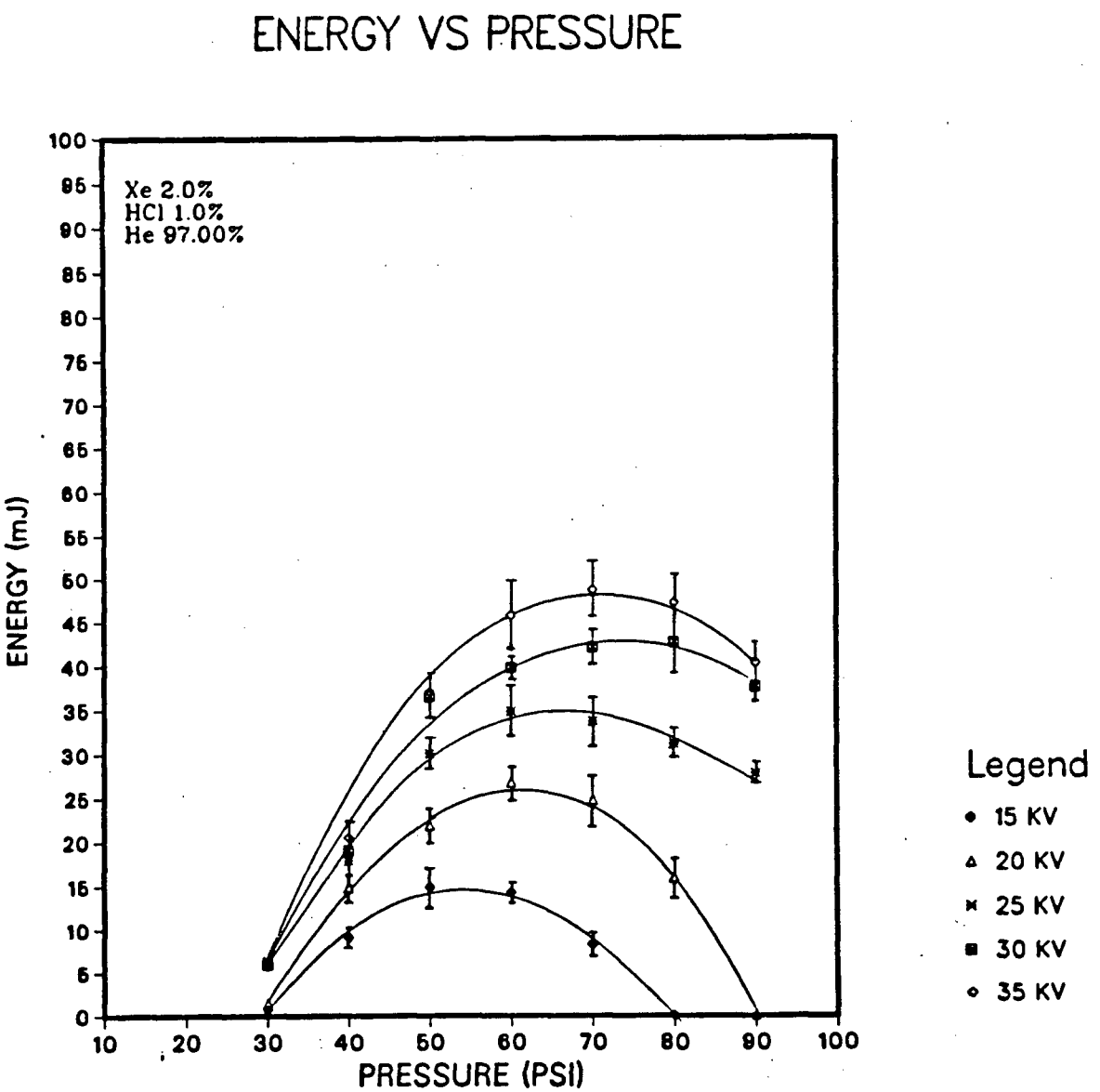

Figure 4.11: Output energy as a function of total gas pressure.

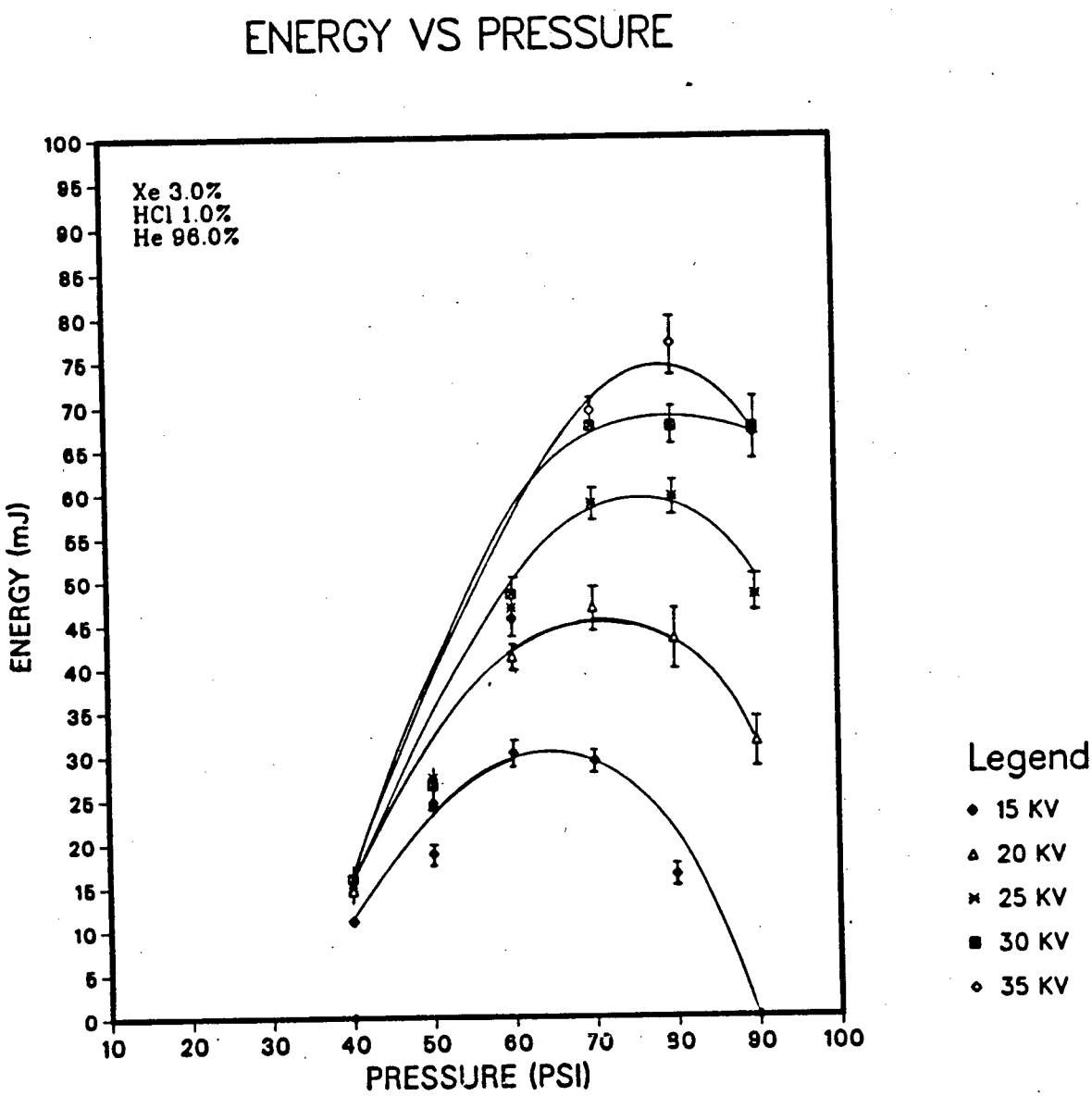

Figure 4.12: Output energy as a function of total gas pressure.

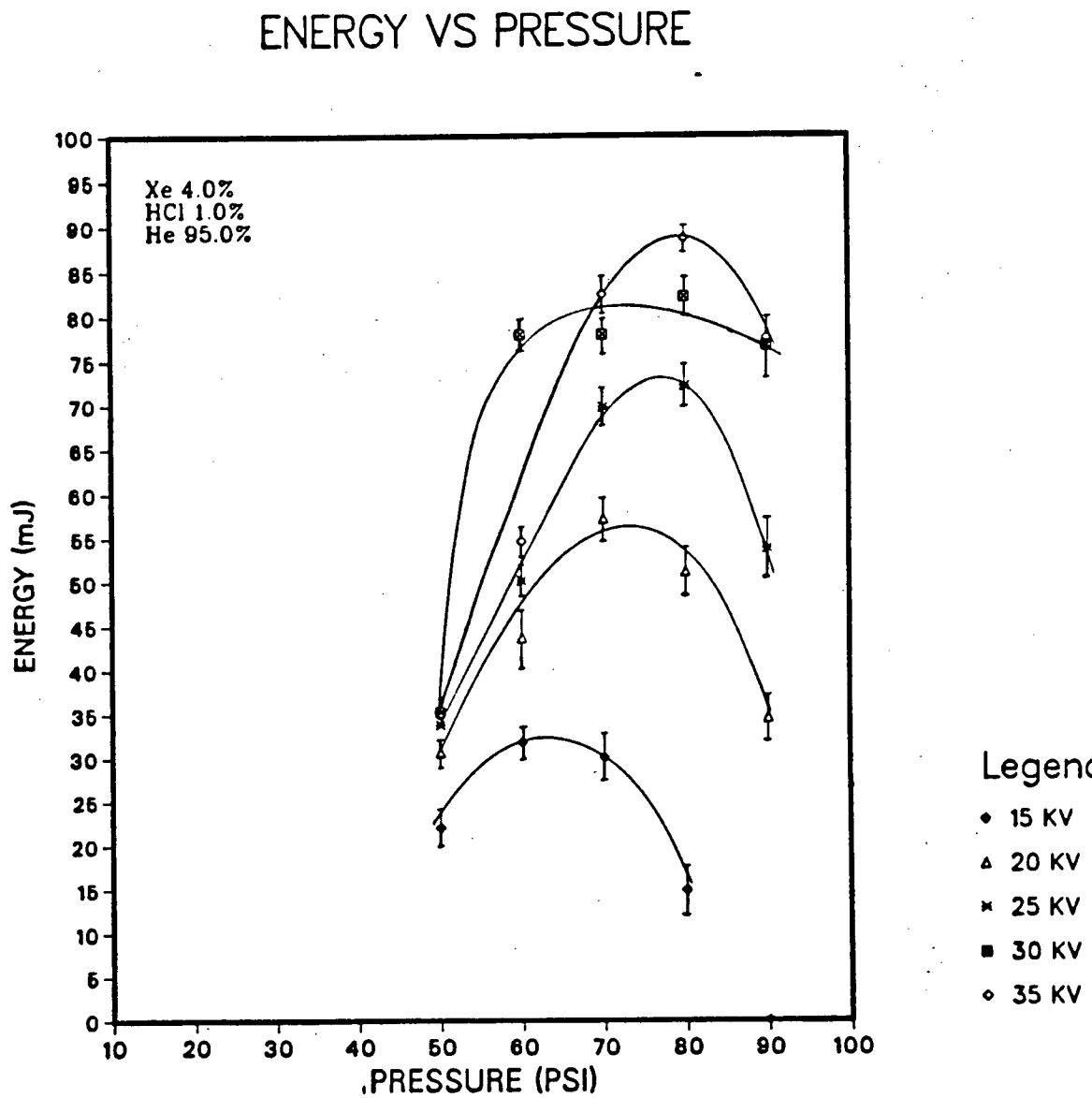

Figure 4.13: Output energy as a function of total gas pressure.

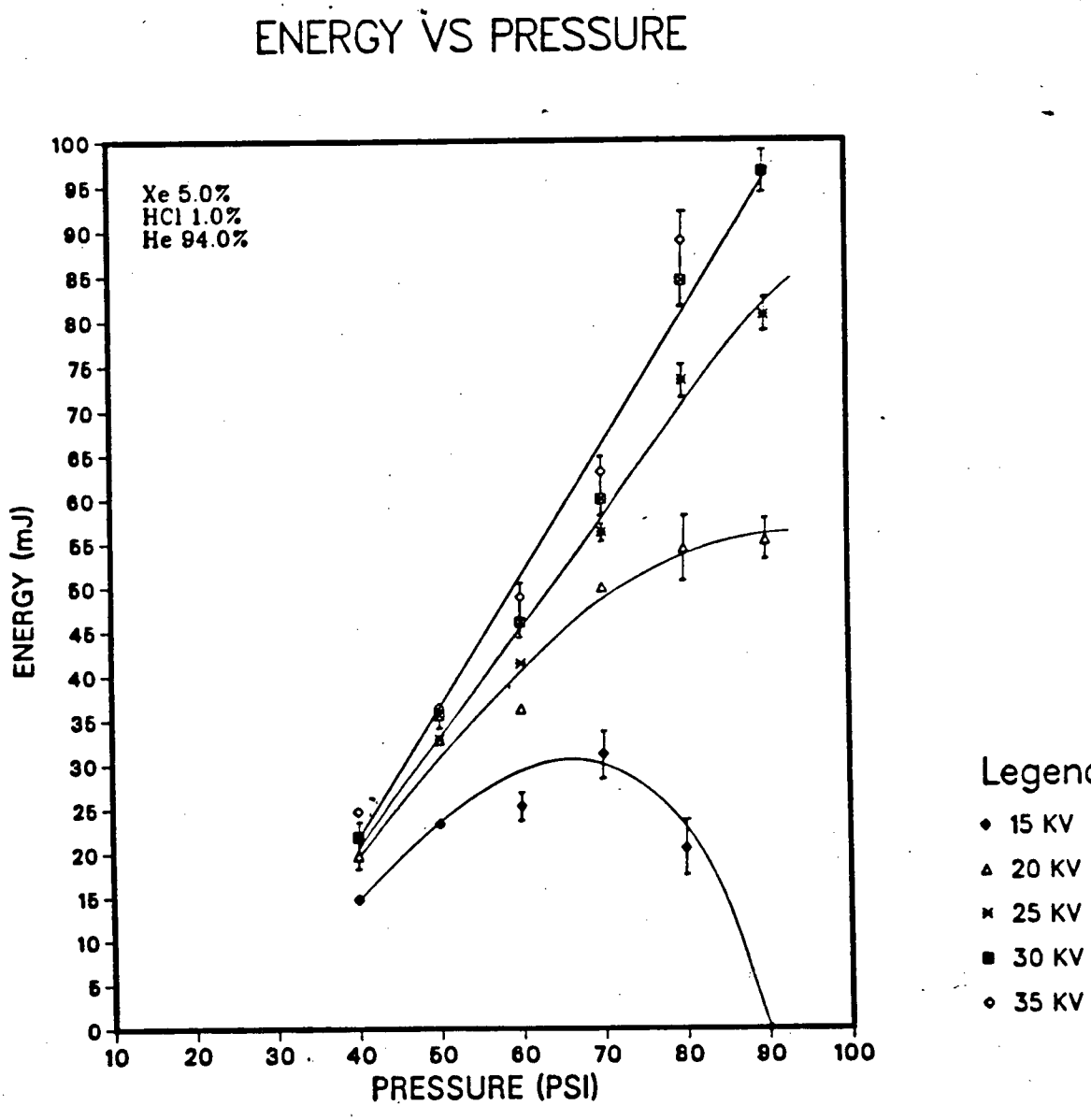

Figure 4.14: Output energy as a function of total gas pressure.

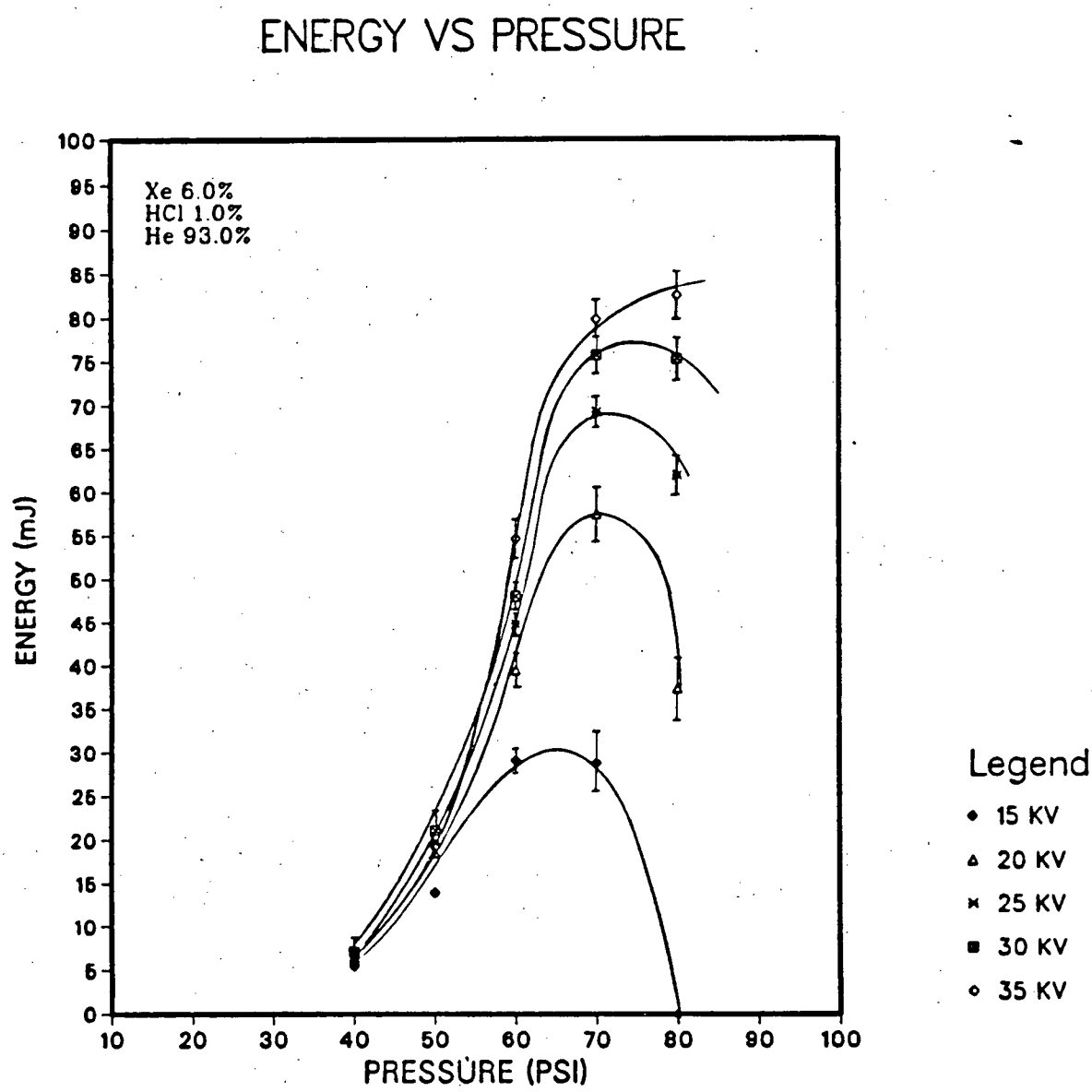

Figure 4.15: Output energy as a function of total gas pressure.

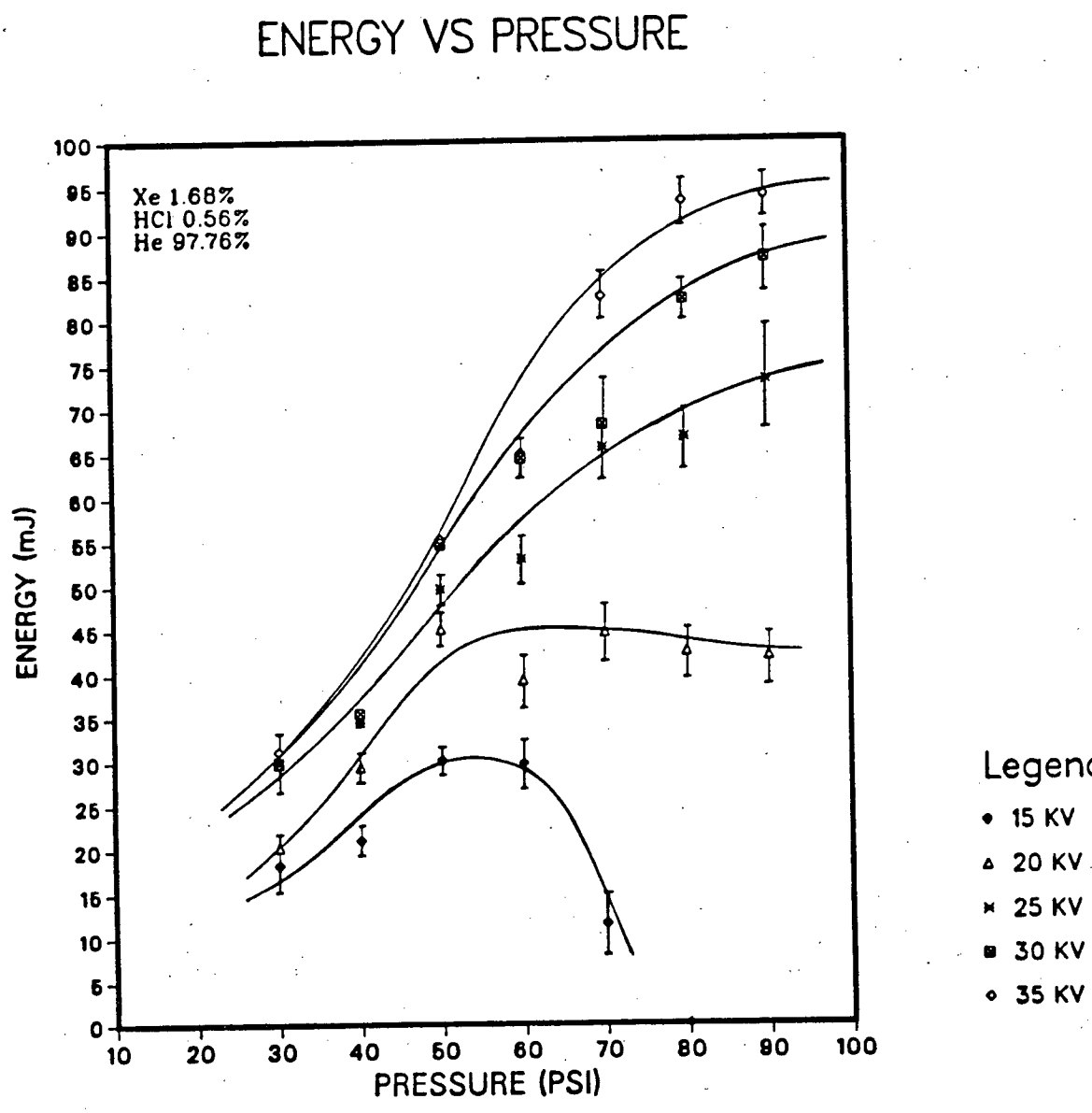

Figure 4.16: Output energy as a function of total gas pressure.

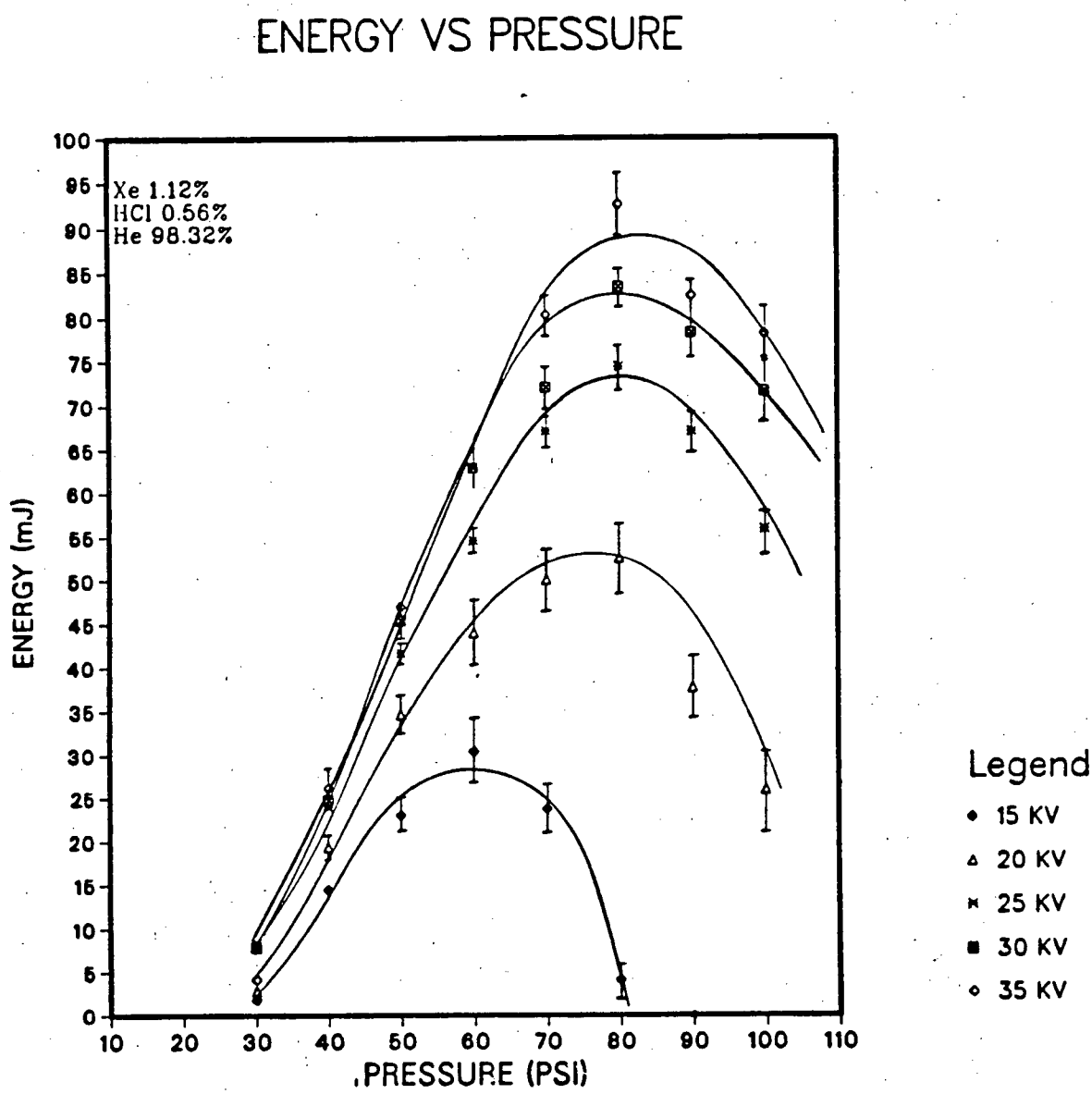

Figure 4.17: Output energy as a function of total gas pressure.

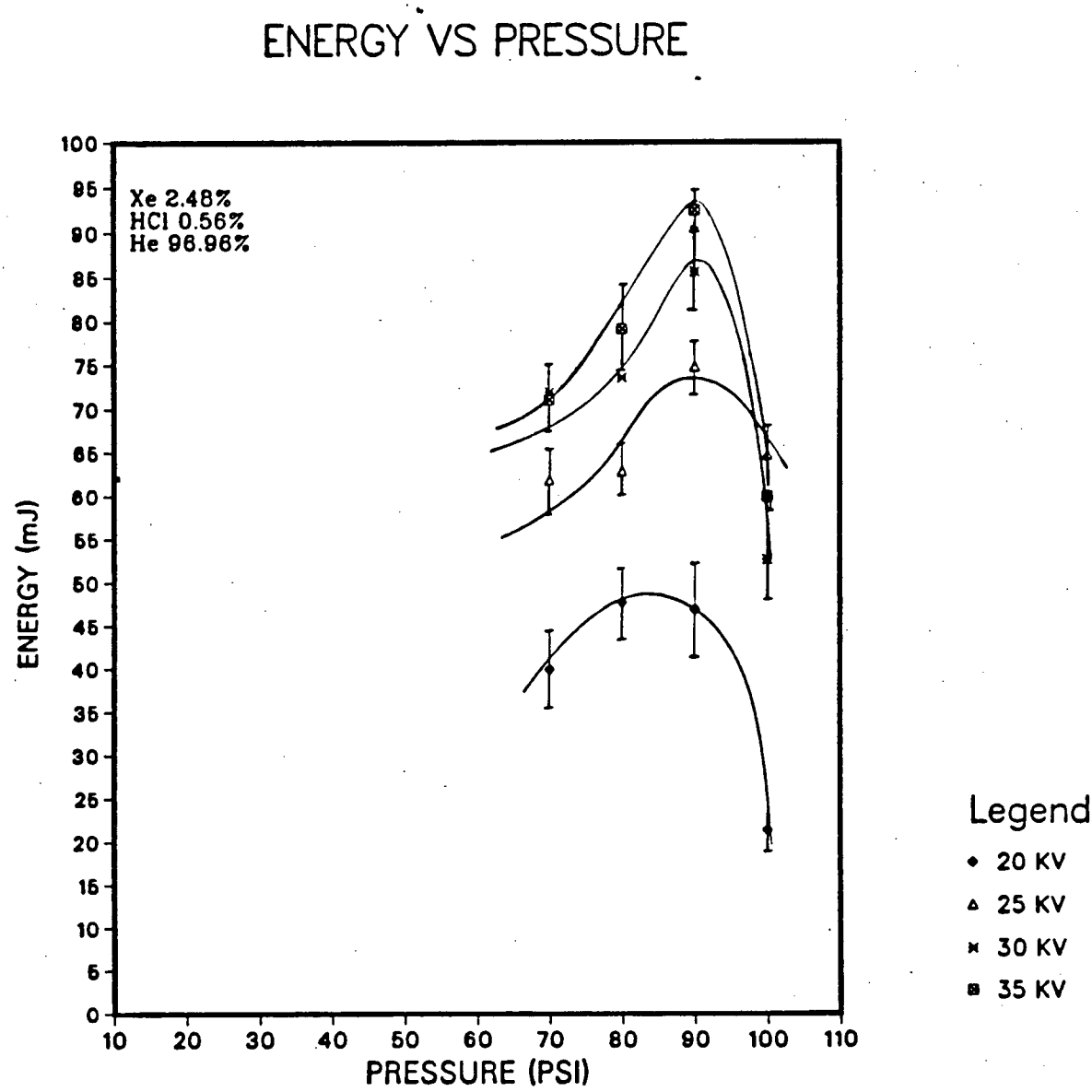

Figure 4.18: Output energy as a function of total gas pressure.

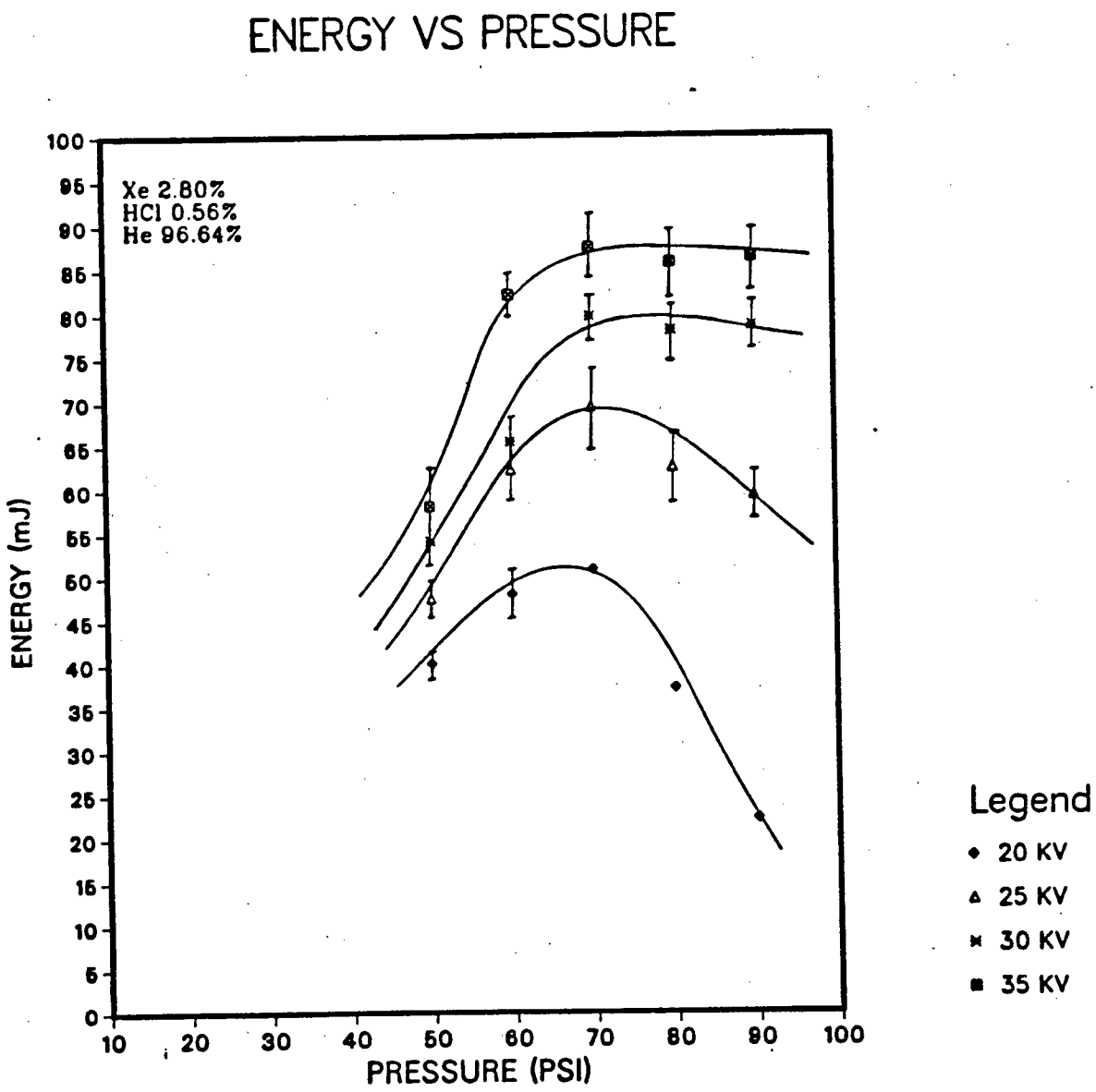

Figure 4.19: Output energy as a function of total gas pressure.

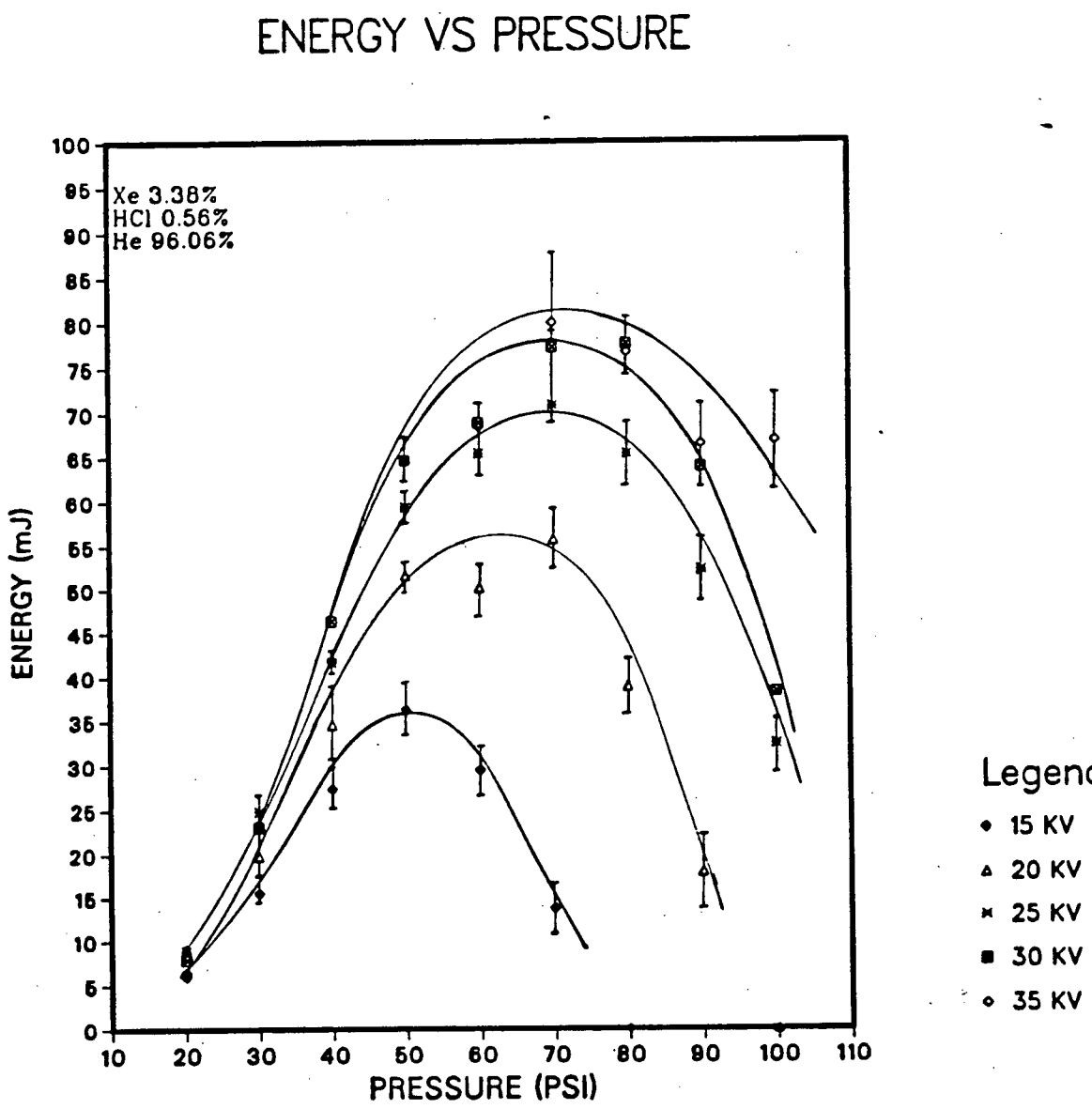

Figure 4.20: Output energy as a function of total gas pressure.

determining the best concentrations of Xe and HCl is an essential step in maximizing the laser output energy.

The glow discharge is found to be extremely sensitive to the lasing gas mixture composition, especially, the concentration of HCl gas. For higher concentrations of HCl > 1%, it was difficult to operate the laser in a glow discharge manner; on the other hand, using low HCl concentrations < 0.5% resulted in a stable glow discharge but low output energies. So it was decided to study the laser behaviour at 0.56% and 1% HCl concentrations at different Xe concentrations.

Figures (4.21) to (4.24) show the behaviour of the laser output energy with the Xe:HCl ratio for constant HCl concentration of 1% and a pressure ranging from 50 *Psi* to 80 *Psi* of the total gas pressure. At a pressure of 50 *Psi*, there was a decrease in energy for Xe:HCl ratio of 3 at higher voltages (25 to 30 *KV*). By increasing the pressure to 60 *Psi*, a dip in the energy curves can be seen at a Xe:HCl ratio of 5, consistent for all charging voltages for which we have no explanation. The reduction in energy was approximately 15%, and by increasing the total pressure to 70 *Psi*, a similar behaviour was observed (except at 15 *KV*) at the same Xe:HCl ratio, where the decrease in energy was approximately 20%. At a gas pressure of 80 *Psi*, the energy curve showed smooth rollover at high charging voltages. This suggests that the maximum Xe:HCl ratio that gives the optimum energy is 4. The rollover can be explained by the increase rate of formation of Xe_2Cl^*, Xe_2^*, and Xe_2^+ [52], which have high u.v. absorption cross sections at the lasing wavelength. With the increase of Xe percentage and total gas pressure, the rate of formation of these molecules increases. In general, for a fixed HCl concentration of 1%, we conclude that at high voltages and a Xe:HCl ratio $\geq$ 4.5, the laser output energy decreases by more than 10% due to increase of Xe concentration.

Figures (4.25) to (4.27) show the laser energy as a function of Xe:HCl ratio for a constant HCl percentage of 0.56%. At a total pressure of 70 *Psi*, the energy shows a

minimum at Xe:HCl ratio of 4.4, which is consistent at all charging voltages. By increasing the gas pressure to 80 *Psi*, a maximum output energy was obtained at a low Xe:HCl ratio of 2; an increase of this ratio results in the decline of the output energy. The same behaviour was observed at 90 *Psi*; however, at this pressure, the glow discharge was unstable.

Finally, we decided to operate the laser at conditions producing the best uniform glow discharge, with maximum output energy, at a mixture of Xe=1.12%, HCl=0.56%, and He=98.32%, at a total gas filling pressure of 80 *Psi* and at a charging voltage of 30 *KV* with 600 *nsec* main discharge delay.

4.4 Pulse Shape

The laser pulse duration was monitored by a *Hamamatsu R1193U.03* phototube with a rise time of less than 1 *nsec*; the phototube was biased at +1000 volts. The temporal behaviour of the laser pulse was displayed on a 7104 *Tektronix* oscilloscope using a 7A19 fast plug in. Neutral density filters were used to attenuate the laser pulse intensity in order to avoid the saturation of the phototube.

A series of measurements were made at 50 *Psi*, 60 *Psi*, and 80 *Psi* of the total lasing gas pressure and at the full optimum lasing concentrations of each of Xe (1.12%), HCl (0.56%), and He (98.32%). The output pulse full width at half maximum ($FWHM$) is found to be an increasing function of the total gas pressure, with the charging voltage and the time delay being constants. This is the same behaviour observed by Mingchao [53] with a similar discharge circuit.

At a total pressure of 50 *Psi*, the pulse shape appears to be consistent all the time: Six runs of the laser pulse were taken; all show a sharp-peaked pulse (Figure (4.28a))

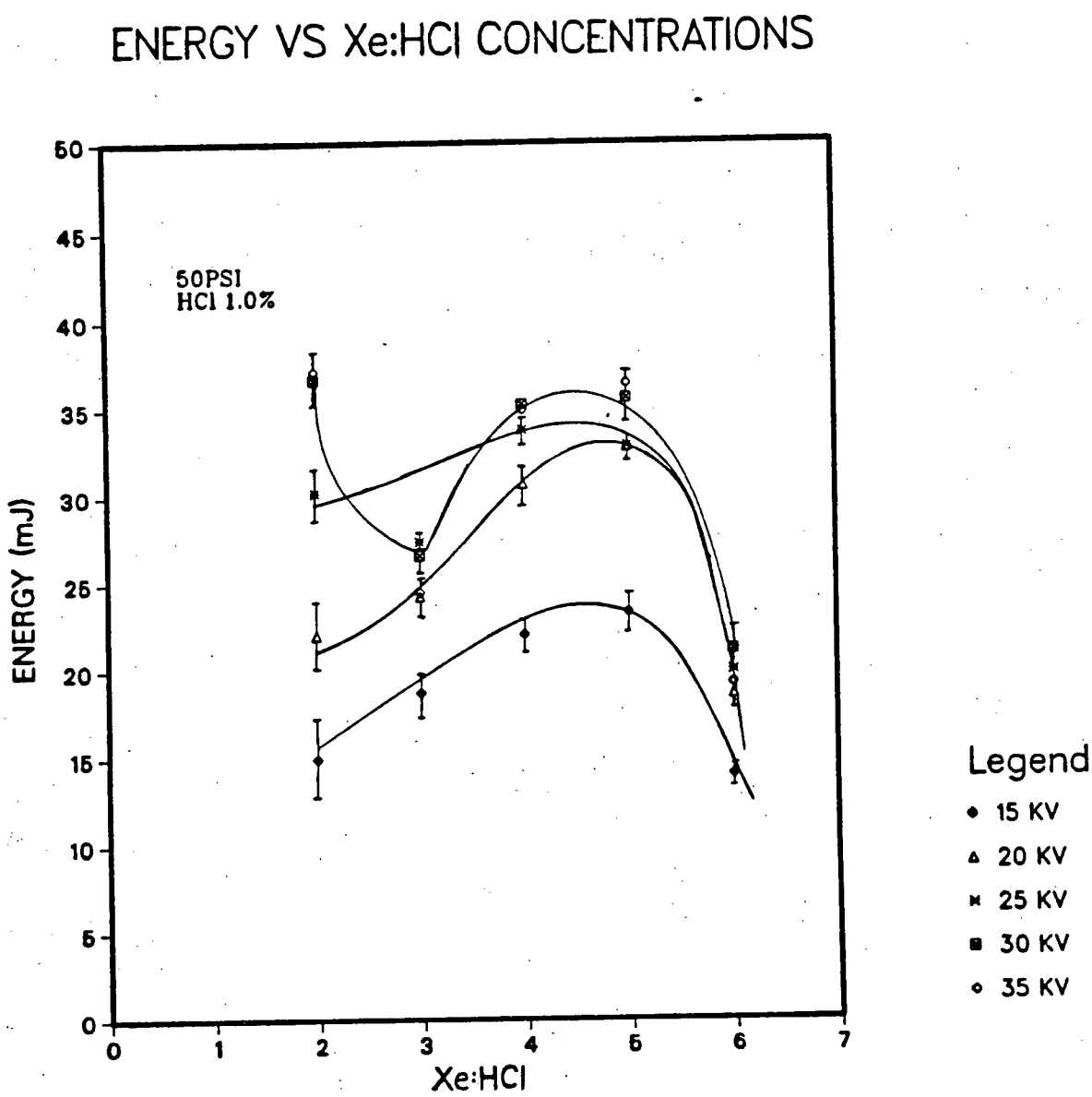

Figure 4.21: Output energy versus Xe:HCl ratio (50 Psi, 1%(HCl)).

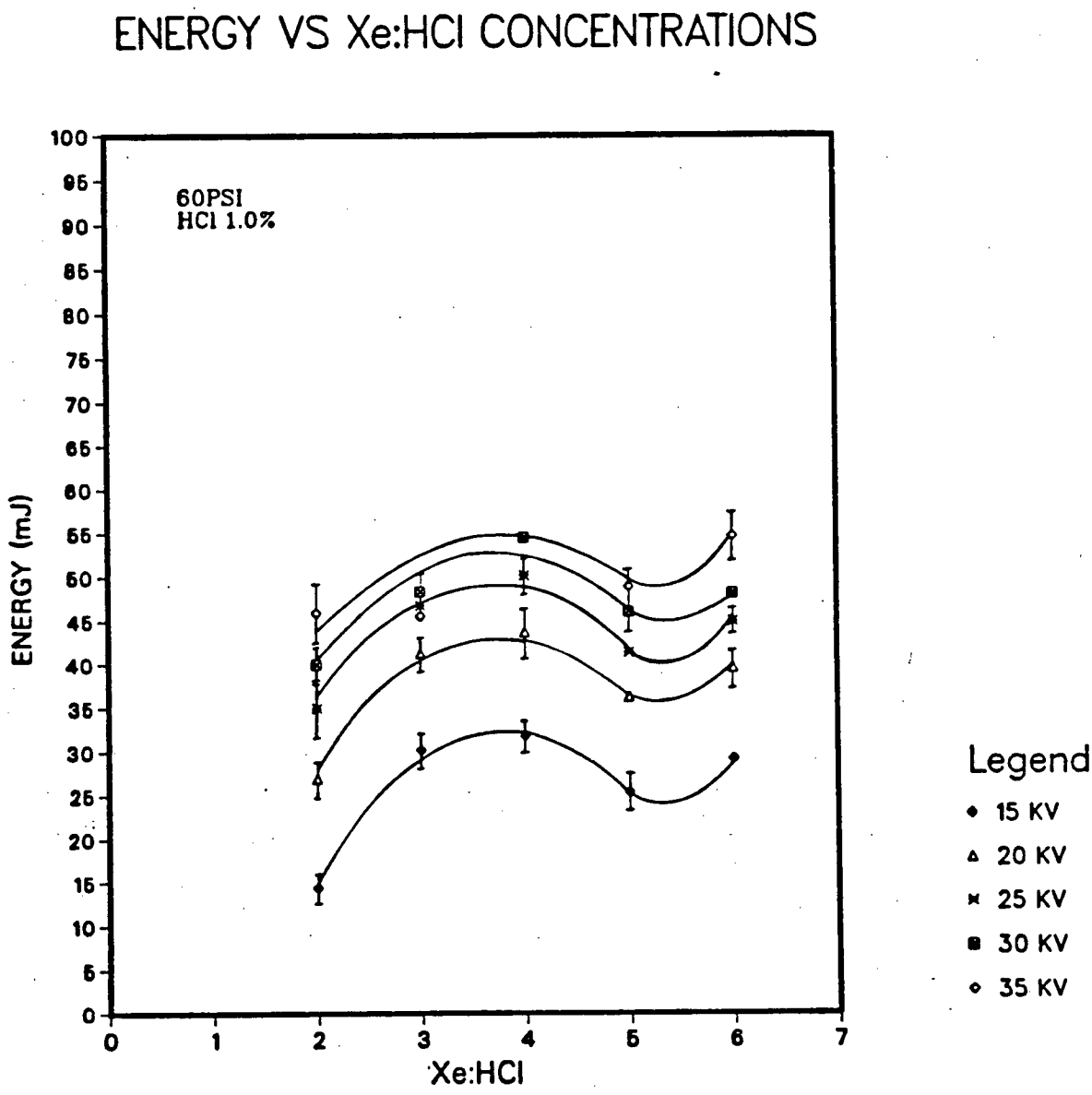

Figure 4.22: Output energy versus Xe:HCl ratio (60 Psi, 1%(HCl)).

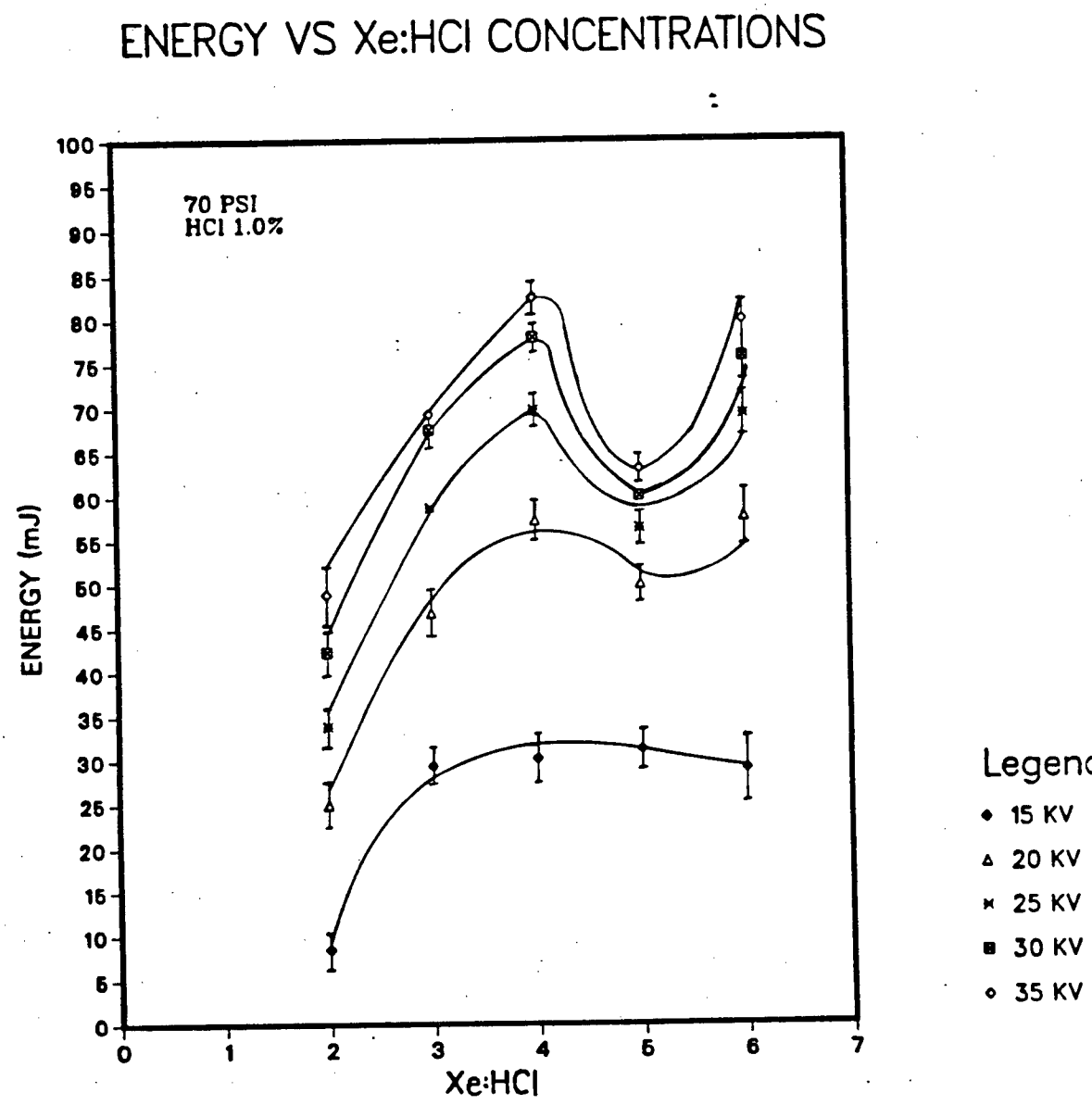

Figure 4.23: Output energy versus Xe:HCl ratio (70 Psi, 1%(HCl)).

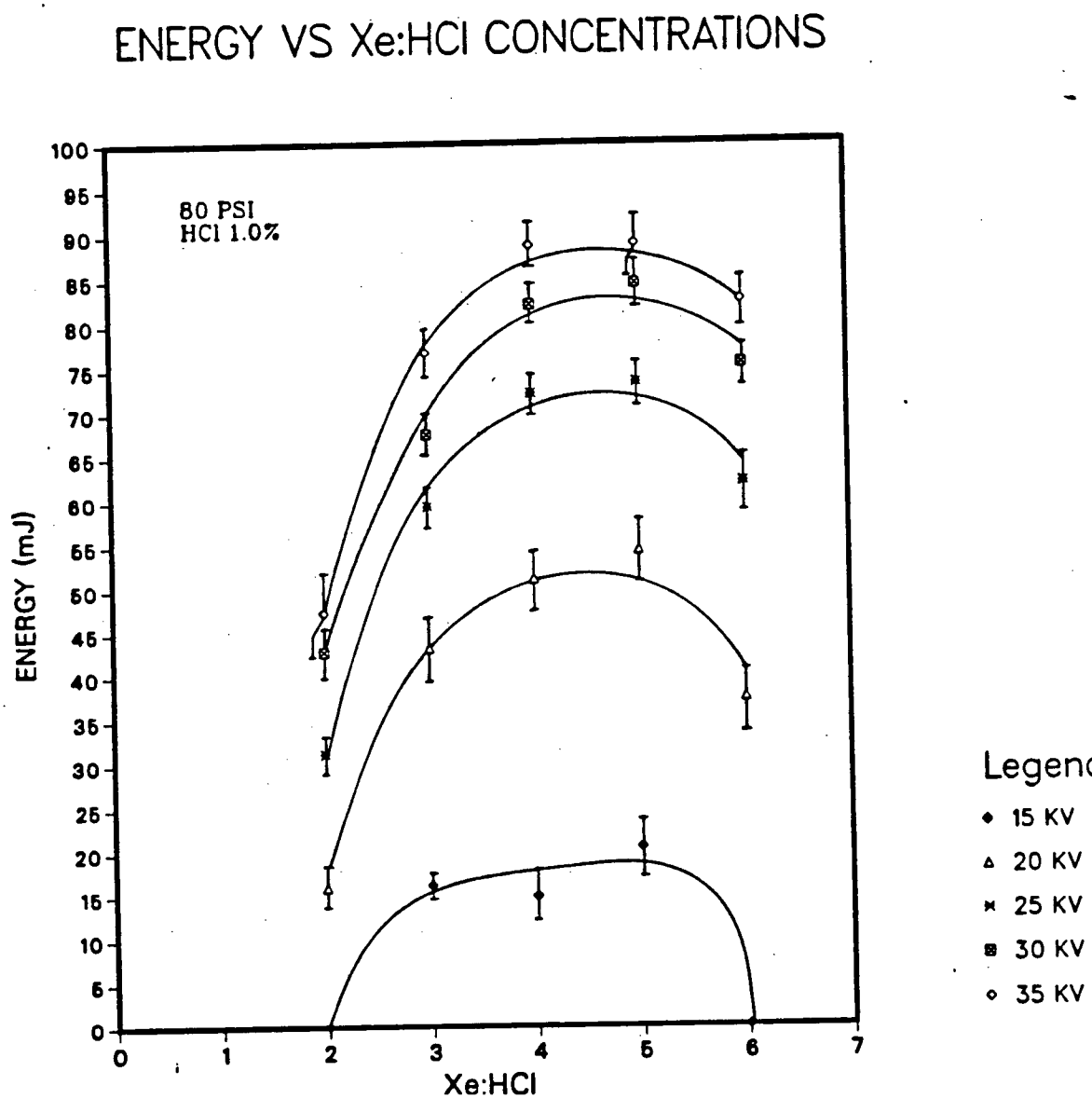

Figure 4.24: output energy versus Xe:HCl ratio (80 Psi, 1%(HCl)).

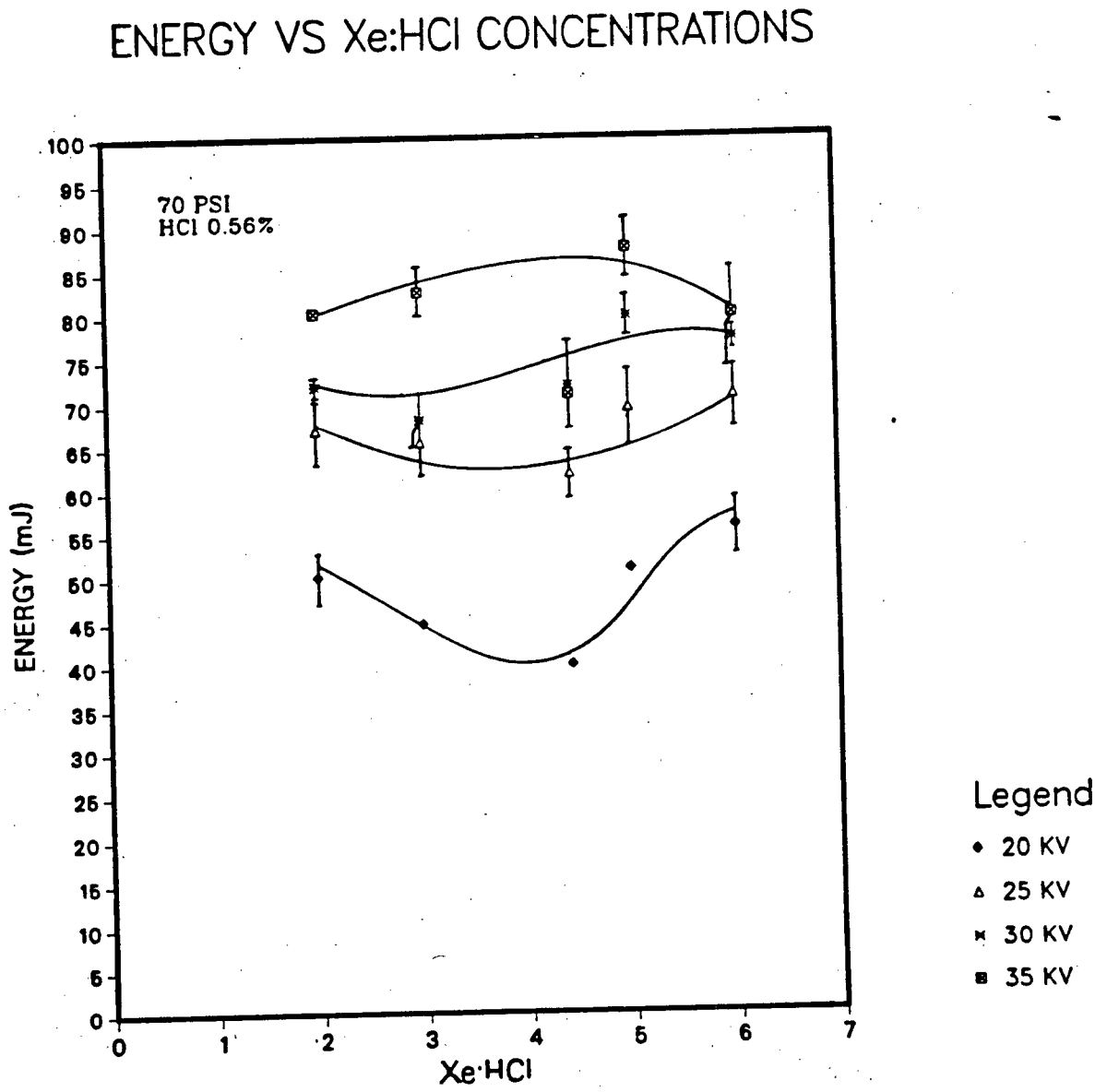

Figure 4.25: Output energy versus Xe:HCl ratio (70 Psi, 0.56%(HCl)).

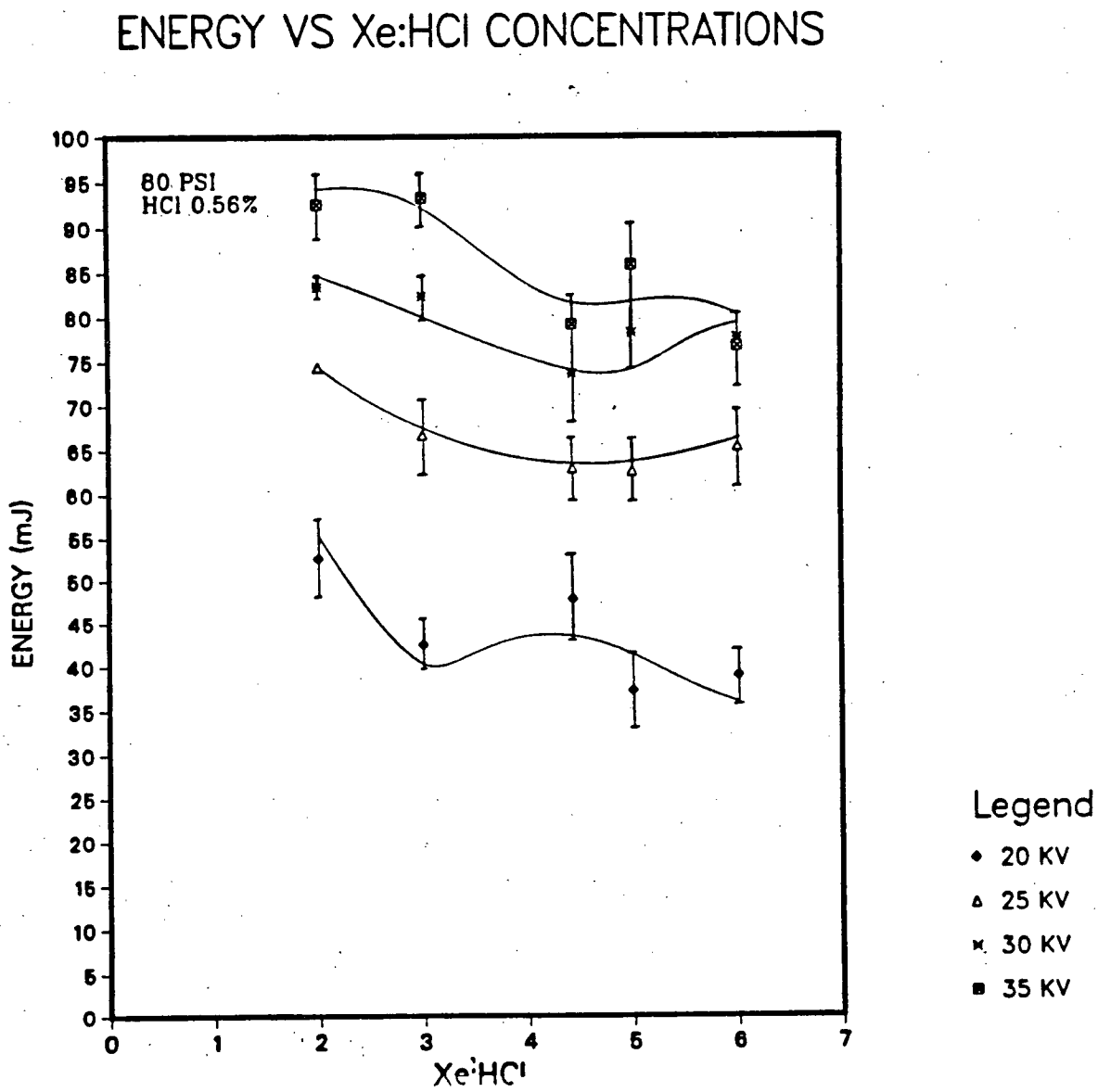

Figure 4.26: Output energy versus Xe:HCl ratio (80 Psi, 0.56%(HCl)).

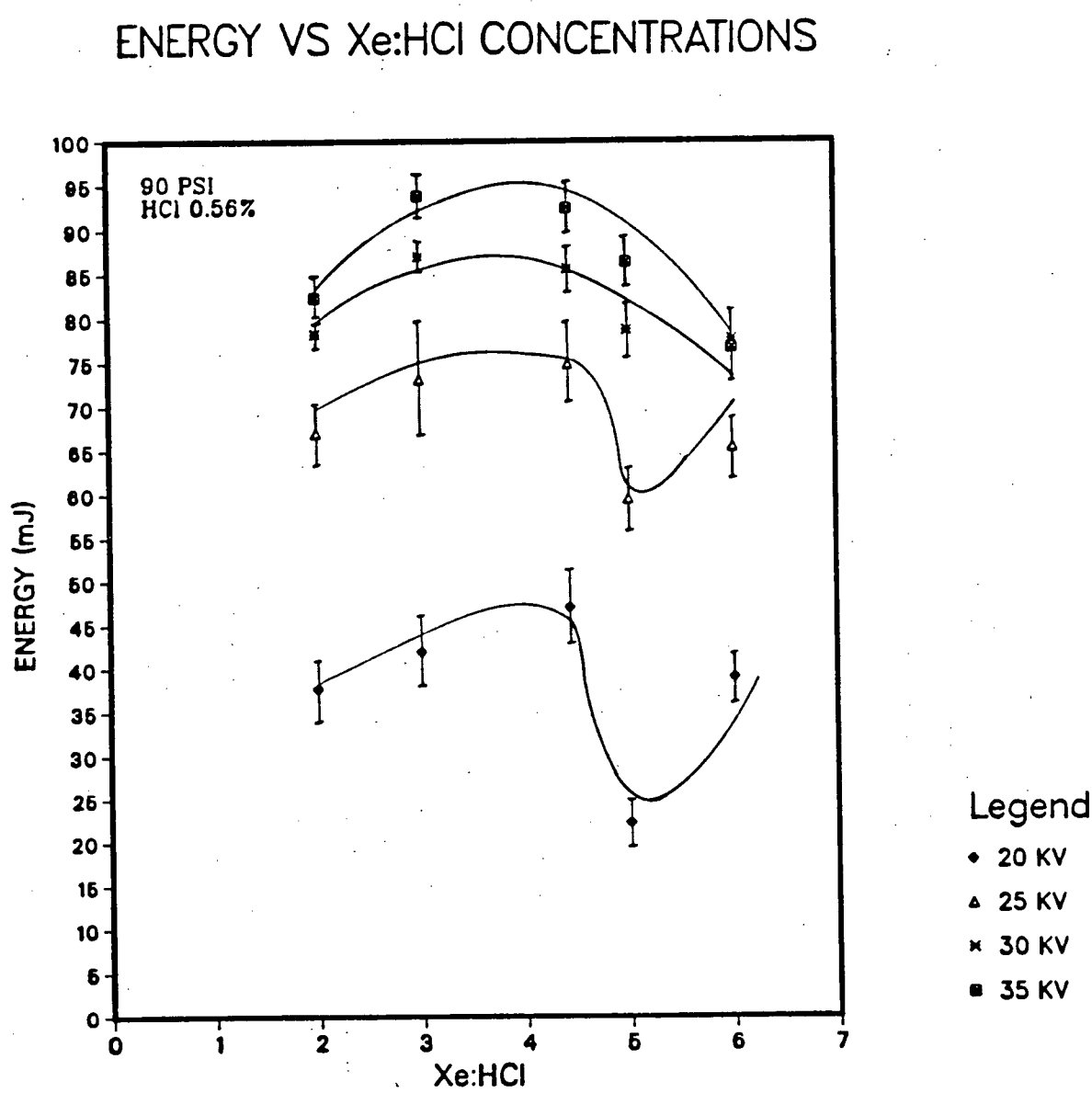

Figure 4.27: Output energy versus Xe:HCl ratio (90 Psi, 0.56%(HCl)).

with a rise time of 4 *nsec*. At this pressure, the *FWHM* was measured to be 9.2 *nsec* with a foot to foot pulse width of 30 *nsec*. The pulse was free of any temporal modulations. However, at higher pressures, the pulse shape changes: At a pressure of 60 *Psi* the laser pulse appears to be double peaked, as seen in figure (4.28b), with a shorter rise time of 2 *nsec*. The pulse *FWHM* was 12.8 *nsec* with 30 *nsec* foot to foot duration.
When the laser was pressure optimized to 80 *Psi* for maximum energy output, some characteristic modulation features appeared on the peak of the pulse profile. The pulse *FWHM* was measured to be 13.5 *nsec*, with a foot to foot pulse duration of 28 *nsec*. See figure (4.28c).

One can conclude that two important parameters affect the *XeCl* laser pulse shape: The overall lasing gas pressure and the Q factor of the cavity. The individual pulses, or low modulations, are mainly associated with the round trip time of the photons in the cavity, because the separation between the modulations matches the round trip time around the cavity. In this laser, superradiance was occasionally observed with the output quartz coupler removed and the total rear reflector in place. But the output energy was not measured when the laser was operating in a superradiance manner.

An interesting *IR* pulse was also observed in this lasing mixture with a *FWHM* of 2 *nsec* and a foot to foot width of 5 *nsec*. For more details on this emission and detection technique refer to chapter 6.

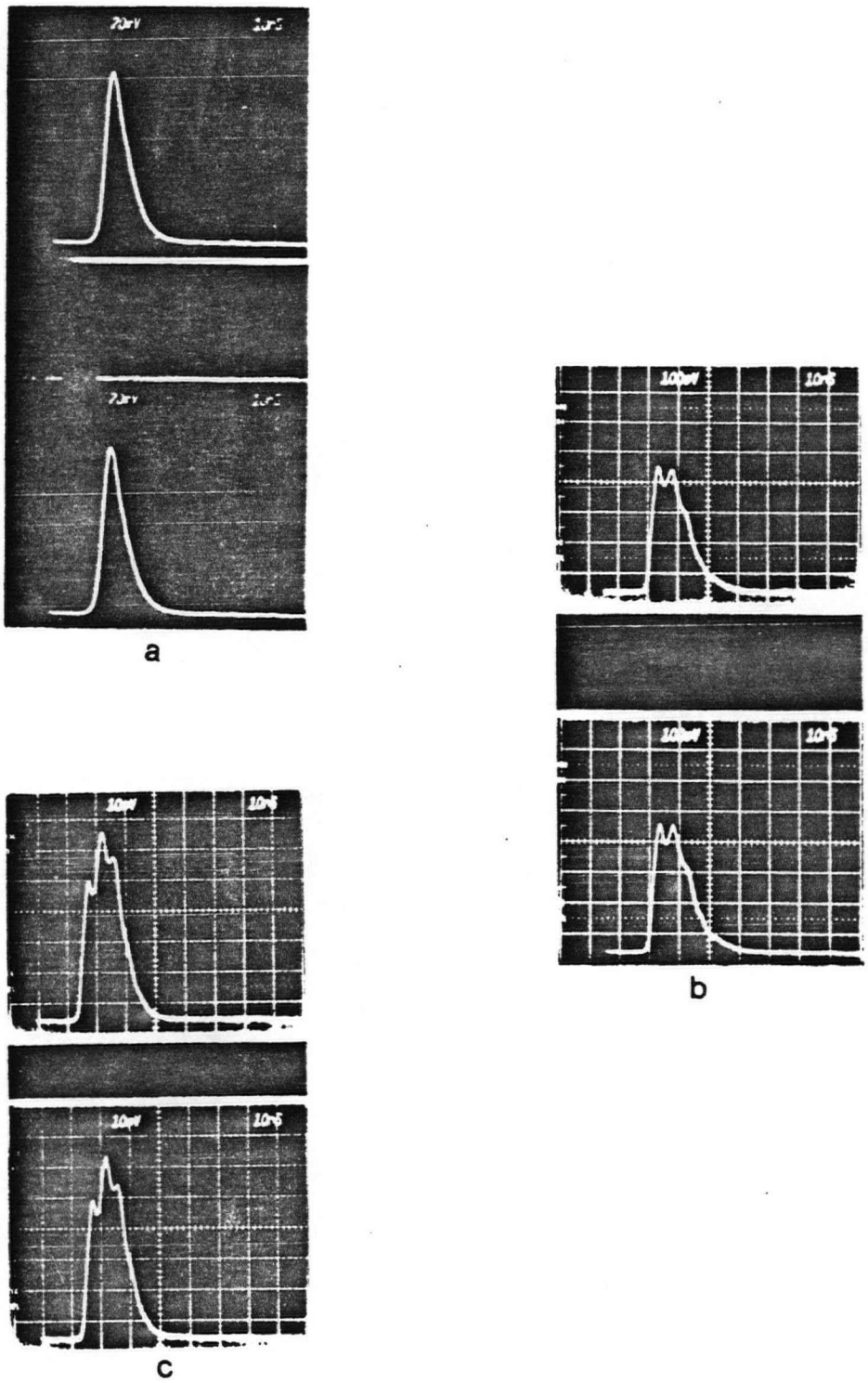

Figure 4.28: Laser pulses (a) 50 Psi, (b) 60 Psi, (c) 80 Psi all at (1.12% Xe, 0.56% HCl,98.32% He).

Chapter 5

Electrical Measurements

In this chapter, we will describe the measurements of some electrical properties of the laser discharge plasma. Such properties include the discharge breakdown voltage, the total current through the plasma, and the discharge resistance. Variations of these parameters with the total gas pressure and composition were studied.

In all the electrical measurements, the oscilloscope was triggered by a photomultiplier (PMT). A single optical fiber was mounted on the top of the main discharge switching spark gap, delivering enough light to the PMT housed inside the screened room. The delay of the PMT stages was measured to be 18 $nsec$.

Moreover, the delay due to optical fiber, was adjusted to be just right in order to trigger the oscilloscope at the start of the voltage trace in the screened room.

Optical triggering is jitter-free and more reliable than using the voltage trace for triggering.

5.1 Current Measurements

The discharge current is an essential electrical parameter for calculating the discharge resistance and it needs to be investigated. The current rise time is directly related to the rate of energy deposition, where the lower the inductance of the circuit, the faster is the current rise time.

In the laser discharge, the electric current changes very quickly; this induces a varying

magnetic field. Therefore, by taking advantage of this, a satisfactory current measurement using a pick up coil should be easily performed. A *Rogowski* pick up coil, 10 *cm* long, consisting of ten turns wrapped around a nylon tube, was used. The coil was housed inside a $\frac{1}{2}$ *inch* piece of poly-flo tubing for electrical insulation, and was connected to a $RG-58$ coaxial cable.

The pick up coil was placed inside the laser loop between the PVC laser chamber and the high voltage charging plate, in the vicinity of the discharge current to be measured. The change in the magnetic field of the main discharge induces an electromotive force $-\frac{d\Phi}{dt}$, where Φ is the magnetic flux through the coil loop. The emf signal produced by the magnetic flux is proportional to the time derivative of the current pulse $\frac{di}{dt}$. The resulting signal was attenuated 75 times, and was displayed on a 7104 *Tektronix* oscilloscope using a 7A22 plug in.

To obtain an absolute calibration of the *Rogowski* coil, the $\frac{di}{dt}$ signal had to be integrated twice to obtain the total amount of charge flowing through the discharge plasma. By comparing the total charge stored in the capacitor banks with the calculated one, we were able to obtain the proportionality constant K of the coil.

$$V_{ind} = K\frac{di}{dt} \tag{5.1}$$

where V_{ind} is the induced emf signal in volts,
K is the *Rogowski* coil proportionality constant, and
i is the current flowing through the discharge.

The total current is

$$\int_0^t \frac{V_{ind}}{K} dt = i = \frac{A}{K} \tag{5.2}$$

where $A = \int_0^t V_{ind} dt$ is the area under the current trace.

Next, the total charge passed through the discharge is

$$Q_T = \int_0^t \frac{di}{dt} \tag{5.3}$$

$$Q_T = \frac{1}{K} \int_0^t A dt \tag{5.4}$$

On the other hand, the total charge stored in the capacitors is

$$Q_T = \frac{CV_b}{4} \tag{5.5}$$

where C =64.8 nF, and V_b is the discharge breakdown voltage.

Equating equations (5.4) and (5.5) gives the coil proportionality constant, and by using equation (5.2), one can find the total current passing through the discharge.

Figure (5.1) shows a photograph of the rate of change of the current with time in an optimum mixture composition of Xe, HCl, He of 1.12%, 0.56%, 98.32%, respectively, at a total filling pressure of 80 Psi and a charging voltage of $30KV$. The signals were electronically integrated using the *U.B.C. DIGIT* programme, and were stored for further analysis.

The numerically integrated $\frac{di}{dt}$ signal of figure (5.1) is shown in figure (5.2). The $FWHM$ was 34 $nsec$ with a current peak value of 7.75 KA and a rise time (10%-90%) of 24 $nsec$.

Several measurements were made at quarter, half, three quarters, and full percentages of the optimum concentration at a charging voltage of 30 KV and at a variable total pressure between 40 Psi and 80 Psi in 10 Psi intervals.

In some cases, the current signal showed two peaks; this was also seen in the oscillograms of $\frac{di}{dt}$ (i.e. figure (5.3)). The ringing of the $\frac{di}{dt}$ results in the formation of the second current pulse.

5.2 Discharge Voltage

Measuring the discharge breakdown voltage and current gives an insight into the amount of electrical excitation energy that is being delivered during the laser operation.

In measuring the transient high voltages, it is convenient to use a high voltage divider. In this experiment, the temporal behaviour of the discharge voltage was monitored with a high voltage divider. The high voltage divider consisted of 15 carbon resistors wired in series, giving a total effective resistance of 61 $K\Omega$, and it used the 50 Ω impedance of the oscillscope as part of its circuit. The voltage divider has an attenuation factor of 123. The voltage signal was further attenuated by a factor of 6150, using *Tektronix* voltage attenuators.

The breakdown voltage was studied as a function of the total lasing gas pressure and composition at a charging voltage of 30 KV.

Some measurements were performed in the optimum lasing mixture and at the optimum operating conditions; figure (5.4) shows the voltage signal at the optimum operating conditions.

Operating the laser at the optimum conditions gives a breakdown voltage of 29.1 KV with rise time of 111 $nsec$. Because the breakdown voltage is less than twice the charging voltage, the discharge circuit does not double the charging voltage. That is, the current will start flowing through the discharge when the voltage at the laser electrode reaches the breakdown voltage of the gas. The ringing in the voltage trace is a result of impedance

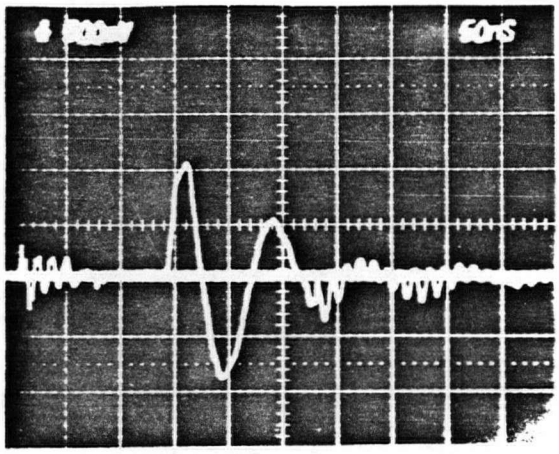

Figure 5.1: Rogowski coil signal attenuated by 75 (0.5v/div), 30 Kv.

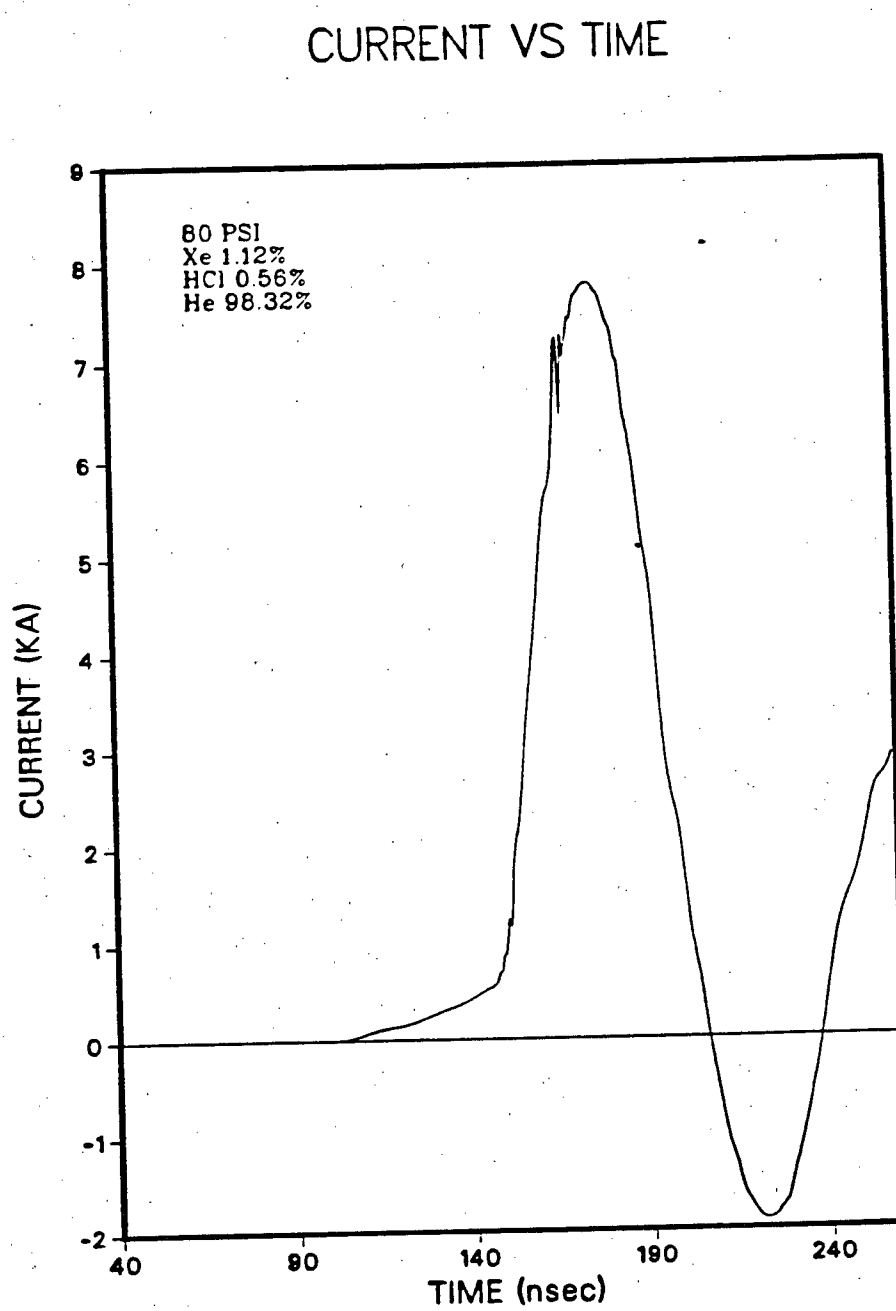

Figure 5.2: The integrated current signal of figure (5.1).

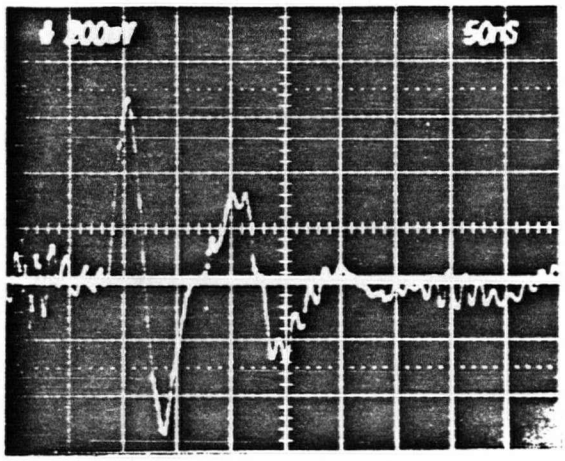

Figure 5.3: $\frac{di}{dt}$ signal (0.28% Xe, 0.14% HCl, 99.58% He).

mismatching between the discharge plasma and the electric circuit.

Several other voltage measurements were performed in quarter, half, and three quarters of the optimum lasing concentration at variable filling pressures.

Finally, by using the above data, we plotted the breakdown voltage as a function of the total gas filling pressure in figures (5.5) to (5.9). As expected, a linear relationship between the breakdown voltage and the total filling pressure is clear. As the concentration of Xe and HCl increased, the breakdown voltages (at the same pressure) did not vary by much; this is because the gas mixture contains mainly He gas, and the low percentages of Xe and HCl do not influence the breakdown voltage.

5.3 Discharge Resistance

The discharge resistance of the $XeCl$ discharge was evaluated by dividing the voltage profile by the current pulse profile starting at the beginning of the current trace. The discharge resistance can be expressed in the following manner provided that the inductance is less than $10^{-7}\ H$.

$$R(t) = \frac{V(t)}{I(t)} \tag{5.6}$$

$$R(t) = \frac{E(t)d}{n_e A e V_d(t)} \tag{5.7}$$

where $V(t)$ is the voltage across the discharge,

$I(t)$ is the current flowing through the plasma,

E is the electric field,

d is the discharge gap separation,

e is the electron charge,

A is the electrode discharge area, and

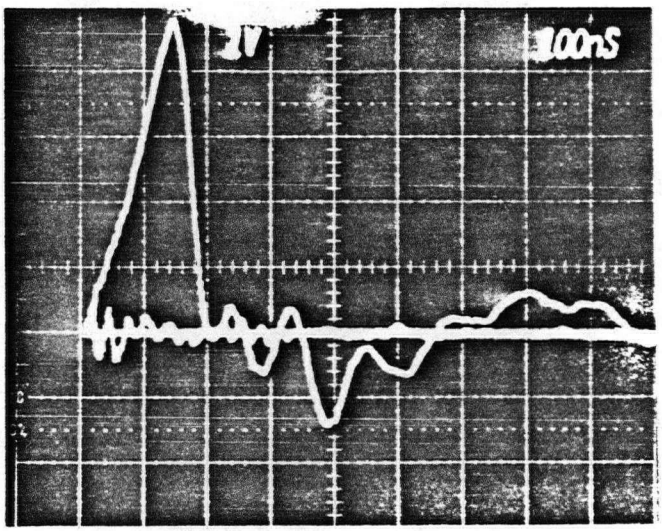

Figure 5.4: Voltage of the main electrodes attenuated by 6150 (1v/div).

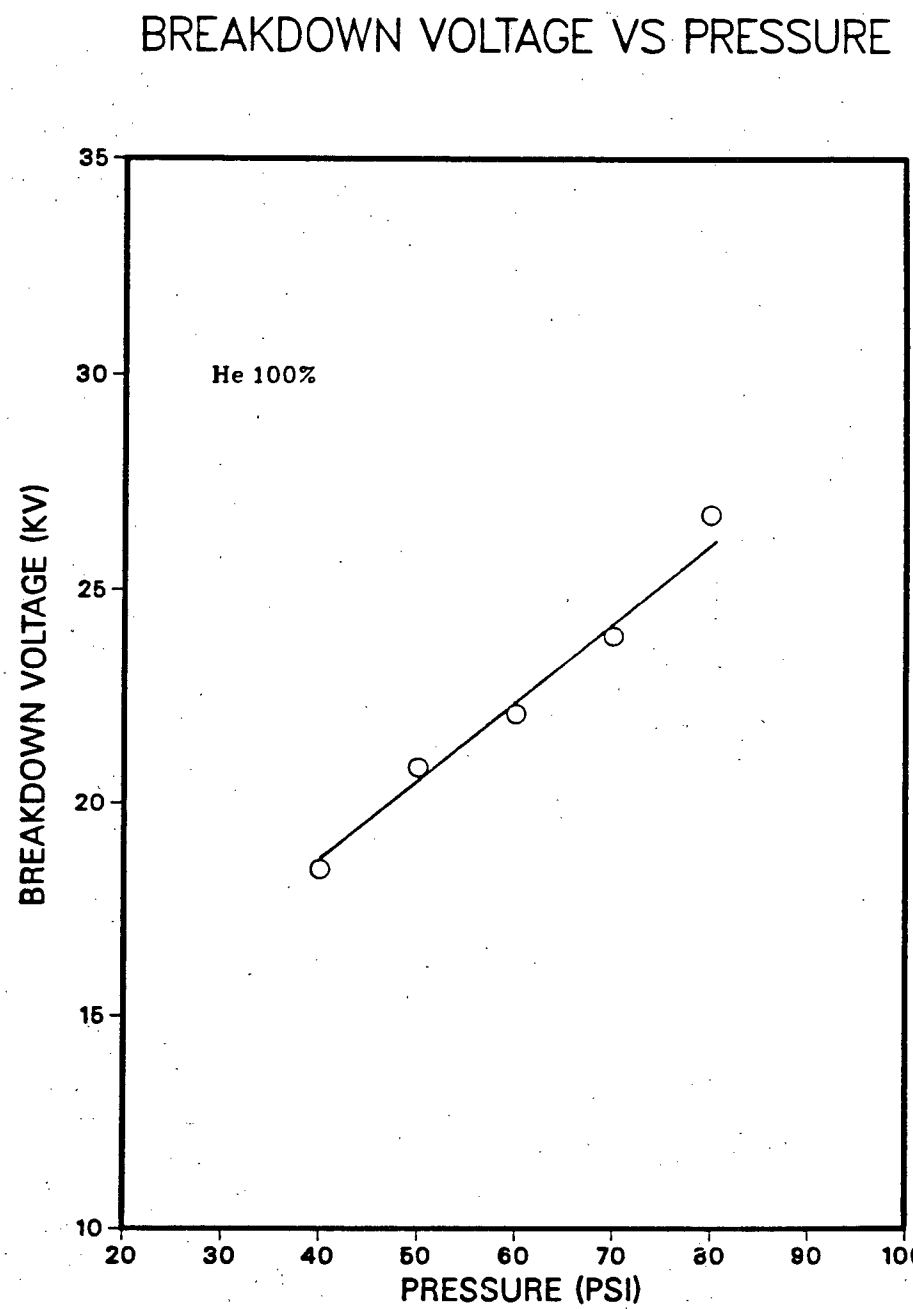

Figure 5.5: The breakdown voltage versus total pressure for pure He.

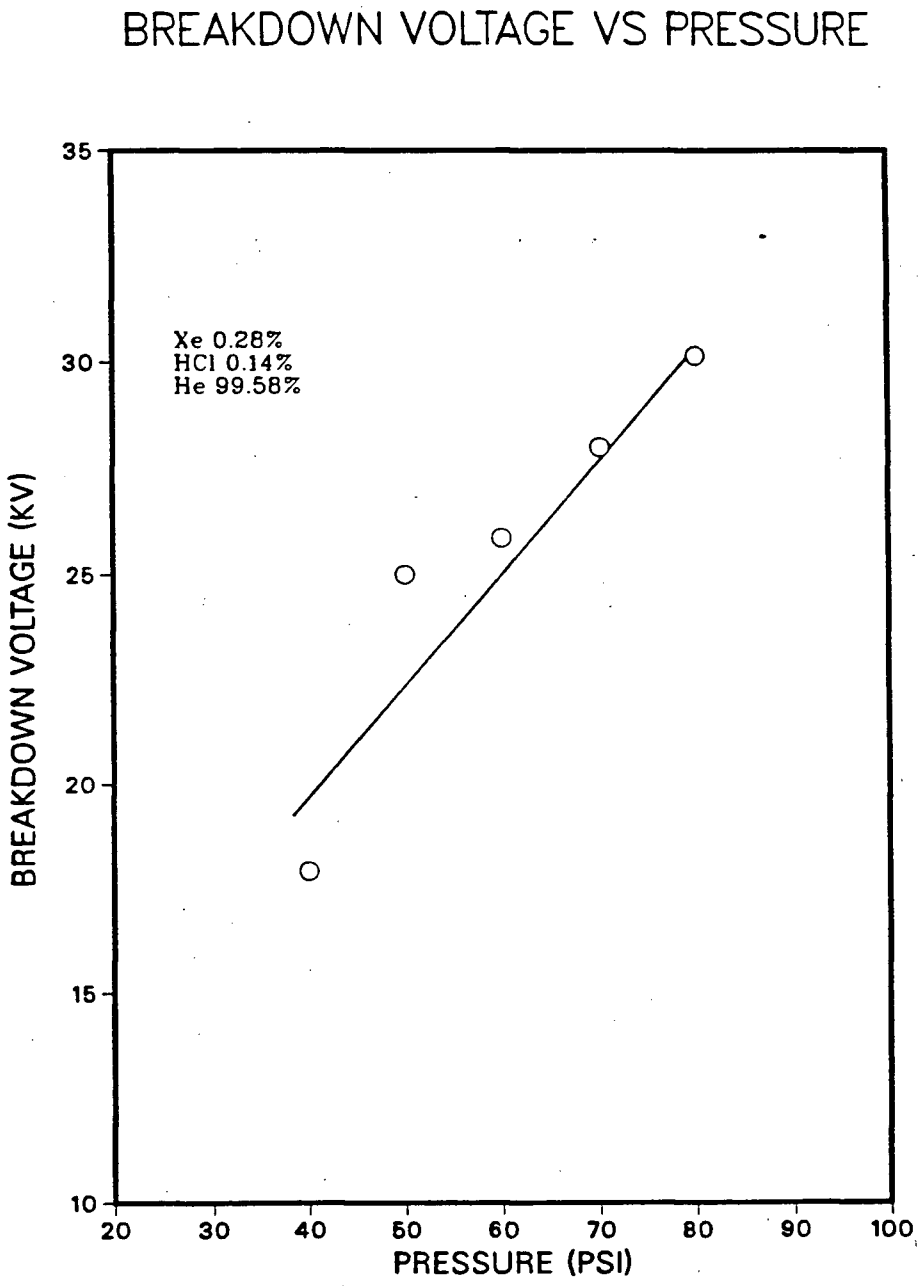

Figure 5.6: Breakdown voltage versus total pressure.

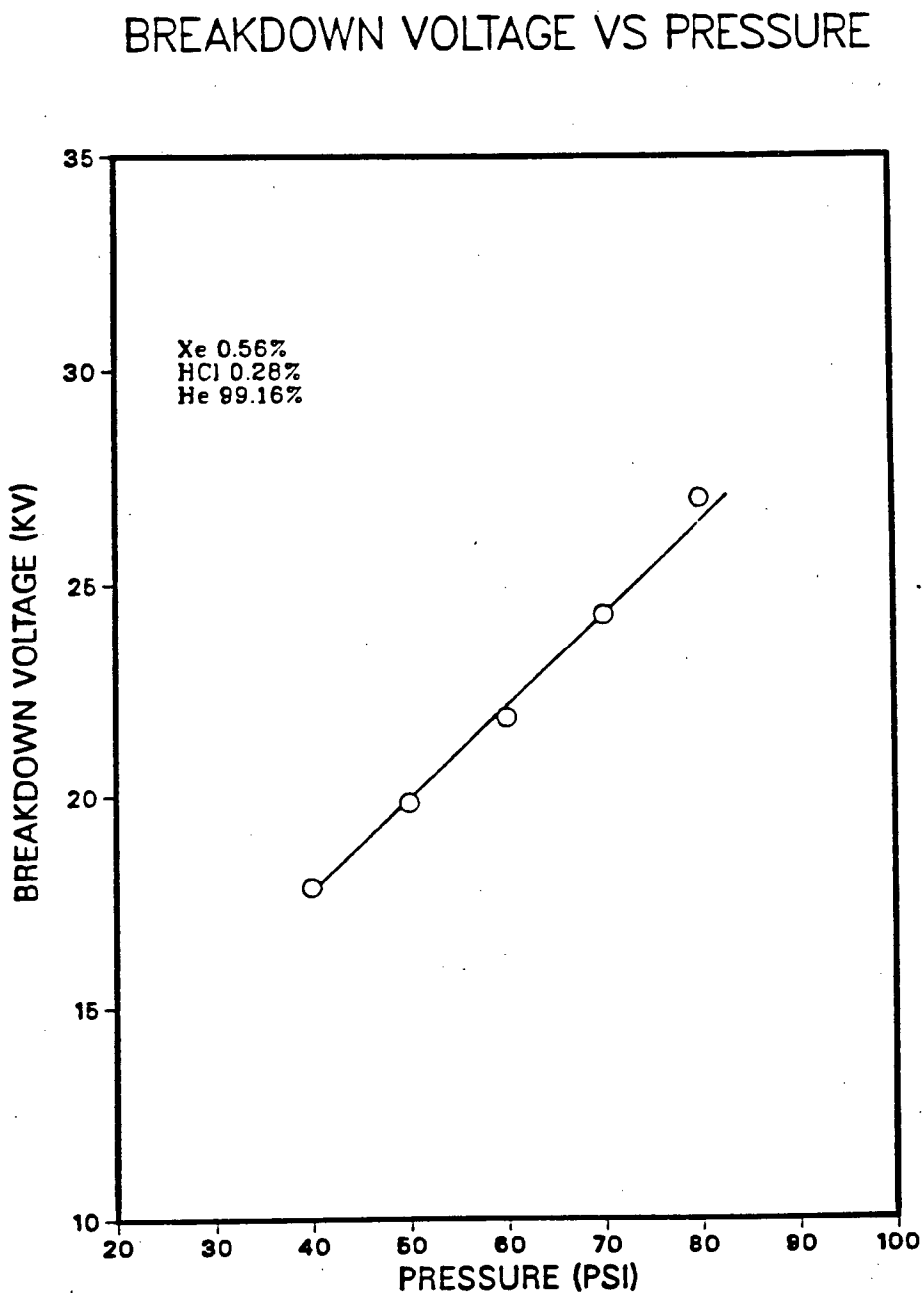

Figure 5.7: Breakdown voltage versus total pressure.

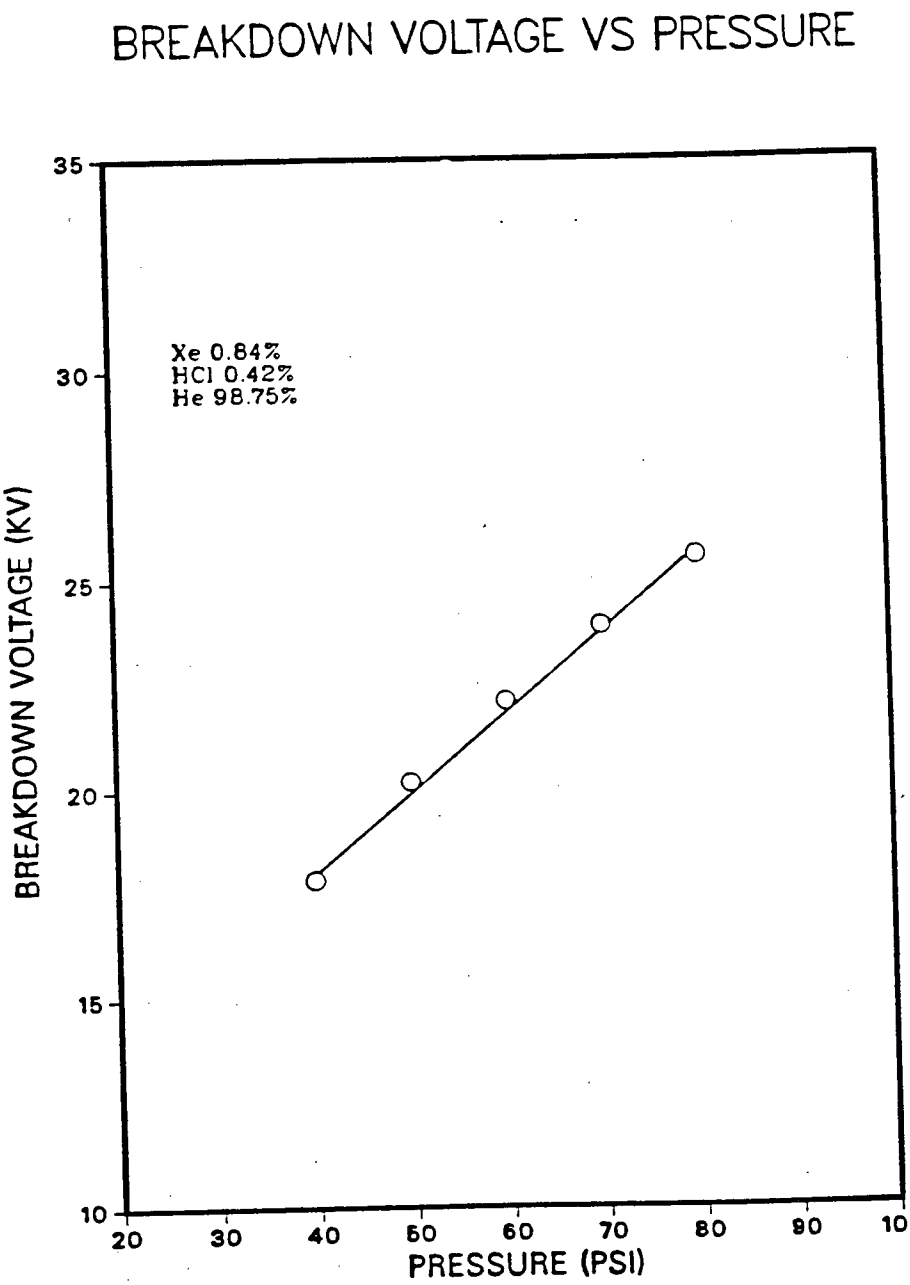

Figure 5.8: Breakdown voltage versus total pressure.

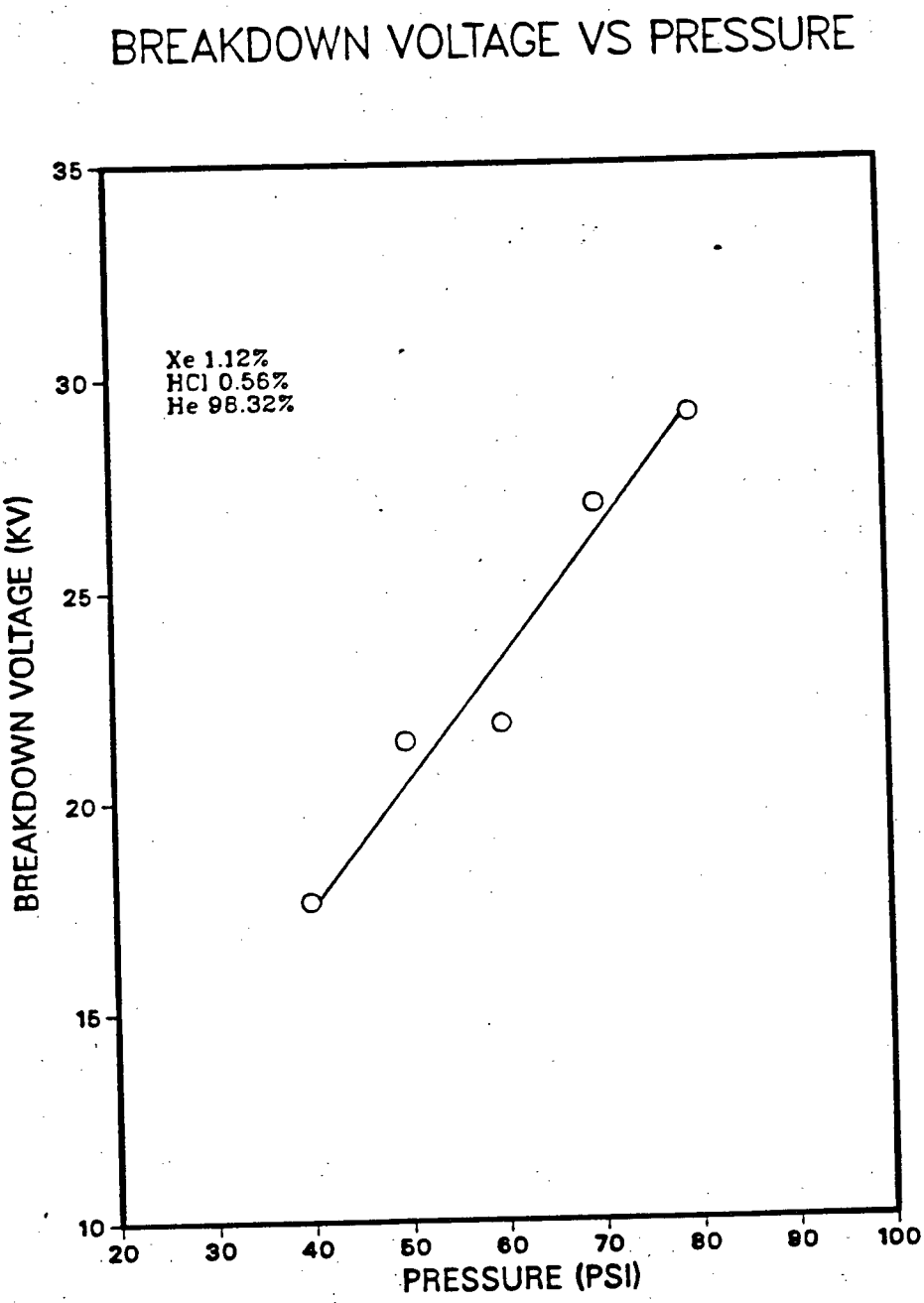

Figure 5.9: Breakdown voltage versus total pressure.

$V_d(t)$ is the drift velocity of the electrons.

Figures (5.10) to (5.12) display the temporal behaviour of the discharge impedance in pure He gas at variable pressures, where, after the voltage breakdown, the resistance of the falls rapidly as the current pulse rises. Then, the resistance reaches a plateau region and starts to rise again after the electron density starts to decay.
Figures (5.13) to (5.15) show the time histories of the discharge resistance in the optimum lasing gas composition. The oscillations of the resistance in the plateau regions are due to the noise in the current and voltage traces, and are not real, but products of the calculations. Therefore, it was decided to average the discharge resistance over the whole plateau region terminating at the end of the initial current pulse.

For the optimum operating conditions, the resistance was calculated to be 0.41 $\pm$0.08 Ω which is lower than the discharge impedance calculated for a critically damped RLC circuit (1.83 Ω).
We also performed the same calculations at quarter, half, and three quarters of the lasing gas concentrations; the results are plotted in figures (5.16) to (5.24). At a quarter of the lasing mixture concentration, the glow discharge is unstable, and is followed by arc formation; therefore, the resistance values were not used in any of the following analyses.

Since the halogen donor (HCl) plays an important role in discharge stability and electron attachment [54, 55] (which in turn affects the discharge resistance), we plotted the time average discharge resistance versus the HCl partial pressure in figure (5.25). The plot reveals that the discharge resistance is a decreasing function of the HCl partial pressure (or concentration). Such a result is contradictory to the result obtained by Ohwa et al. [3] in their computer simulation.

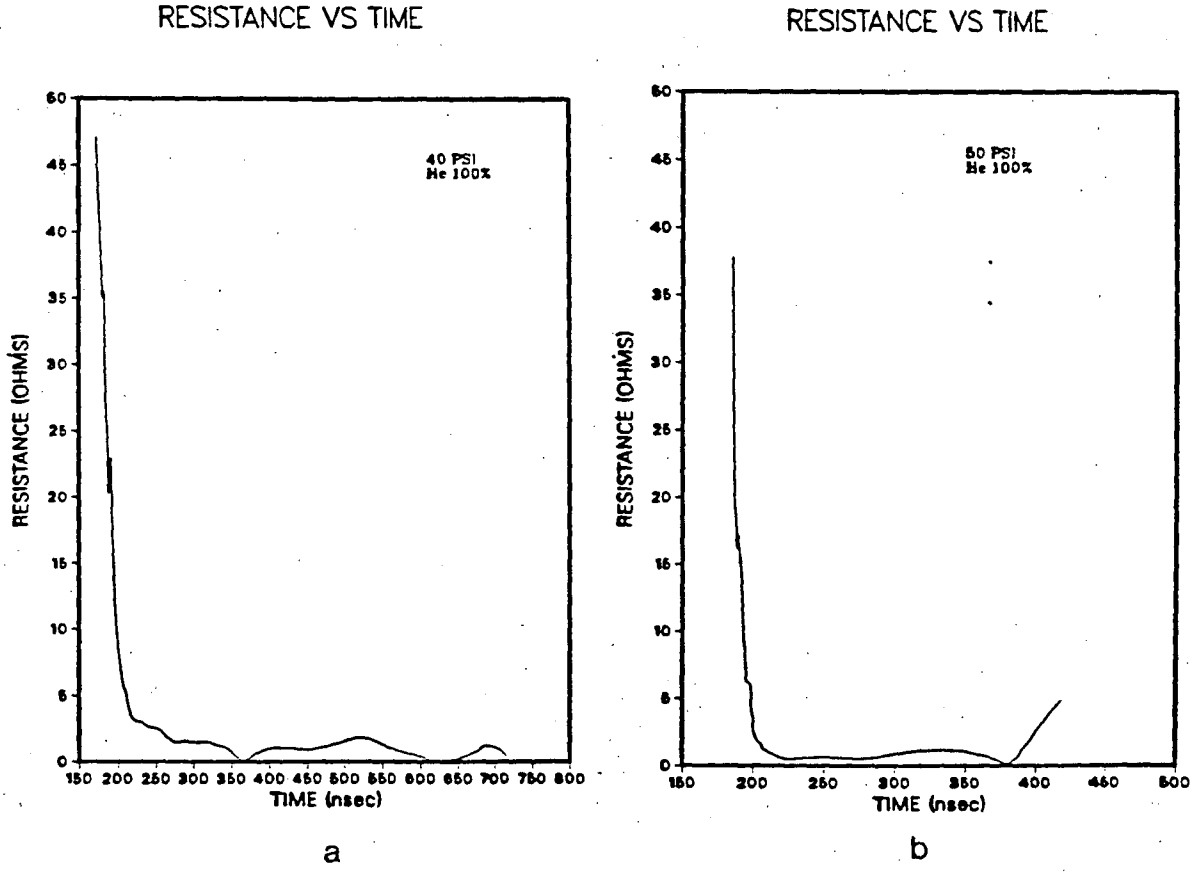

Figure 5.10: Discharge resistance as a function of time in He at (a) 40 Psi, 30 KV. (b) 50 Psi, 30 KV.

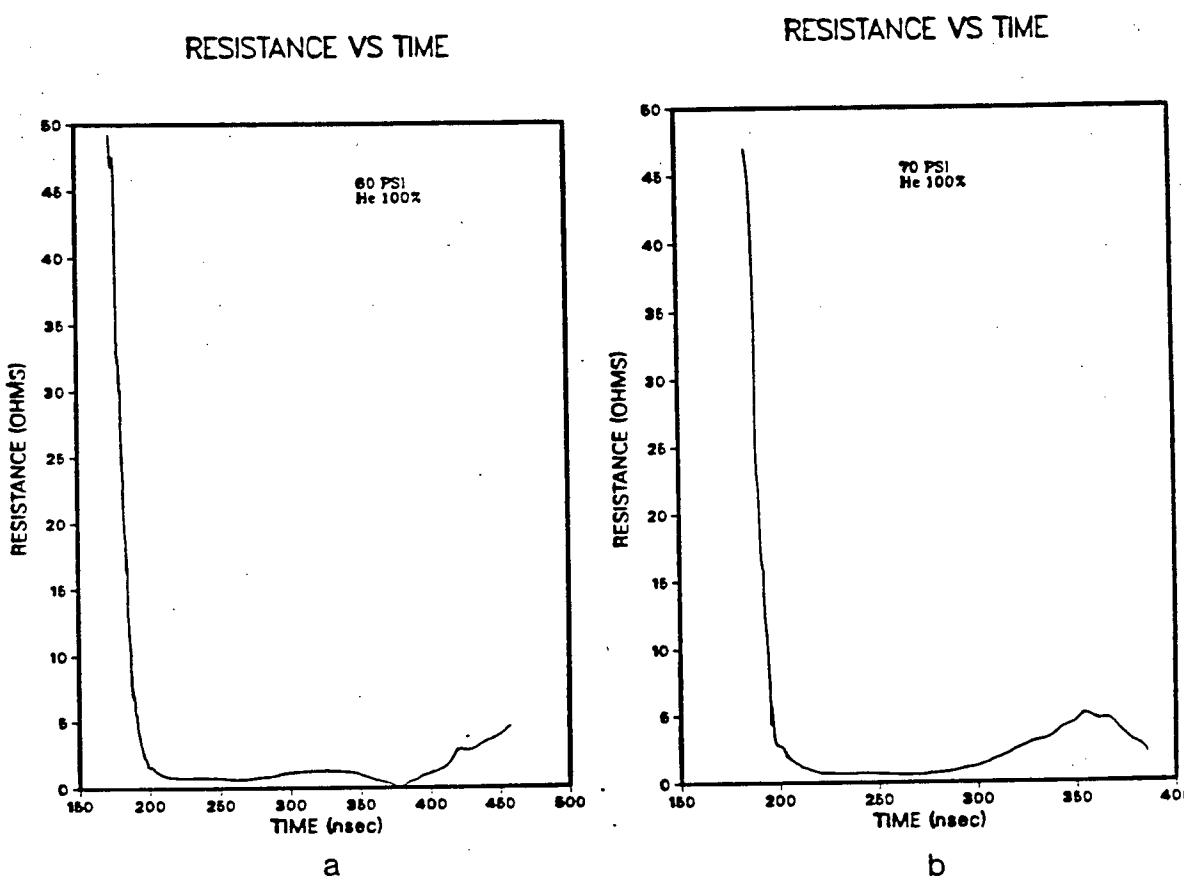

Figure 5.11: Discharge resistance as a function of time in He at (a) 60 Psi, 30 KV. (b) 70 Psi, 30 KV.

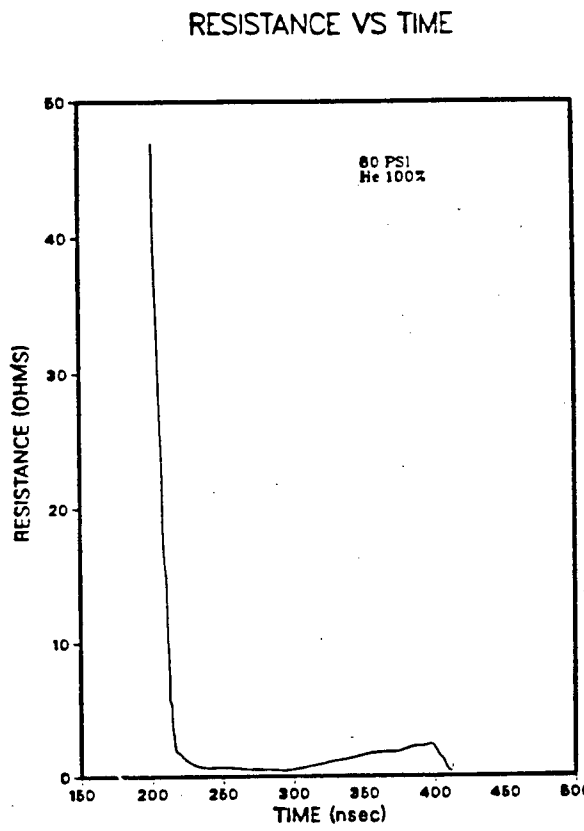

Figure 5.12: Discharge resistance as a function of time in 80 Psi He, 30 KV.

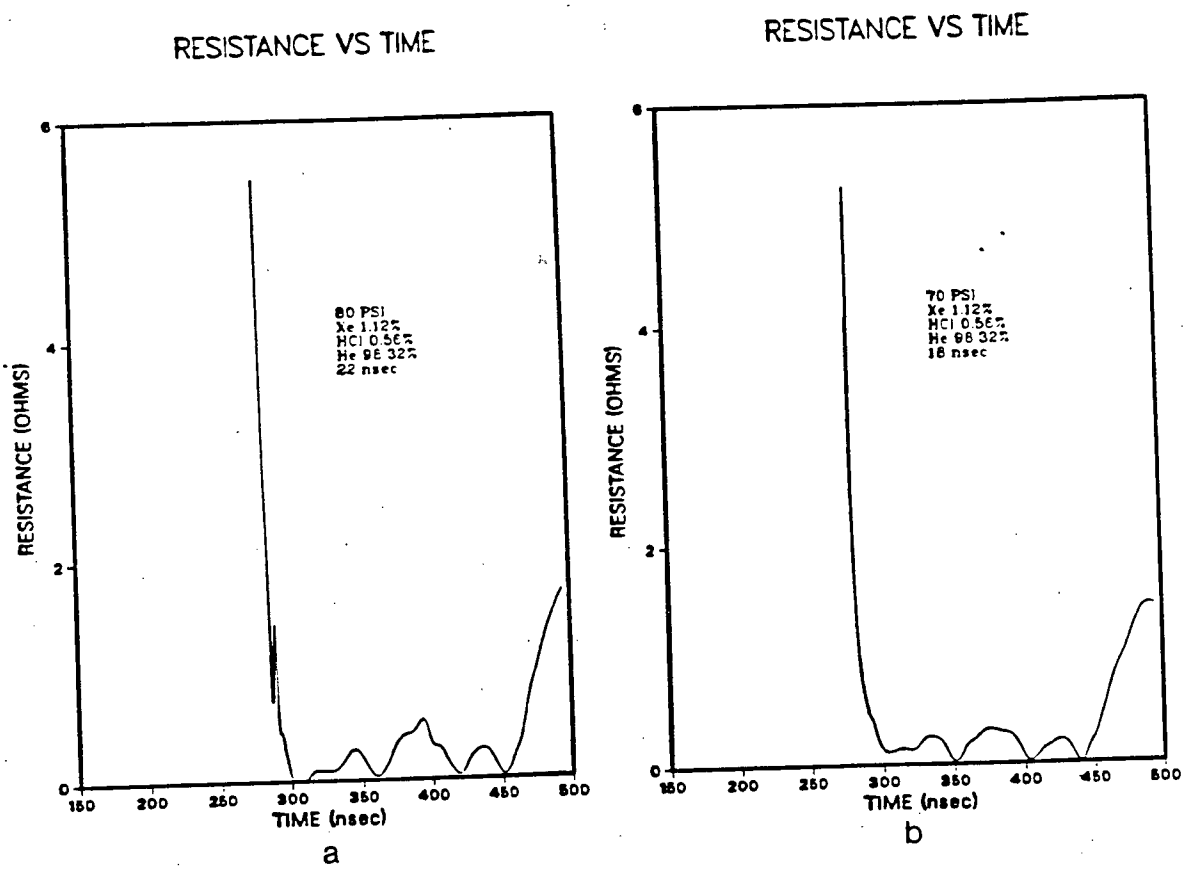

Figure 5.13: Discharge resistance at 1.12% Xe, 0.56% HCl, 98.32% He ((a) 80 Psi, (b) 70 Psi. The time above is after breakdown).

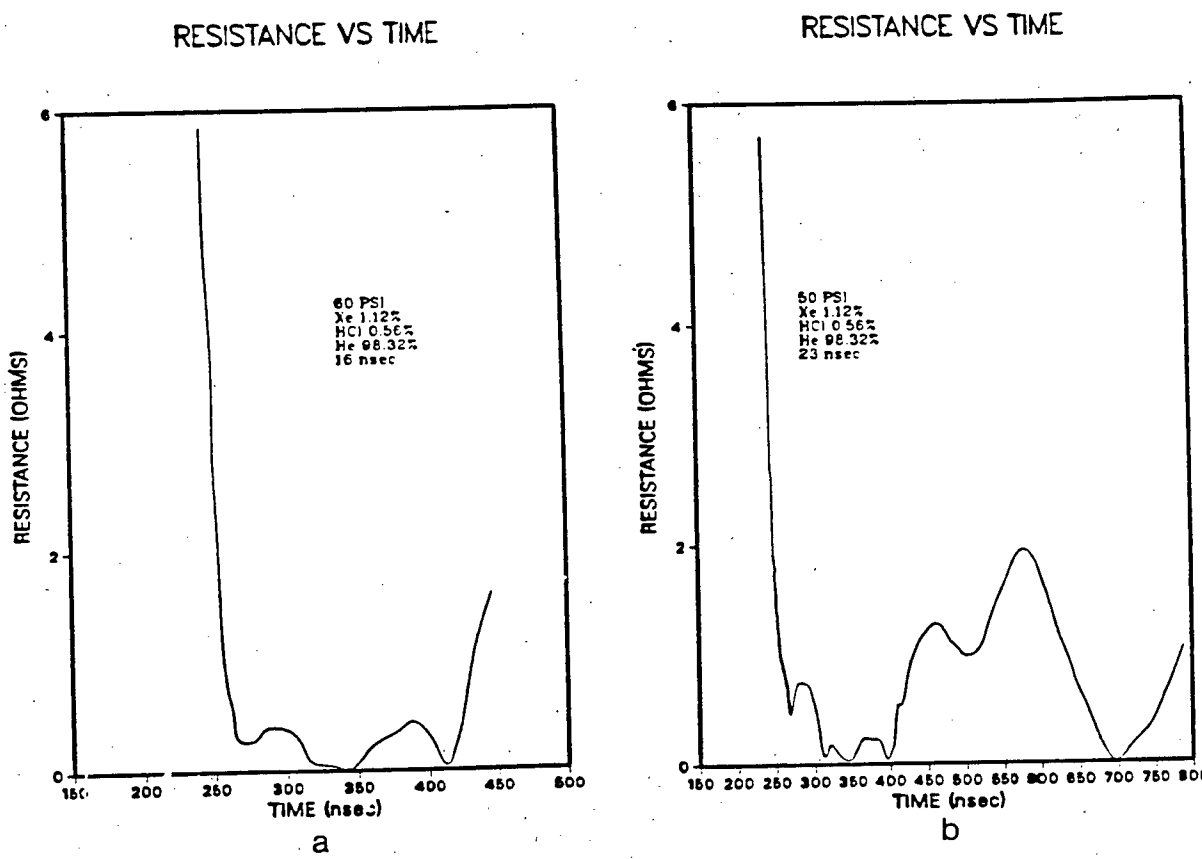

Figure 5.14: Discharge resistance at 1.12% Xe, 0.56% HCl, 98.32% He ((a) 60 Psi, (b) 50 Psi. The time above is after breakdown).

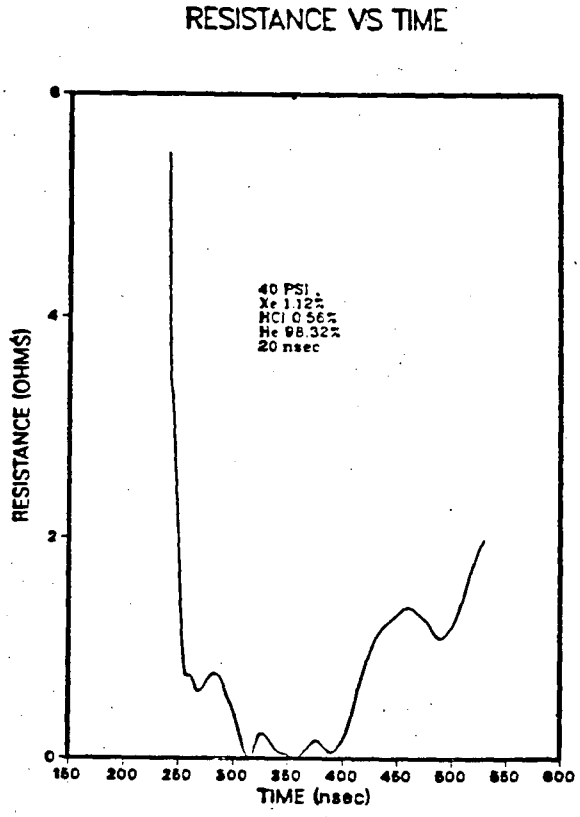

Figure 5.15: Discharge resistance at 1.12% Xe, 0.56% HCl, 98.32% He ((40 Psi. The time above is after breakdown).

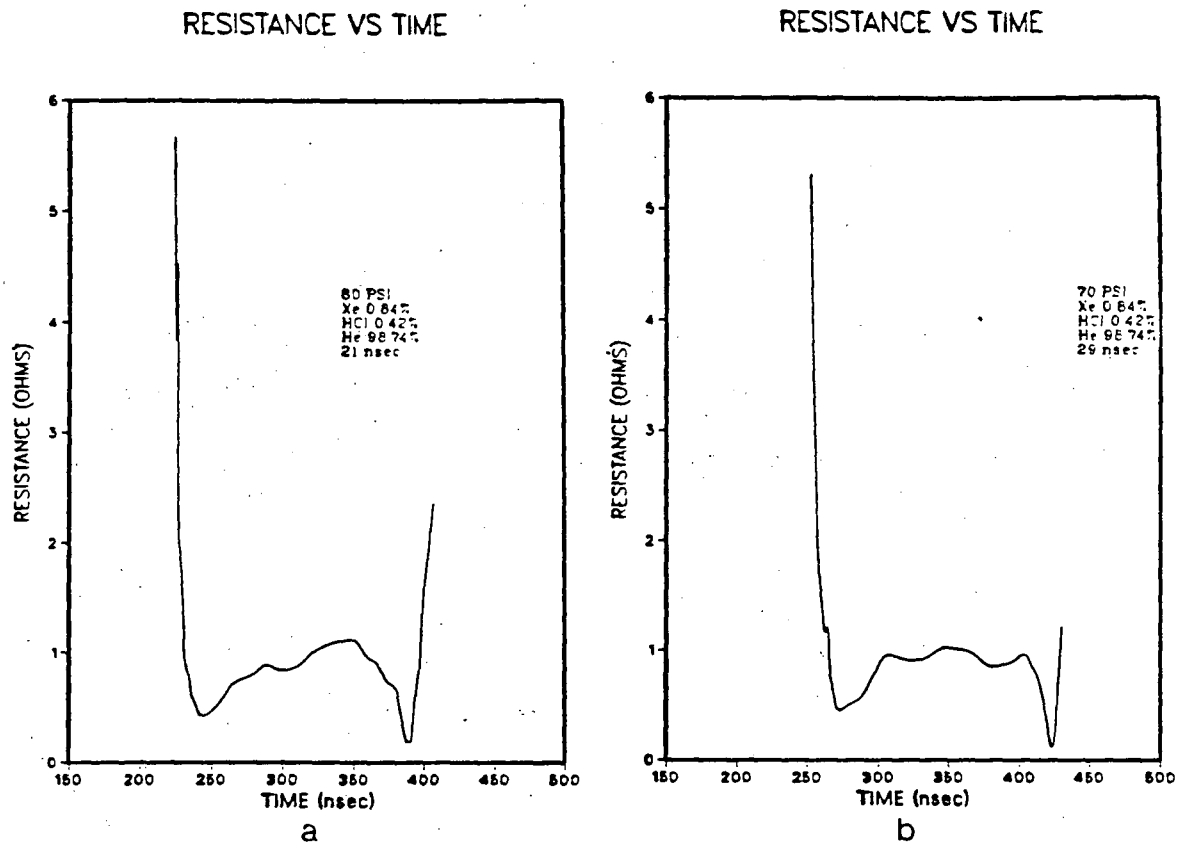

Figure 5.16: Discharge resistance at 0.84% Xe, 0.42% HCl, 98.74% He ((a) 80 Psi, (b) 70 Psi. The time above is after breakdown).

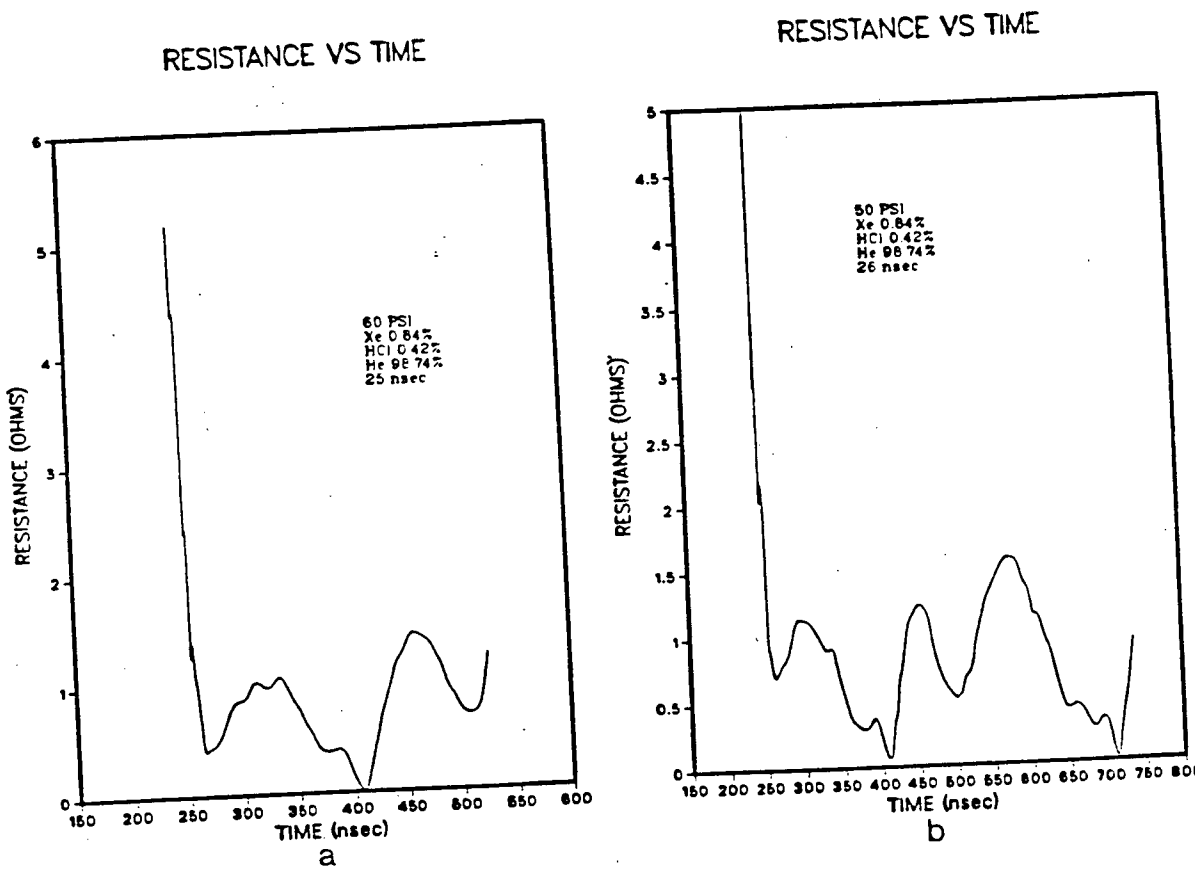

Figure 5.17: Discharge resistance at 0.84% Xe, 0.42% HCl, 98.74% He ((a) 60 Psi, (b) 50 Psi. The time above is after breakdown).

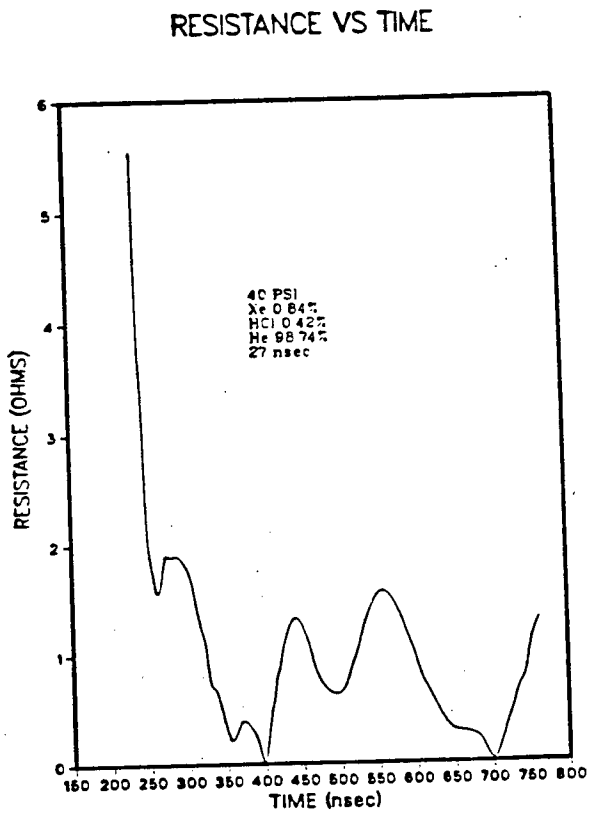

Figure 5.18: Discharge resistance at 0.84% Xe, 0.42% HCl, 98.74% He (40 Psi. The time above is after breakdown).

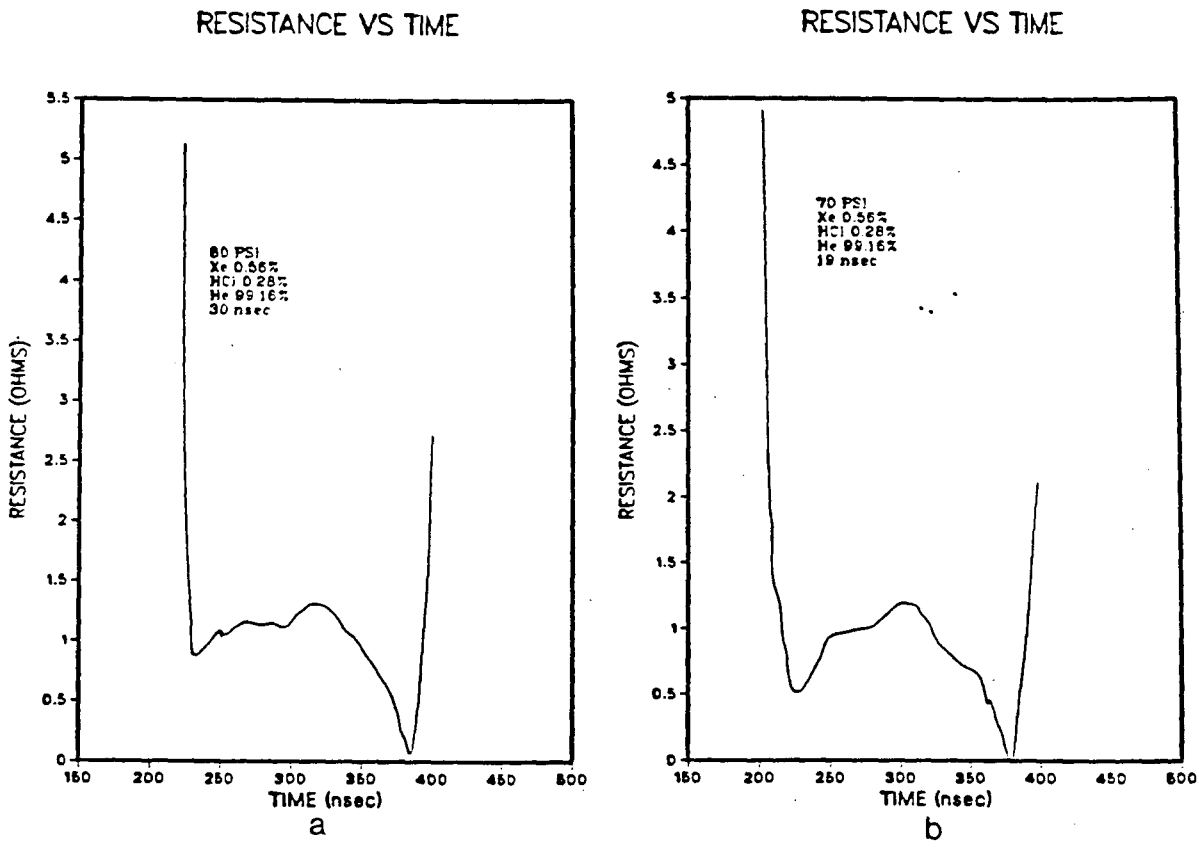

Figure 5.19: Discharge resistance at 0.56% Xe, 0.28% HCl, 99.16% He ((a) 80 Psi, (b) 70 Psi. The time above is after breakdown).

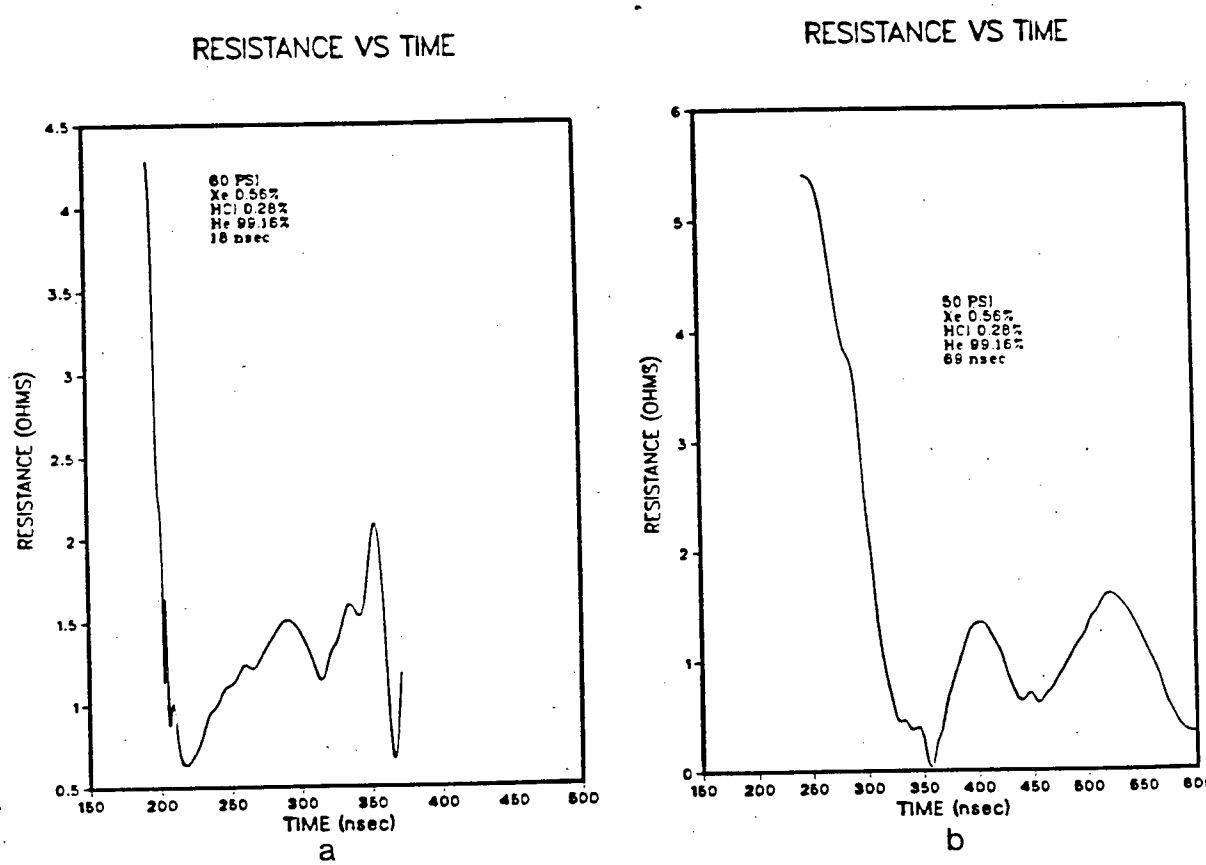

Figure 5.20: Discharge resistance at 0.56% Xe, 0.28% HCl, 98.16% He ((a) 60 Psi, (b) 50 Psi. The time above is after breakdown).

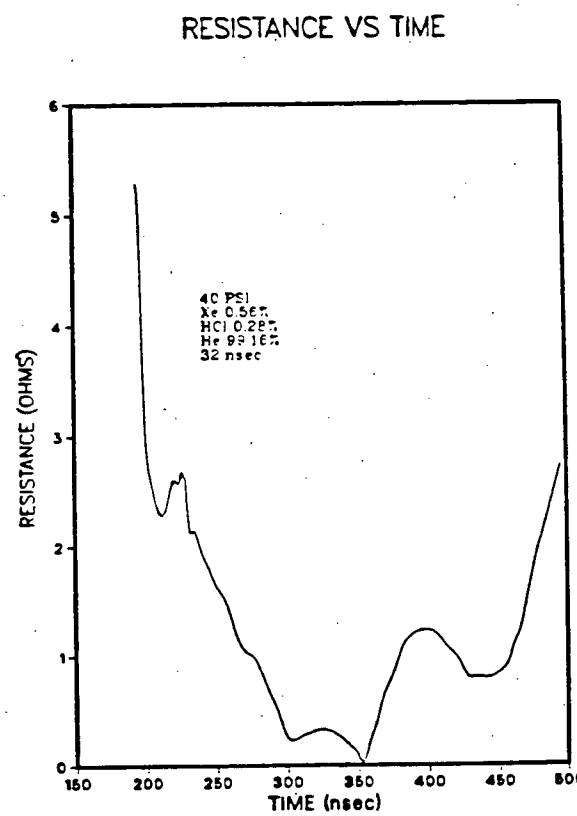

Figure 5.21: Discharge resistance at 0.56% Xe, 0.28% HCl, 99.16% He (40 Psi. The time above is after breakdown).

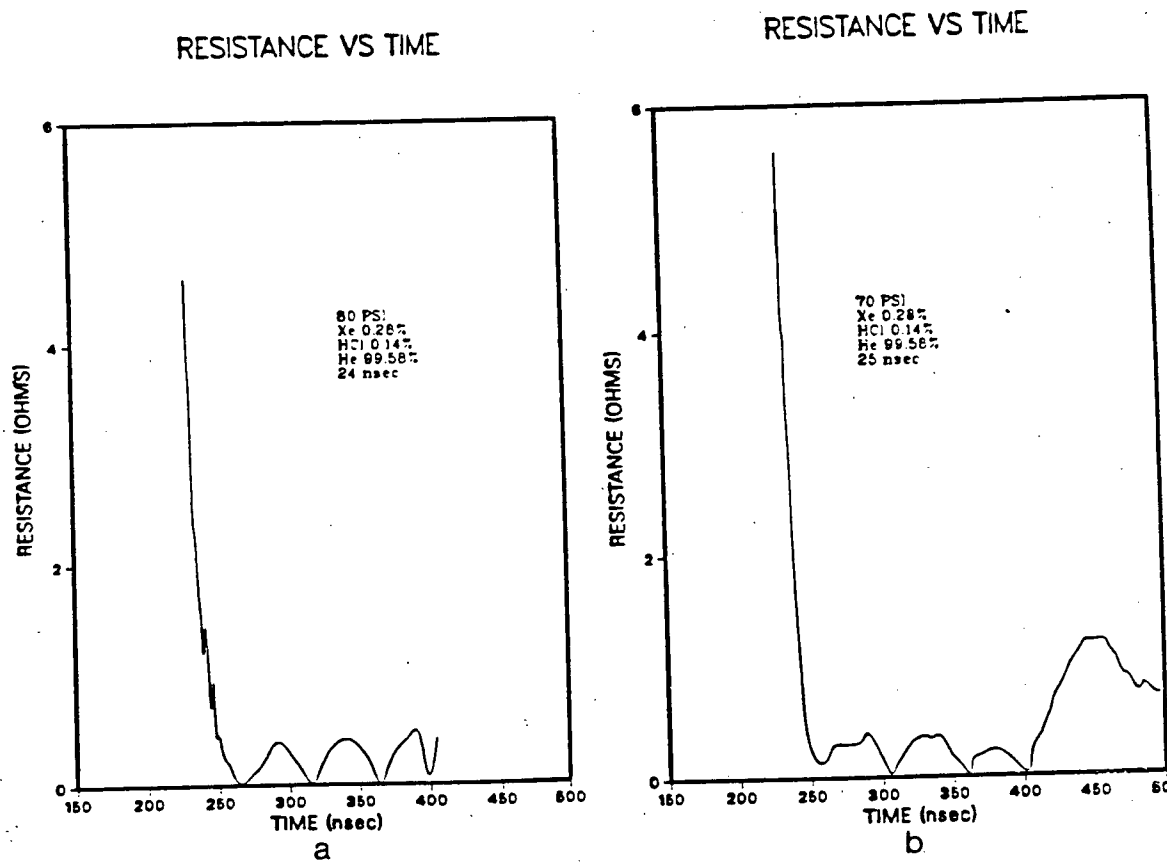

Figure 5.22: Discharge resistance at 0.28% Xe, 0.14% HCl, 99.58% He ((a) 80 Psi, (b) 70 Psi. The time above is after breakdown).

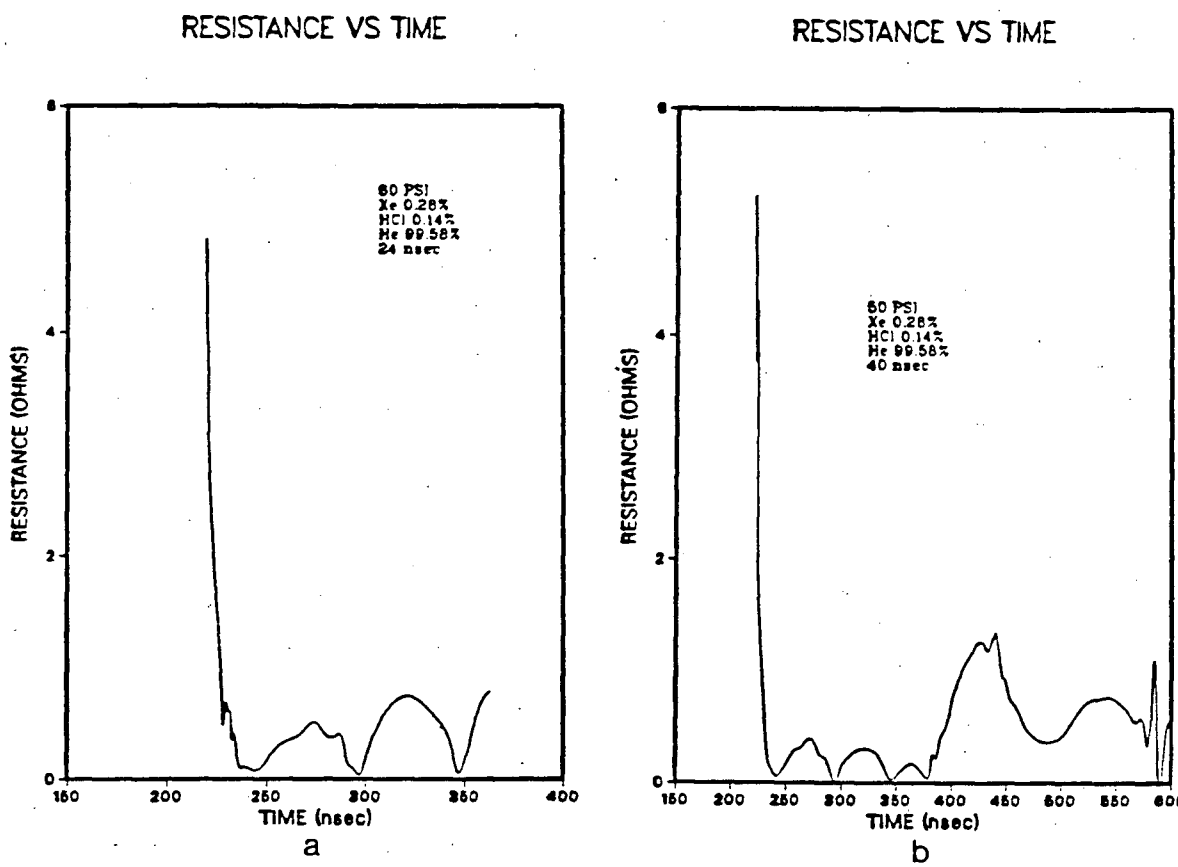

Figure 5.23: Discharge resistance at 0.28% Xe, 0.14% HCl, 99.58% He ((a) 60 Psi, (b) 50 Psi. The time above is after breakdown).

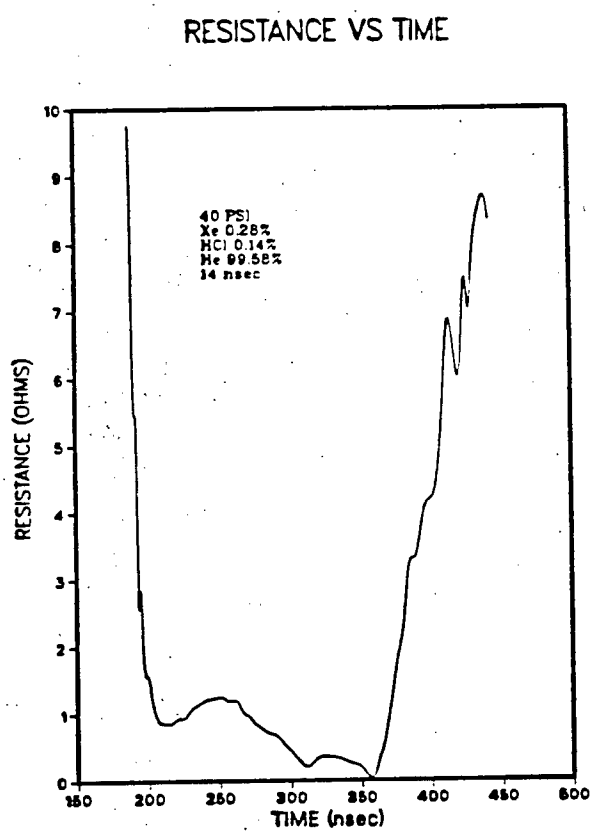

Figure 5.24: Discharge resistance at 0.28% Xe, 0.14% HCl, 99.58% He (40 Psi. The time above is after breakdown).

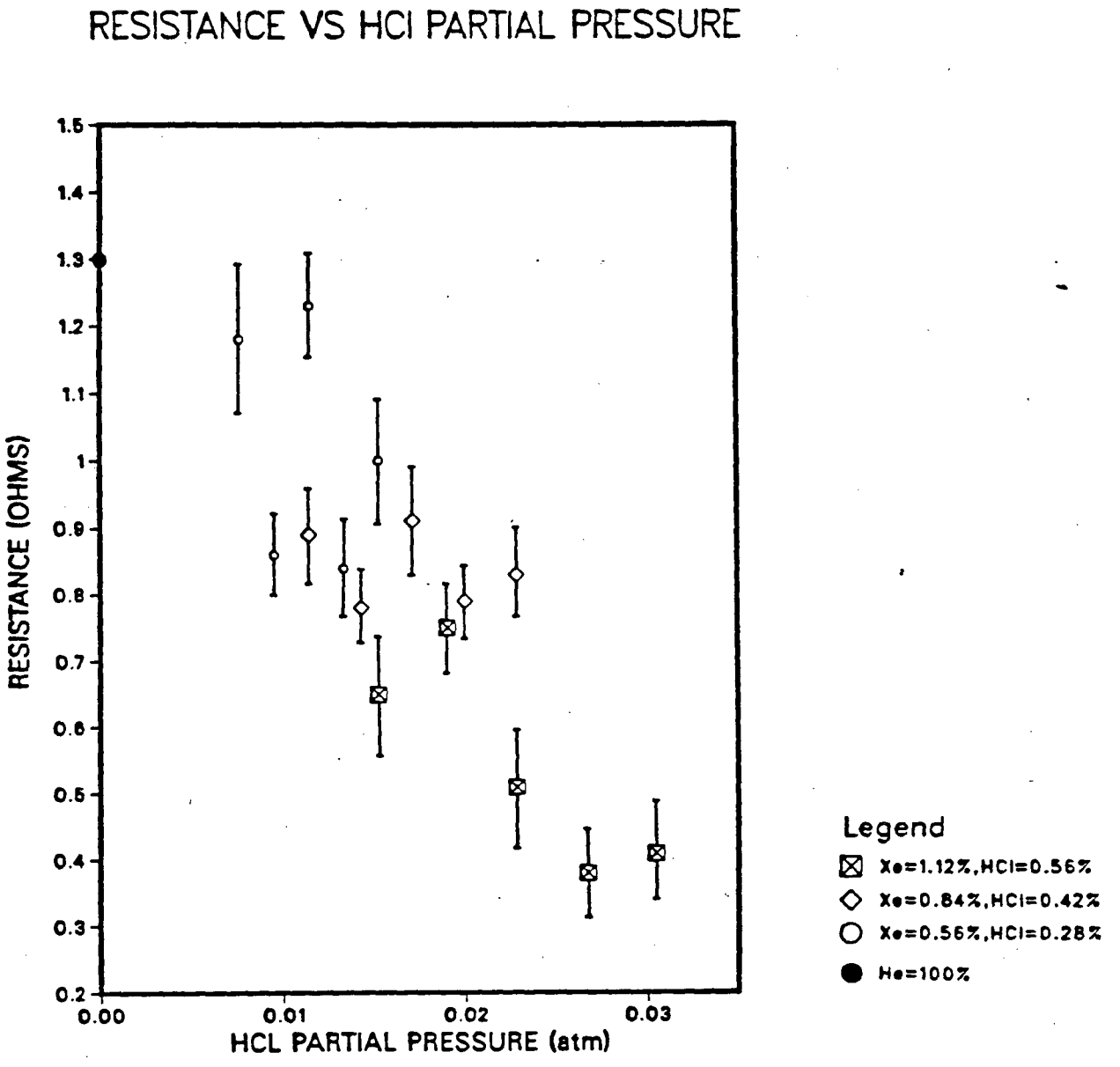

Figure 5.25: Average resistance as a function of HCl partial presure.

Chapter 6

Electron Density and Temperature

Two intrinsic properties, which determine the performance of an excimer laser, are the electron density and the temperature. In this chapter, a description of the measurements, techniques, and the analysis of both parameters will be presented.

6.1 Electron Density

The electron density in a $XeCl$ excimer laser discharge is an essential parameter determining the performance of the laser. The change in the temporal density profile gives an insight into the excitation and kinetic processes leading to the formation and quenching of the $XeCl^*$ excimer molecule. For example, electrons play an essential role in the quenching mechanism of the $XeCl^*$ excimer molecule through the reaction [3, 4]:

$$XeCl^* + e \longrightarrow Xe + Cl + e \tag{6.1}$$

which reduces the laser output energy.

The knowledge of the electron density enables the evaluation of discharge parameters, like the electron drift velocity. Therefore, in order to develop more efficient $XeCl$ lasers, it is important to compare computer simulations of the electron density with the experimental results.

Interferometric methods for determining the electron concentrations are satisfactory techniques. Laser interferometery, as a tool for discharge plasma diagnostic [56, 57], has many advantages over other methods. Langmuire probes, for example, must have physical

contact with the discharge plasma, thus disturbing it, whereas the use of microwave interferometry is restricted to electron densities below $10^{14} cm^{-3}$ [58] which is much less than the $XeCl$ laser electron density ($\approx 10^{15}\ cm^{-3}$). However, the use of infrared lasers comes in handy in the density range of 10^{14}-$10^{16}\ cm^{-3}$.

To date, only a few experimental studies of the temporal variation of the electron density in $XeCl^*$ discharge pumped lasers have been published, for example, by Ford et al. [1]. They used a Michelson type interferometer to measure the temporal evalution of the electron density. On the other hand, both Hollins and Hiramatsu [59, 60] used a spectroscopic technique, by measuring the Stark broadening of the H_β line.
Recently, De Anglies et al. [61] reported a direct measurement of the electron density temporal evolution using a holographic interferometry technique. Kimura et al. [62] employed a CO_2 quadrature interferometer to measure the electron density in an electron beam pumped $XeCl$ laser.

Several computer simulations and models were developed to describe and predict the kinetic mechanisms of the discharge pumped $XeCl$ lasers. All do not involve the prediction of the temporal behaviour of the discharge electron density and, thus, are considered to be incomplete. One comprehensive simulation code was developed by Johnson et al. [63] to predict the electron density temporal variation in an electron beam pumped $XeCl$ laser.

6.2 The Experimental Setup

In our study of the electron density, we have used the setup illustrated in figure (6.1). A brief description is given below.

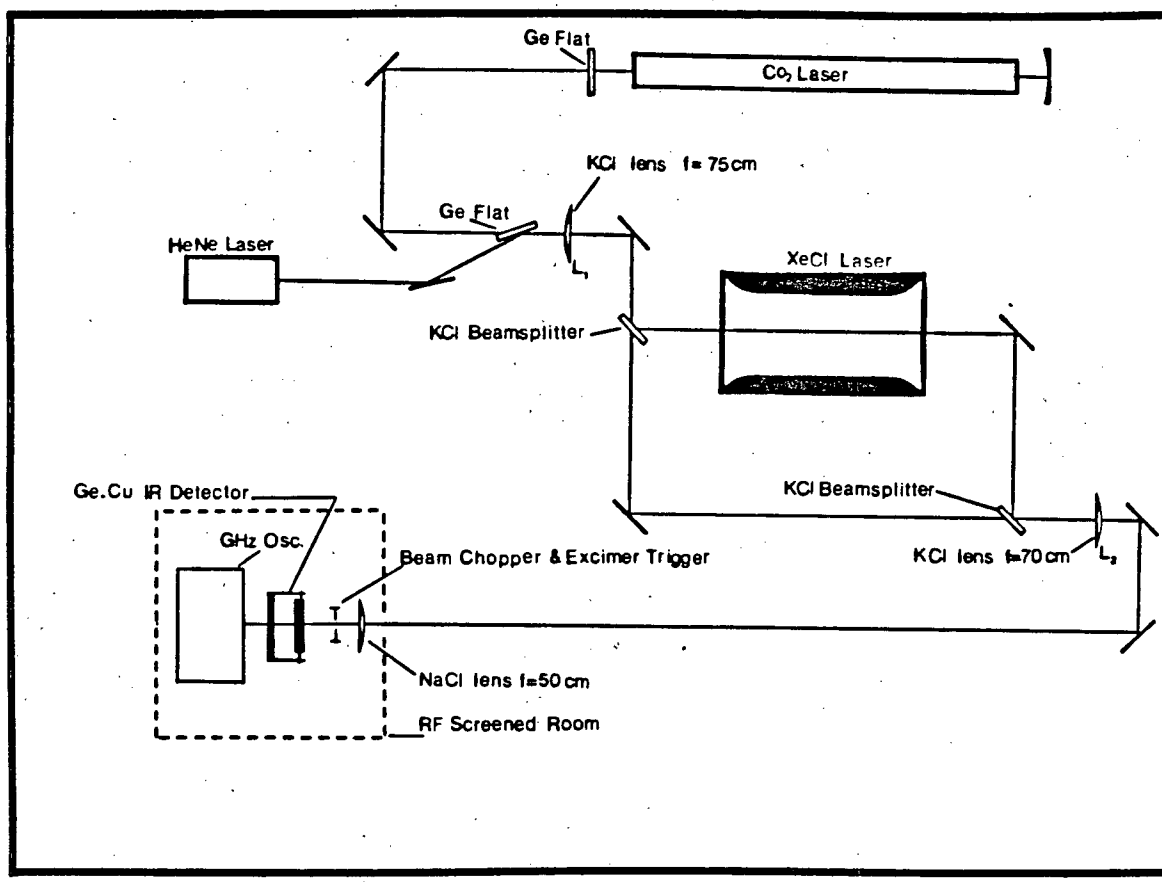

Figure 6.1: A CO_2 Mach-Zehnder intreferometer used for n_e study.

6.2.1 The CO_2 Laser

A cw CO_2 laser beam was used for probing the discharge plasma. The laser (CO_2) was operated at a current of 8 mA and a discharge voltage of 15 KV, with an estimated output power of two watts at a gas pressure of 13 *torr*. The resonator cavity consisted of a concave mirror of 5 *cm* radius of curvature on one end, and a *Ge* flat as an output etalon on the other end. The *Ge* flat was kept at a constant temperature of 28 $C°$, using a temperature controller; at this temperature, the laser wavelength was stable at 10.6 μm (P20) as measured by the CO_2 spectrum analyzer.

6.2.2 The $XeCl$ Excimer Laser

The description of the laser body was presented in chapter 1; however, the two quartz windows were removed and replaced by two 2.5 *inches* in radius, 0.5 *inch* thick $NaCl$ windows. The windows can withstand the maximum gas pressure of 80 Psi without breaking.

6.2.3 The $HeNe$ Laser

A $HeNe$ laser was used for optical alignment of the interferometer. The $HeNe$ beam was reflected off a *Ge* flat which was placed in the CO_2 beam at a Brewster angle of $\approx 76°$. The $HeNe$ beam was adjusted so that the reflected beam concided with the CO_2 beam. The interferometer could then be aligned with the use of the $HeNe$ beam to satisfactory accuracy.

6.2.4 The Infrared Detector

A *Santa Barbara Research* liquid *He* cooled *Cu* doped *Ge* photoconductive detector was employed to detect the interferance fringes during the rise and fall of n_e. The detector has a flat spectral response over the 2 μm to 30μm wavelength range with $\leq$ one nanosecond rise time. In preparation for measurements, the detector dewar was pumped to $\approx 10^{-5}$ *torr*, then filled with liquid nitrogen and left to cool for two hours; after that, the detector was emptied and refilled with liquid *He* at 4.2 $K°$. When in use, the detector was biased at -100 volts, and the interference signal was displayed on a 7104 *Tektronix GHz* oscilloscope with a fast (50 Ω) 7A19 plug in.

The detector could be operated for as much as six hours on a single liquid *He* fill.

6.2.5 Principle of Interferometry

Initially, we used a Michelson interferometer setup, since it was compact, simple, and provided twice the optical path than a Mach-Zehnder interferometer; thus, twice as many fringes should result. However, when the Michelson interferometer was used in conjunction with the CO_2 laser, the laser cavity could not be completely decoupled from the interferometer. This resulted in modulation of the laser output, because the radiation was fed back by the interferometer mirrors to the CO_2 laser cavity.

Figure (6.2a) shows an example of the density oscillogram taken in 60 *Psi* of pure *He* at a charging voltage of 20 KV; it is clear that the real interference signal occurs in the first 100 *nsec*, and that the rest of the oscillogram signal is a result of the CO_2 laser intensity modulation by phase variation in the portion of the output radiation reflected back into the optical cavity. Therefore, it was decided to replace the Michelson interferometer by a Mach-Zehnder interferometer.

The Mach-Zehnder interferometer consists of two standard front surface plane mirrors and two 50:50 KCl beam splitters coated on one surface with antireflective coating. In order to minimize the refraction losses due to the excimer discharge plasma, two lenses situated outside the interferometer were employed. The CO_2 beam passed through a KCl plano-convex lens L_1 ($f = 75cm$), and was divided into two beams by the first beam splitter: L_1 focusses one beam at the centre of the excimer discharge, while the other beam was used as an external reference signal. The two beams are then combined on the second beam splitter. The combined beams were then passed through another KCl ($f = 70cm$) plano-convex lens L_2.

Introducing the collimating system improved the quality of the interference fringes. Figure (6.2b) shows an oscillogram of the interference pattern taken in 80 Psi of He; this photograph was taken without the the use of the collimating system, whereas figure (6.2c) shows the same interference signal taken under the same conditions, but with the use of the collimating lenses L_1 and L_2 in place. It is clear that the introduction of the lenses resulted in higher signal amplitudes and clearer interference fringes, since the refraction of the probe beam by the discharge plasma was minimized.

The technique for adjusting the interferometer is simple: The four plates of the Mach-Zehnder interferometer were, with the aid of the $HeNe$ laser beam, adjusted approximately parallel to each other. The $HeNe$ beam was superimposed on the CO_2 beam. Once the $HeNe$ beams were correctly combined at the second beam splitter, temporal interference fringes appeared in the far field. The CO_2 beam was turned on and temporal fringes due to the vibration of the optical bench were detected by the Cu doped Ge detector. The combining beam splitter was then adjusted for maximum temporal fringe visibility.

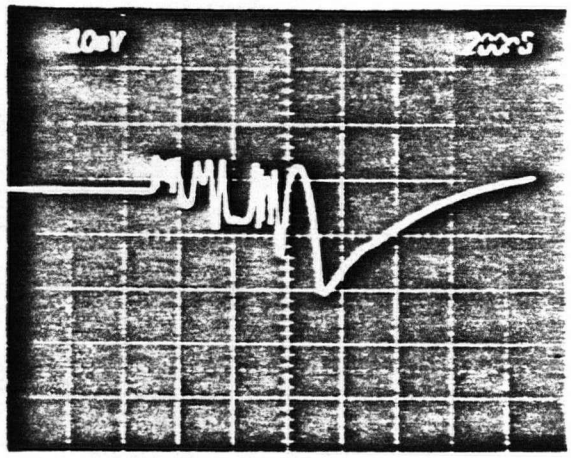

a

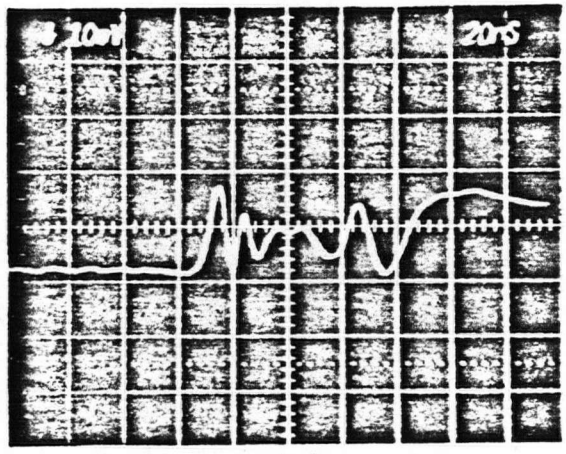

b

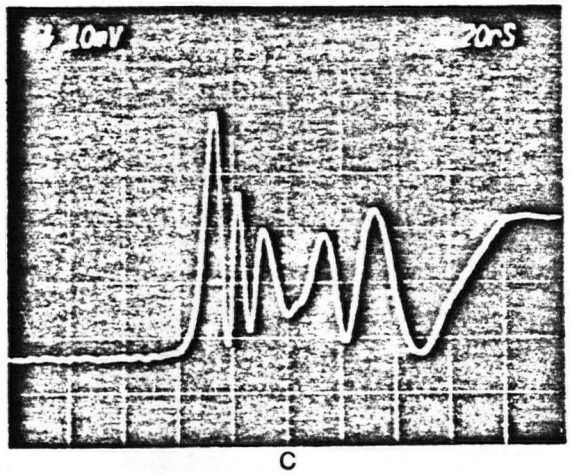

c

Figure 6.2: Density oscillograms in He (a) 60 Psi, 20 KV, using a Michelson interferometer. (b) 80 Psi, 30 KV, using a Mach_Zehnder interferometer without the collimating system. (c) same as (b) except for the collimating system.

6.2.6 Refractivity and the Electron Density

The electron density (n_e) of the plasma can be determined by measuring its refractive index. Consider a plasma of refractive index μ_p. For electromagnetic waves with frequency ω, where ω is much greater than the plasma frequency ω_p and different from any resonance frequencies of the heavy particles, the plasma refractivity is given by

$$\mu_p = \mu_e + \sum_i (\mu_i - 1) \tag{6.2}$$

where μ_e is the contribution due to free electrons and μ_i is the contribution due to other constituents such as atoms, molecules, and ions. But the free electrons' contribution to the refractivity dominates because the laser frequency does not coincide with the ground state transitions frequencies of Xe, He, H, HCl, and Cl; hence, electronic transitions of atoms do not contribute to the refractivity [1, 61]. Refractivity due to the ions is small, because their masses are much heavier than those of the electrons.

Hence, proceeding directly from the formulation of electromagnetic wave propagation in a uniform plasma, we have the refractive index of the plasma:

$$\mu_p = \sqrt{1 - \frac{\omega_p^2}{\omega^2}} \tag{6.3}$$

And for radiation frequency much higher than the plasma frequency, the above equation can be approximated to:

$$\mu_p = (1 - \frac{\omega_p^2}{2\omega^2}) \tag{6.4}$$

where $\omega_p^2 = \frac{4\pi n_e e^2}{m_e}$ in C.G.S. units.

The order of interference fringe, m, produced by the plasma in the Mach-Zehnder interferometer is given by

$$m = (\mu_p - 1)\frac{l}{\lambda} \tag{6.5}$$

where l is the length of the plasma discharge = 35 cm,

and λ is the probing wavelength of the CO_2 laser =10.6 μm.

Equations (6.4) and (6.5) give the relation between the electron density and the order of interference fringes, m, i.e.

$$m = (4.48 \times 10^{-14})l\lambda n_e \tag{6.6}$$

The above equation shows that the order of the interference fringes is proportional to the wavelength. Rearranging equation (6.6) gives

$$n_e(cm^{-3}) = m(6.02 \times 10^{14}) \tag{6.7}$$

From equation (6.7), an increase or decrease of the electron density in time is followed by the appearance of a new interference fringe whenever the phase changes by 2π. Therefore, the measurement of the interference fringe shifts give an accurate value of the plasma electron density, where one fringe shift corresponds to a change in electron density of 6.02×10^{14} cm^{-3}. In the interferograms, it was easy to measure the number of fringes up to half a fringe.

6.2.7 Experimental Results

Before proceeding with the experiment, the accuracy of the reproducibility of the interferograms was first investigated in pure He gas inside the excimer discharge. Figure (6.3) shows the result of six interference oscillograms taken in pure He at a filling pressure of 80 Psi and at a charging voltage of 30 KV; the corresponding densities of such ocsillograms

were plotted in figure (6.4). As can be seen from the figure, the reproducibility of the six separate experiments was excellent, and the only discrepancies between the runs were in the time axis, which is due to the choice of the beginning of the fringe pattern. The oscillograms also show the attenuation of the fringe amplitudes, as the electron density reaches its maximum value; this is a result of refraction of the probe radiation by the discharge plasma, and it is not due to the decreasing response of the detector to the more rapid change in the plasma density. When no interference fringes are produced (i.e. by blocking the reference arm of the interferometer), the CO_2 beam showed (figure (6.5)) the same attenuated envelope.

The electron density measurements in the discharge $XeCl$ were carried out over a wide range of the lasing gas concentration and total pressure. Figures (6.6) show six interferograms taken at the optimum lasing gas mix, charging voltage, and pressure. All interferograms show excellent reproducibility. The turnover (place on the oscillogram where the density reaches its maximum value) of each oscillogram was basically identified as a sudden reversal in the intensity of the interference fringes, and where the number of the full fringes on either side of the turn over point is the same.

The corresponding density of each oscillogram was plotted on figure (6.7). The electron density reaches a maximum value of 4.01×10^{15} cm^{-3} in about 37 $nsec$, corresponding to the peak of the current trace. After reaching the maximum density, where the rate of production of electron equals the rate of losses, the density decreases slowly reaching the zero level after 110 $nsec$ from the start of the current pulse.

Similar experiments were performed at the same lasing gas mix, but at various filling pressures; their electron densities are plotted in figures (6.8) to (6.9). Each single figure contains, on the average, more than five experiments.

To study the change of the electron density as a function of the concentration, several

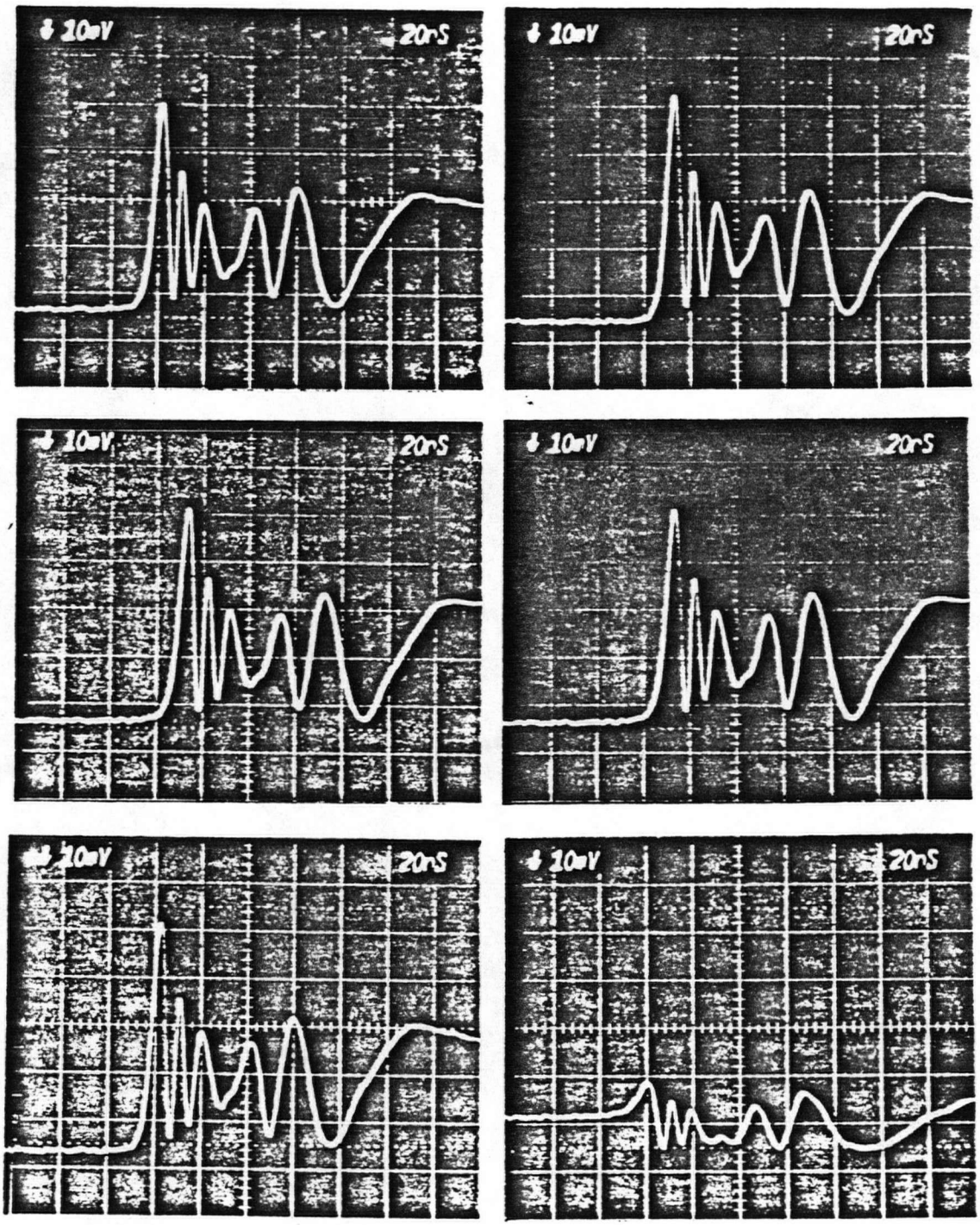

Figure 6.3: Six oscillograms taken in pure He at 80 Psi, 30 Kv.

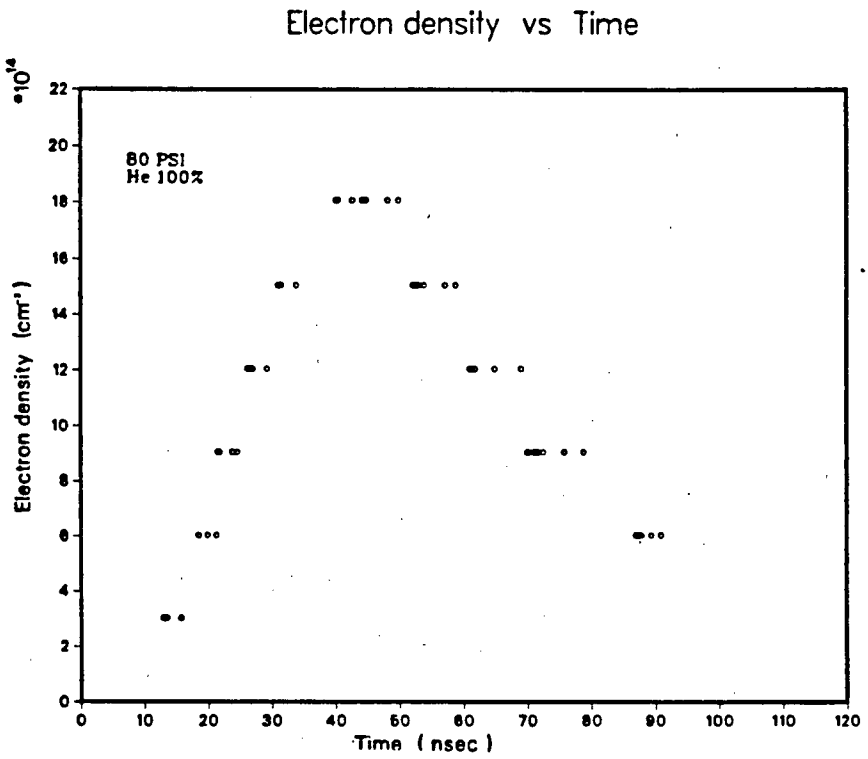

Figure 6.4: Electron density plotted from figure (6.3).

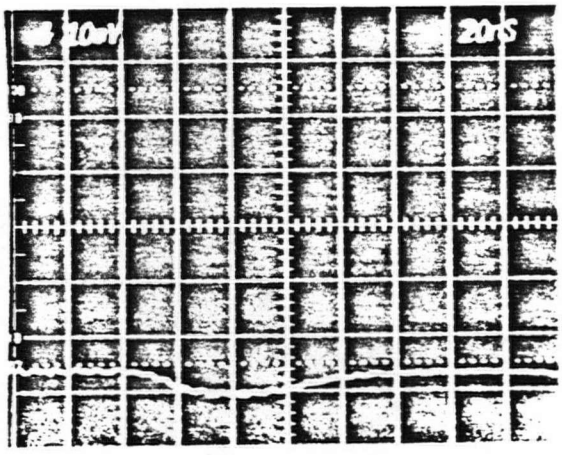

Figure 6.5: Attenuated CO_2 beam with the reference arm of the interferometer blocked.

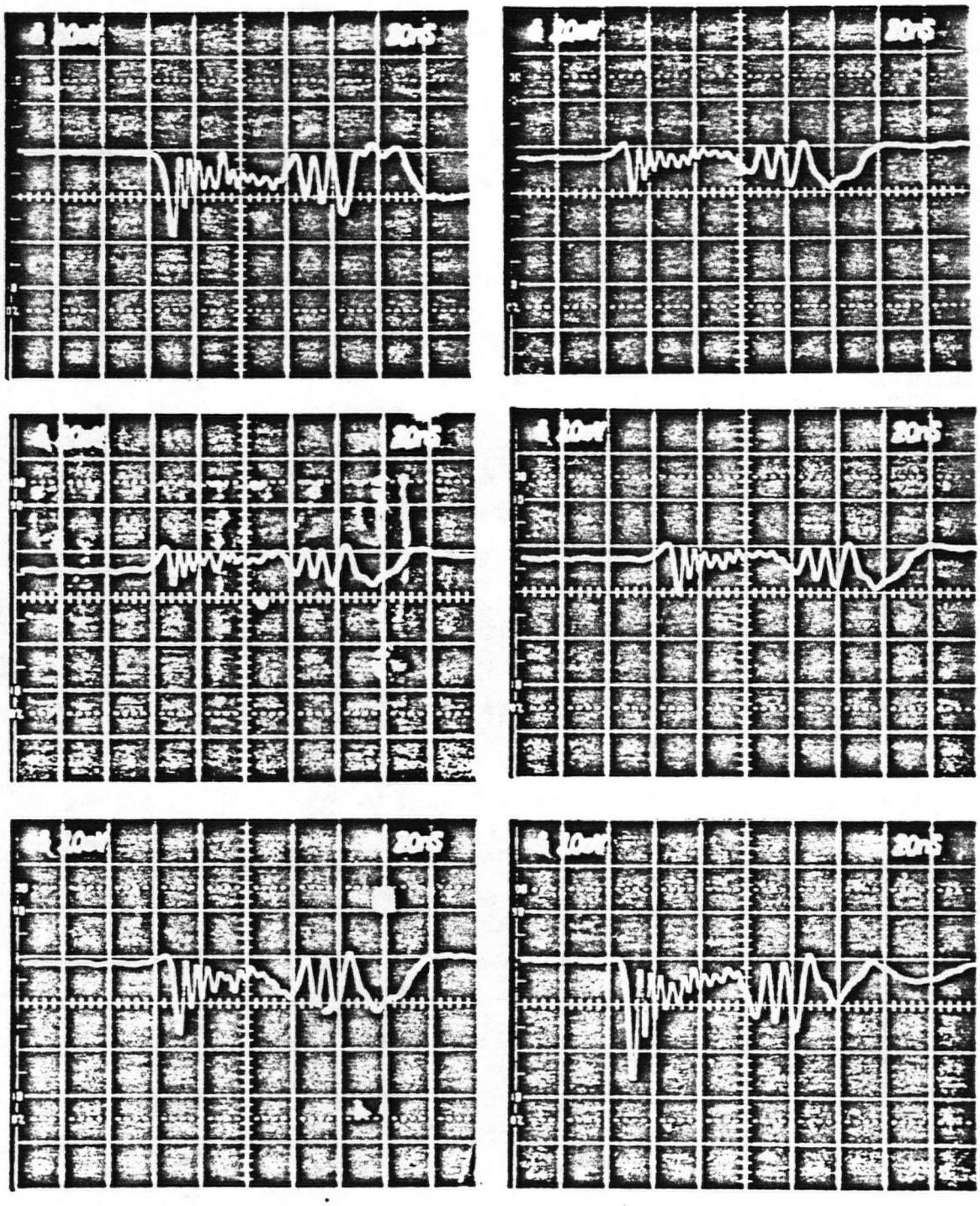

Figure 6.6: Density oscillograms at the full gas mix (1.12%(Xe), 0.56%(HCl), 98.32%(He), 80 Psi, and 30 KV).

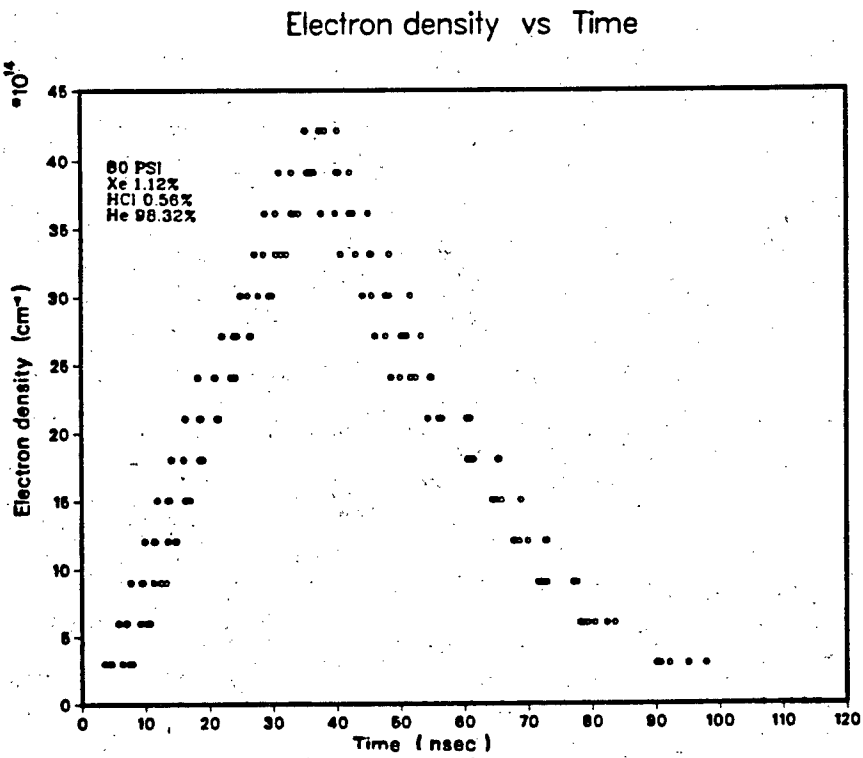

Figure 6.7: Graph of the electron density as a function of time for the same conditions as in figure (6.6).

experiments were performed in quarter, half, and three quarters of the optimum Xe and HCl concentrations. The corresponding electron densities were plotted in figures (6.10) to (6.19). Only those results where discharge arcing was obvious were rejected.

When measuring the electron densities for various HCl concentrations, a noticeable difference in the electron densities was observed between high and low HCl concentrations. At low HCl concentrations, the electron density increases to a high value, probably due to insufficient dissociative attachment to the HCl molecules; at higher HCl concentrations, the electron density decreases as a result of higher dissociative attachment to the HCl molecules. A plot (figure (6.20)) of a normalized n_e to the helium density n_{He} versus HCl partial pressure shows this behaviour.

On the basis of the interpretation discussed above and of references [3, 62, 63, 64], we suggest that the reaction that might be responsible for this decrease in the electron density is:

$$HCl(v = 1) + e \longrightarrow H + Cl^- \tag{6.8}$$

The rate of this reaction increases as a result of increasing the electronic excitation of the HCl molecule from the ground state ($v = 0$) to the first excited state ($v = 1$), while excitations to higher vibrational levels than ($v = 1$) contribute much less to this reaction. The rate of the recombination of Cl^- and H is much slower than the rate of dissociation of HCl molecules [64]. Therefore, on the time scale of the laser pulse, the HCl gas will be used up, resulting in a decrease of the electron density. The dissociative attachment of HCl may also result in increasing discharge instability [61].

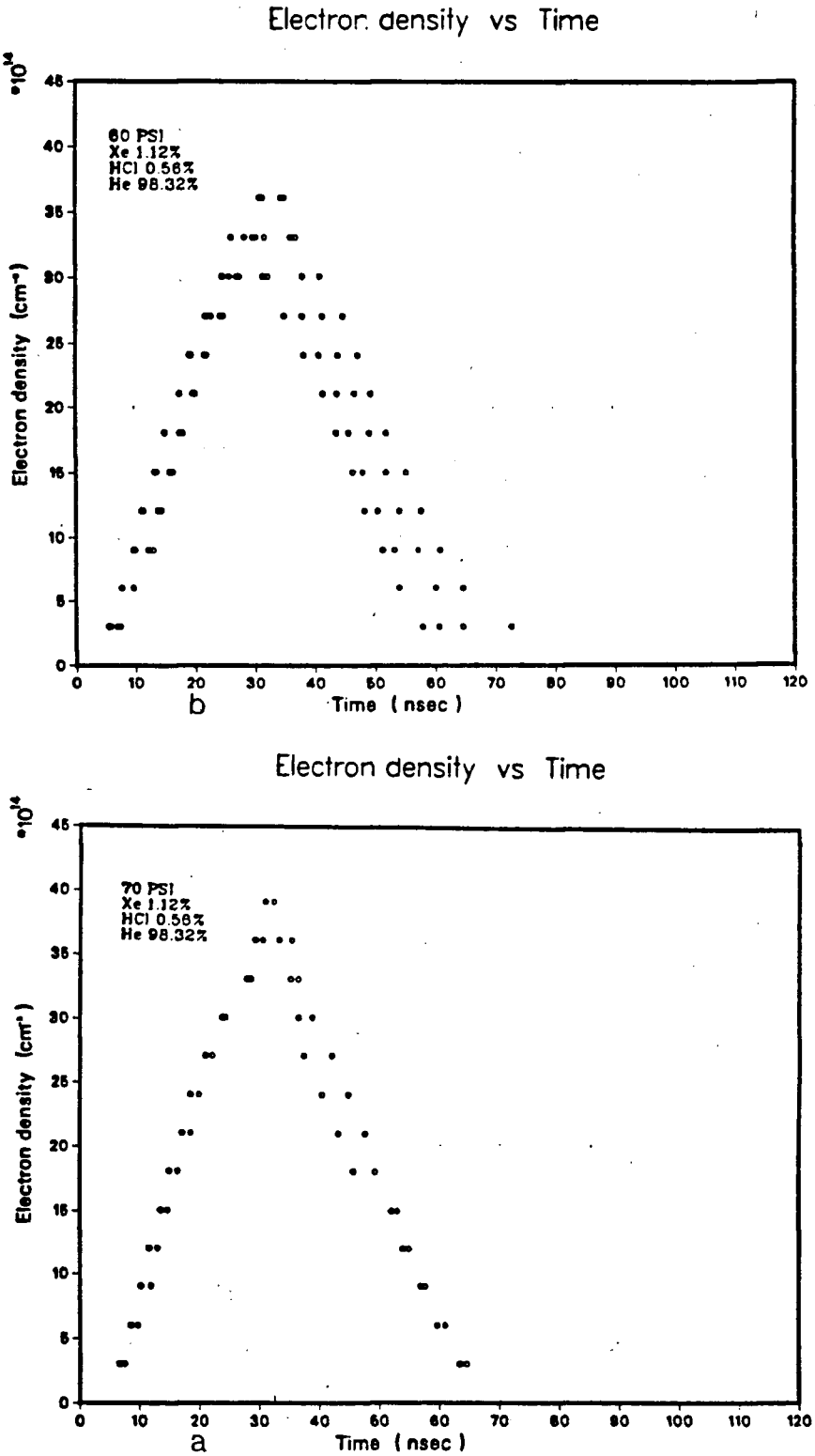

Figure 6.8: Graph of the electron density as a function of time at (a) 70 Psi, (b) 60 Psi. 30 KV, in a gas mix contained 1.12%(Xe), 0.56%(HCl), and 98.32%(He).

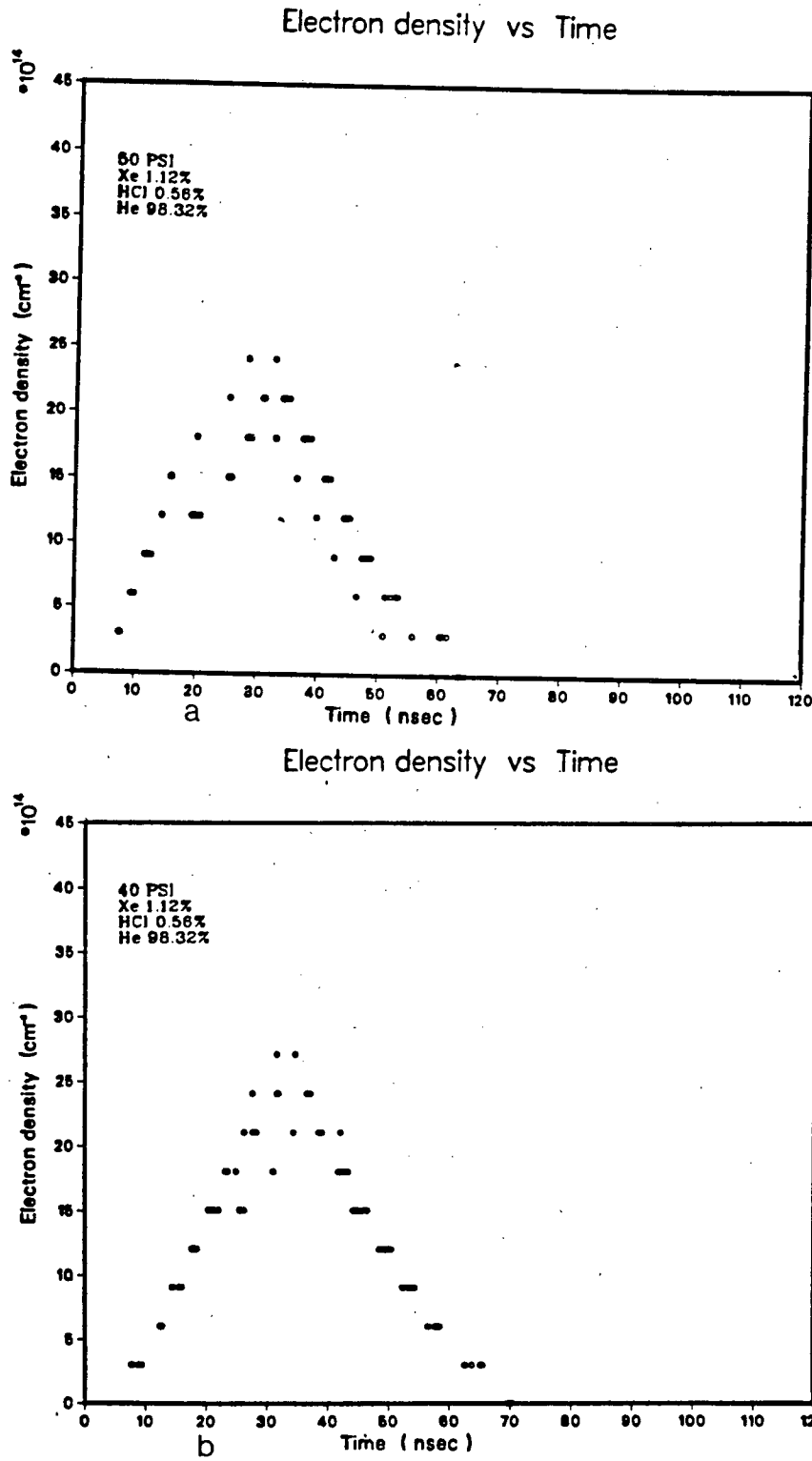

Figure 6.9: Graph of the electron density as a function of time at (a) 50 Psi, (b) 40 Psi. 30 KV, in a gas mix contained 1.12%(Xe), 0.56%(HCl), and 98.32%(He).

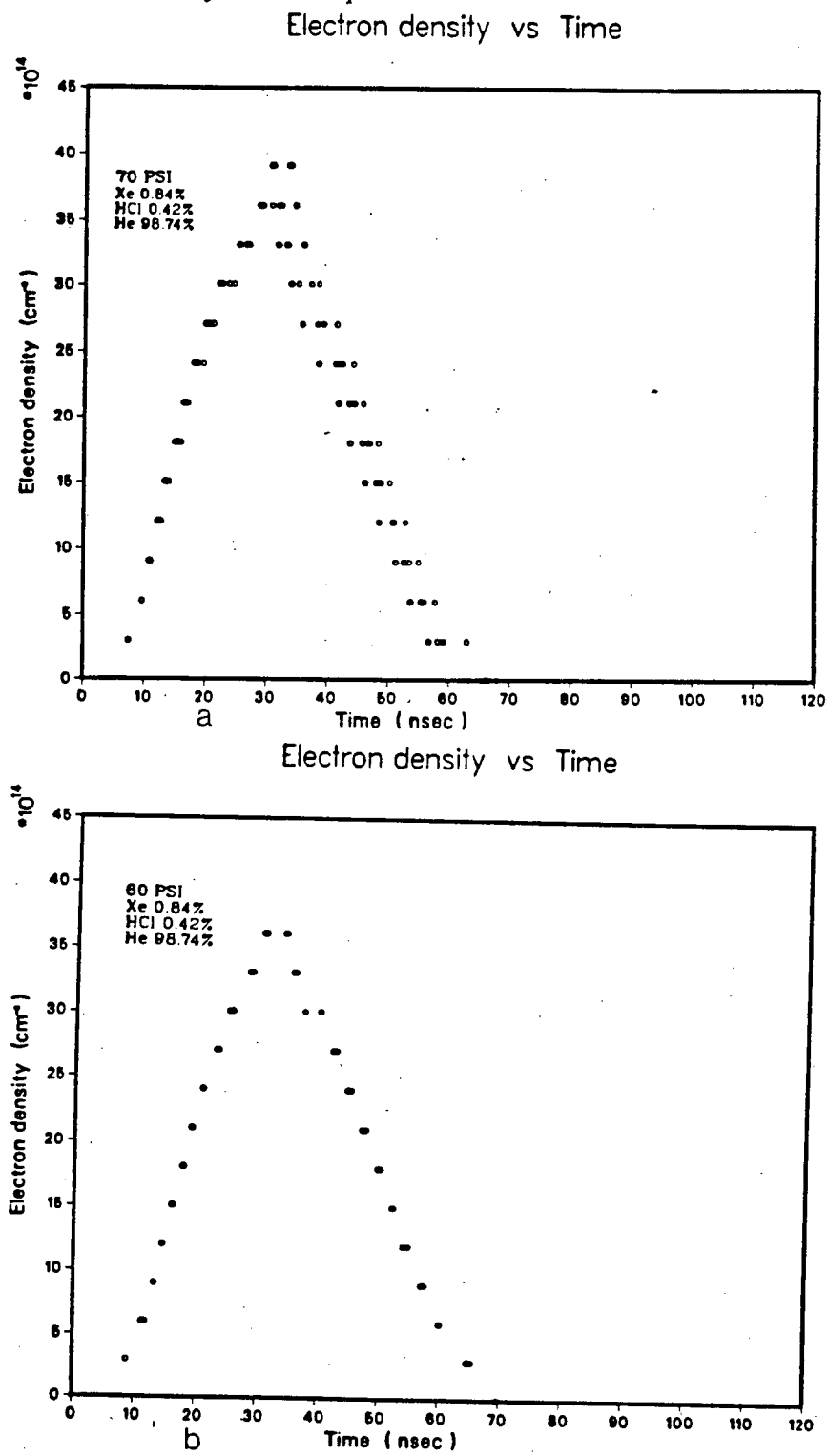

Figure 6.10: Graph of the electron density as a function of time at (a) 70 Psi, (b) 60 Psi. 30 KV, in a gas mix contained 0.84%(Xe), 0.42%(HCl), and 98.74%(He).

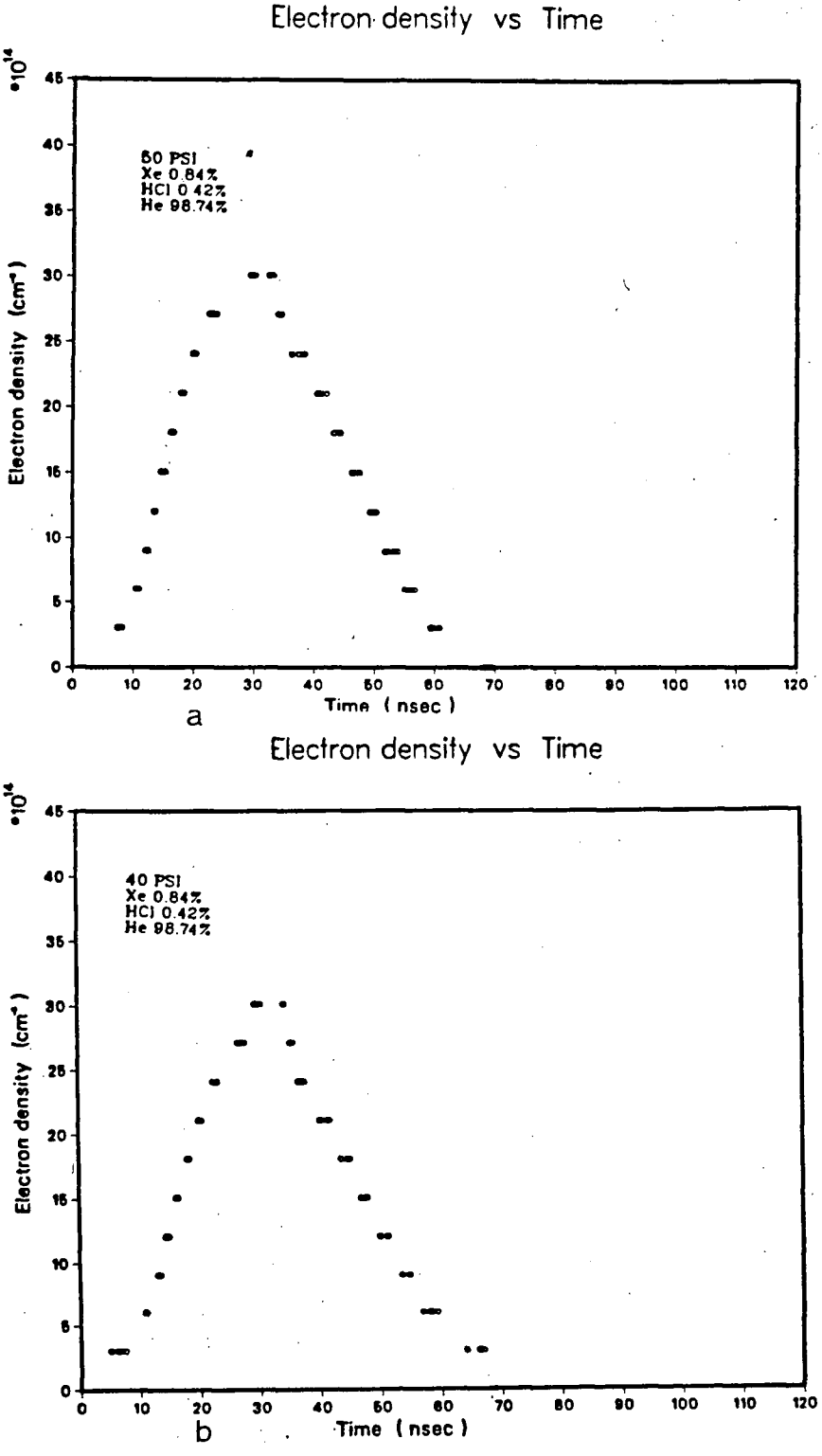

Figure 6.11: Graph of the electron density as a function of time at (a) 50 Psi, (b) 40 Psi. 30 KV, in a gas mix contained 0.84%(Xe), 0.42%(HCl), and 98.74%(He).

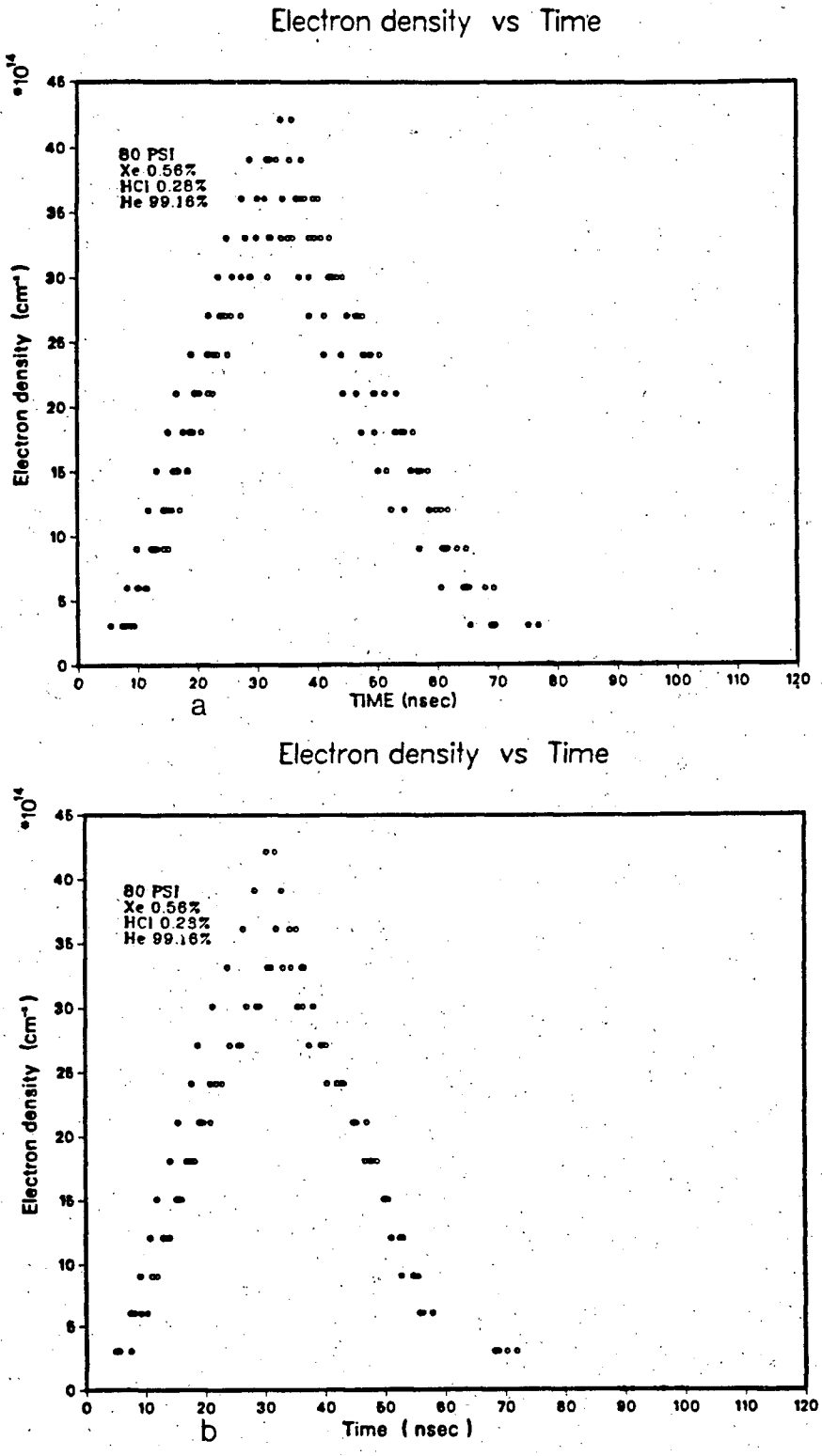

Figure 6.12: Two graphs of the electron density as a function of time at 80 Psi, (a) at 30 KV, (b) at 25 KV in a gas mix contained 0.56%(Xe), 0.28%(HCl), and 99.16%(He).

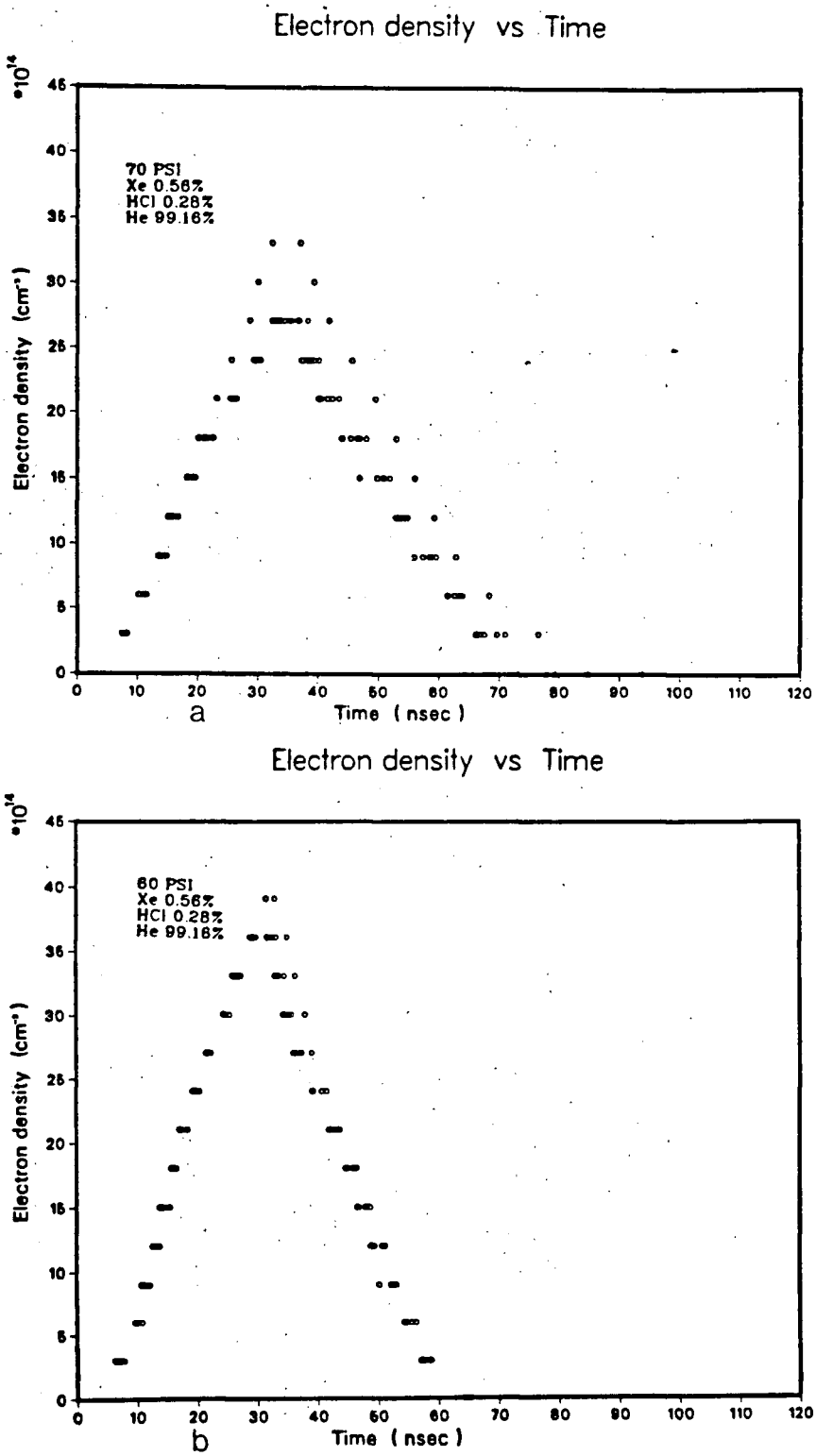

Figure 6.13: Graph of the electron density as a function of time at (a) 70 Psi, (b) 60 Psi. 30 KV, in a gas mix contained 0.56%(Xe), 0.28%(HCl), and 99.16%(He).

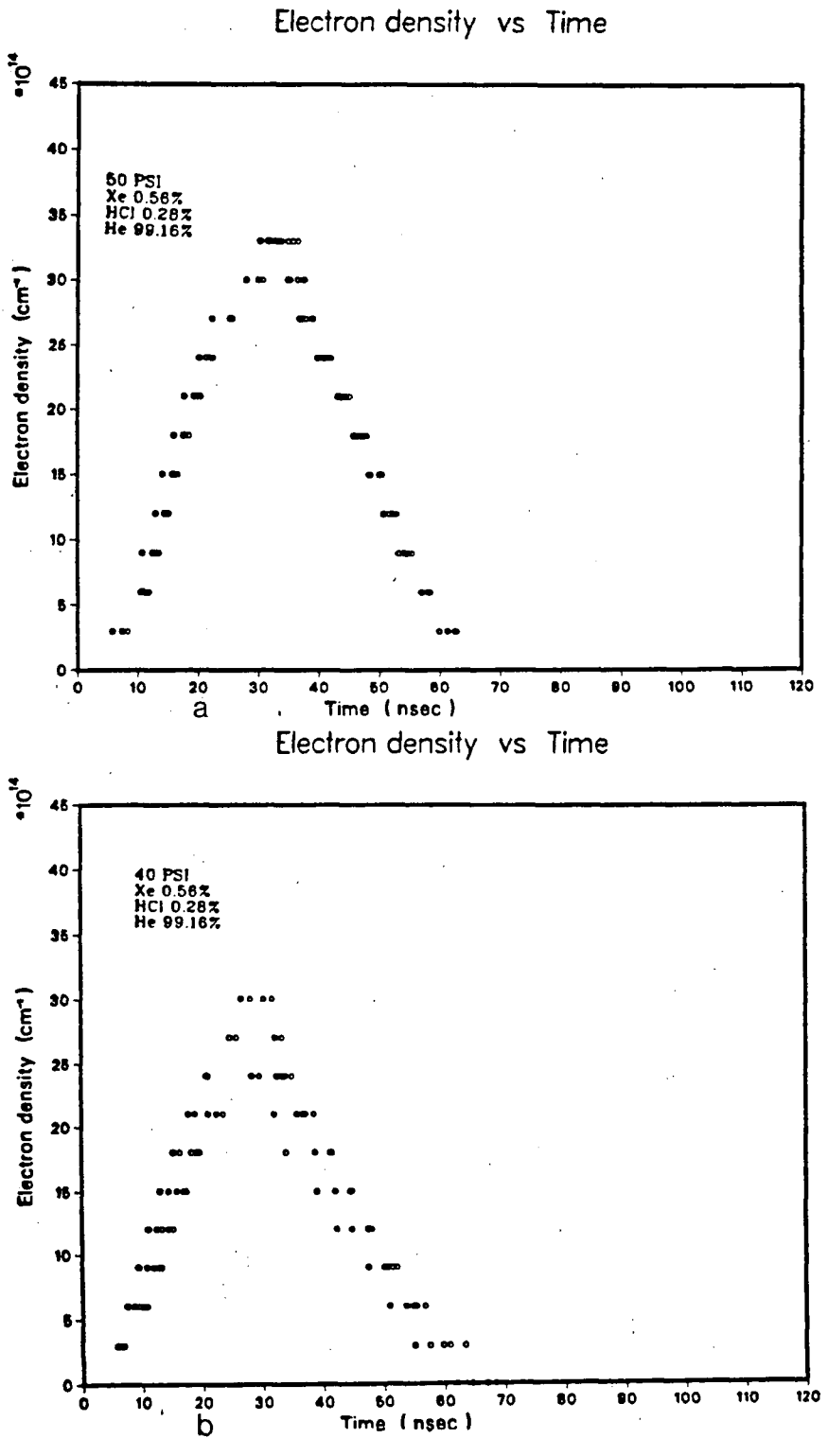

Figure 6.14: Graph of the electron density as a function of time at (a) 50 Psi, (b) 40 Psi. 30 KV, in a gas mix contained 0.56%(Xe), 0.28%(HCl), and 99.16%(He).

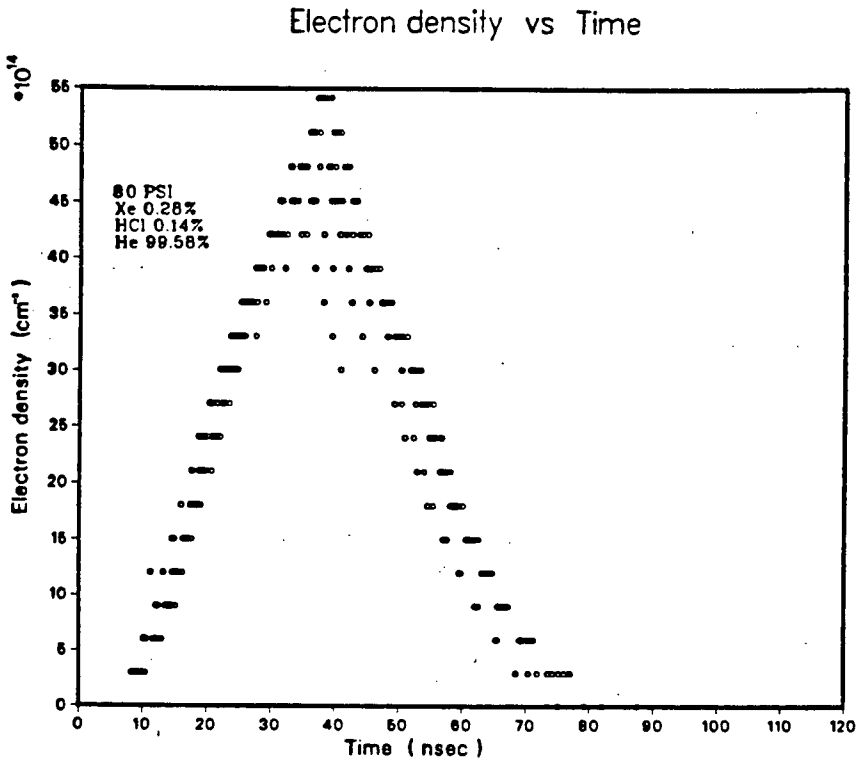

Figure 6.15: Graph of the electron density as a function of time at 80 Psi, 30 KV, in a gas mix contained 0.28%(Xe), 0.14%(HCl), and 99.58%(He).

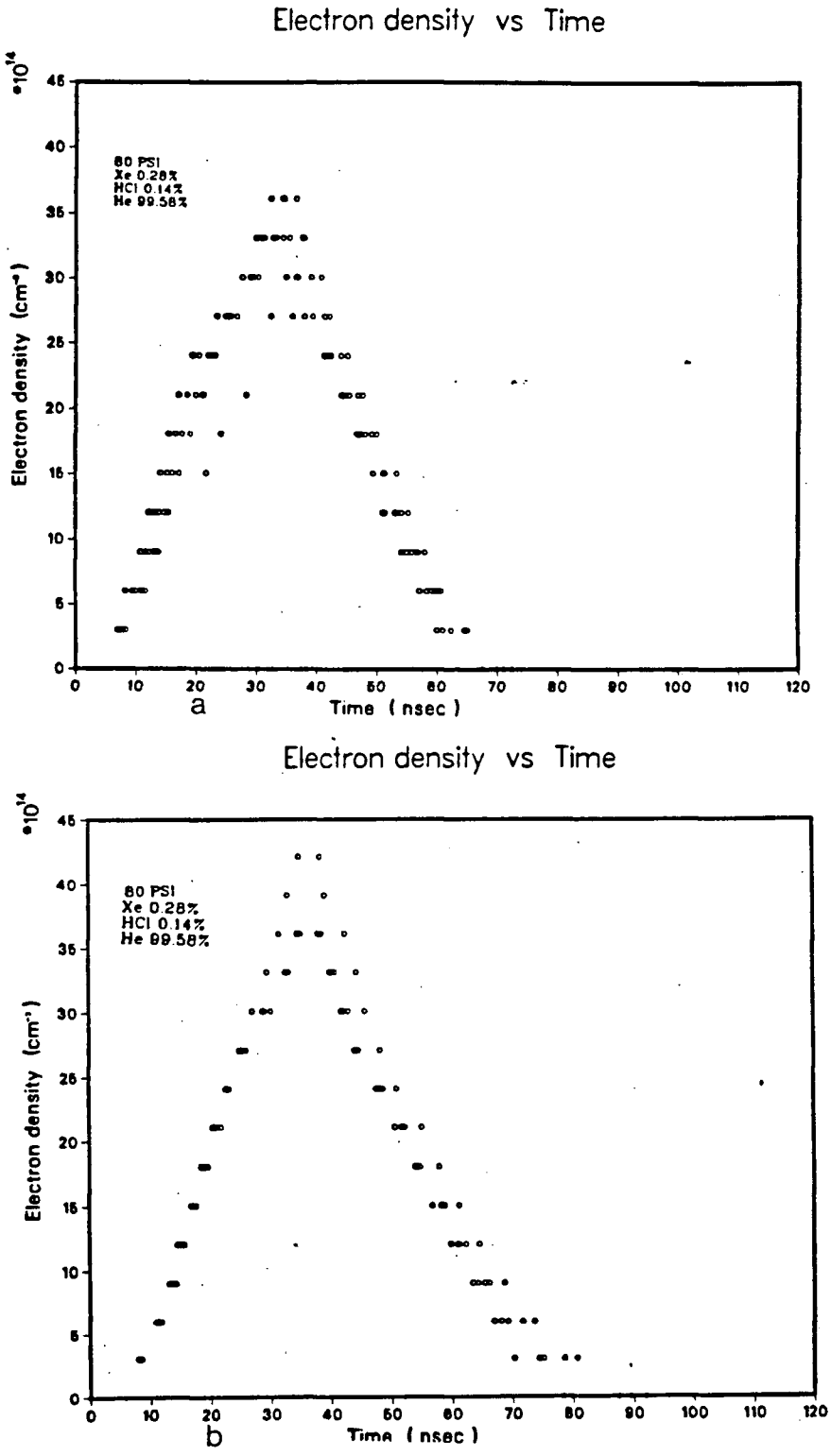

Figure 6.16: Two graphs of the electron density as a function of time at 80 Psi, 30 KV, in a gas mix contained 0.28%(Xe), 0.14%(HCl), and 99.58%(He).

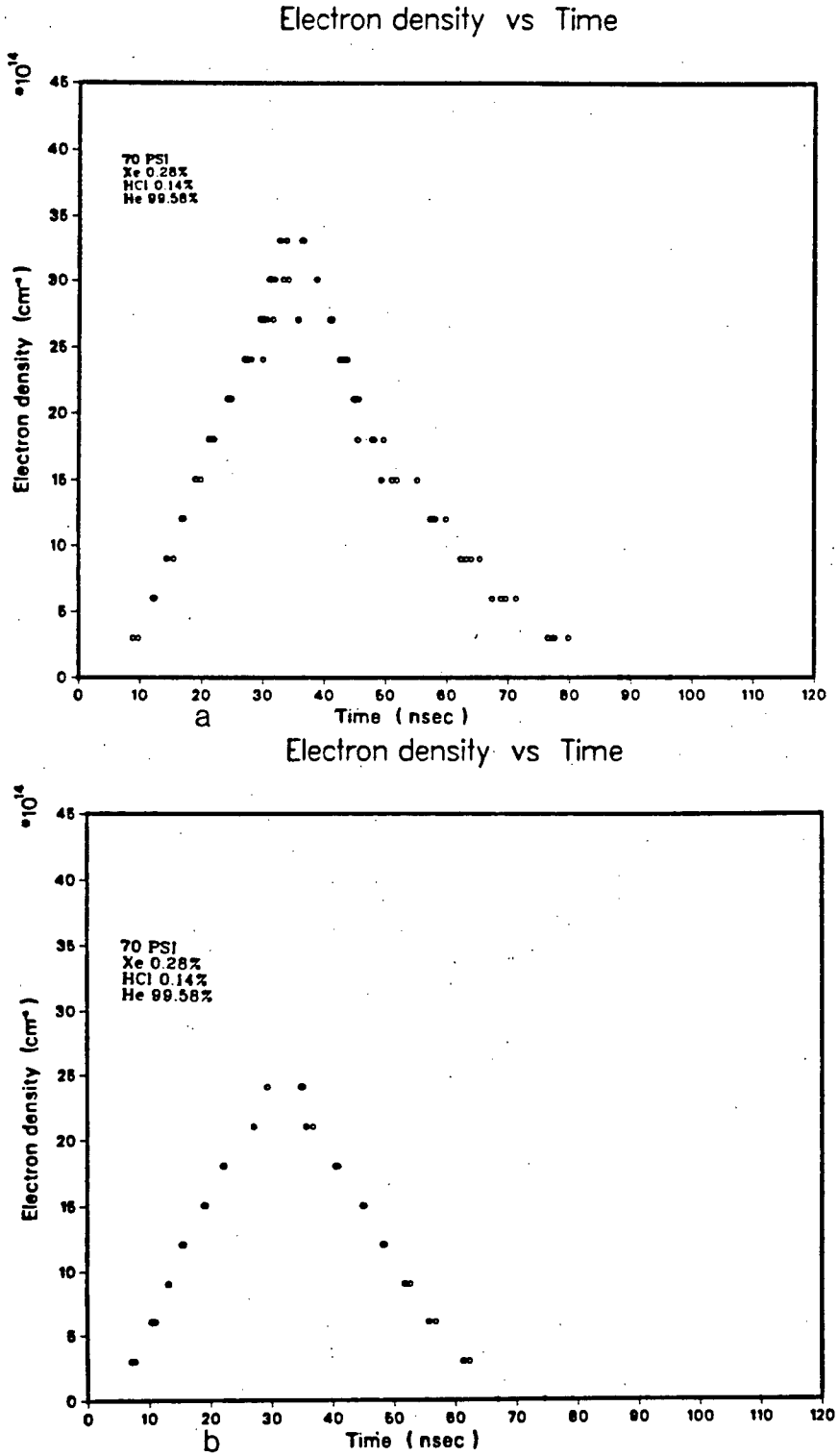

Figure 6.17: Two graphs of the electron density as a function of time at 70 Psi, 30 KV, in a gas mix contained 0.28%(Xe), 0.14%(HCl), and 99.58%(He).

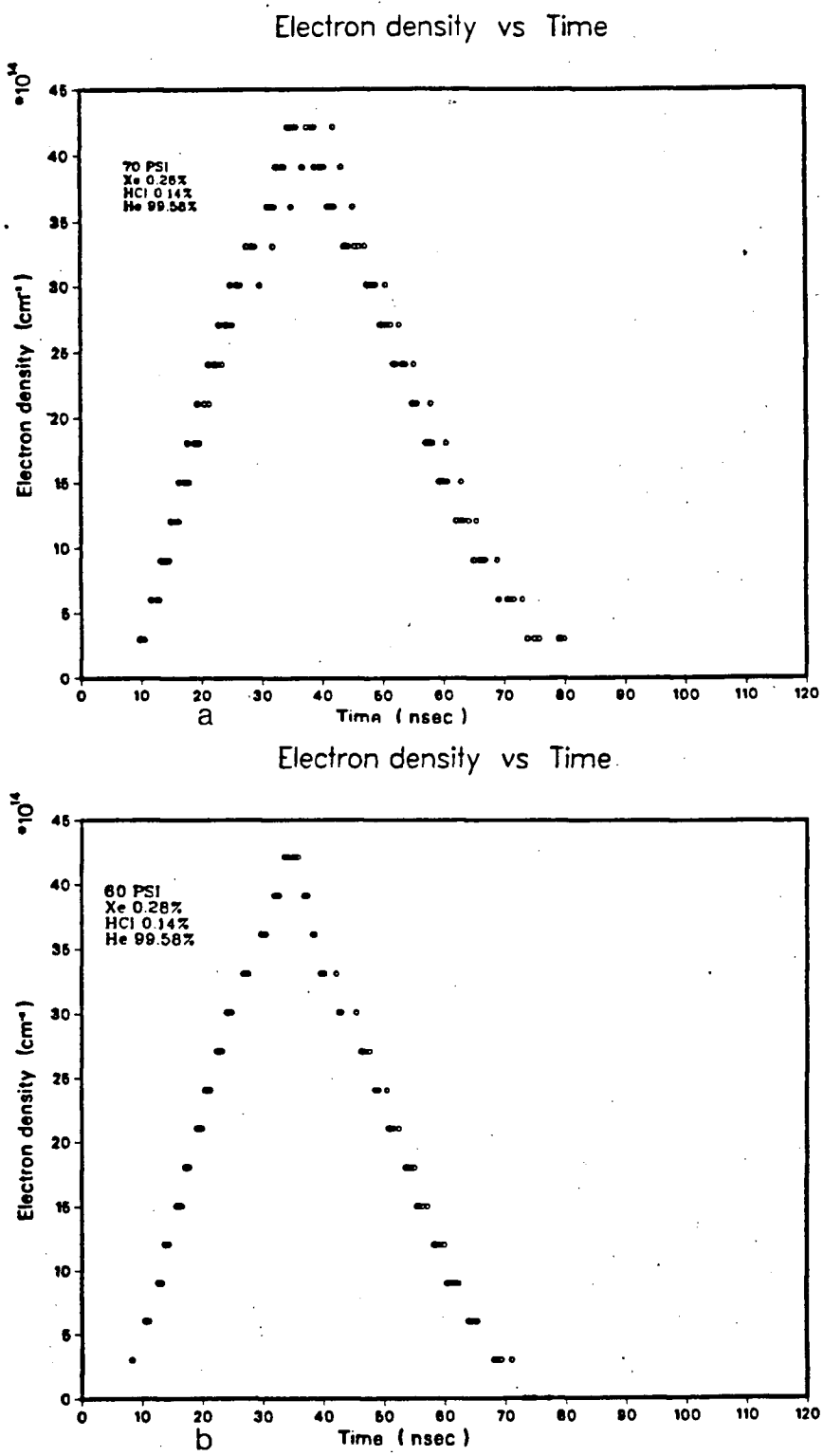

Figure 6.18: Graph of the electron density as a function of time at (a) 70 Psi, (b) 60 Psi. 30 KV, in a gas mix contained 0.28%(Xe), 0.14%(HCl), and 99.58%(He).

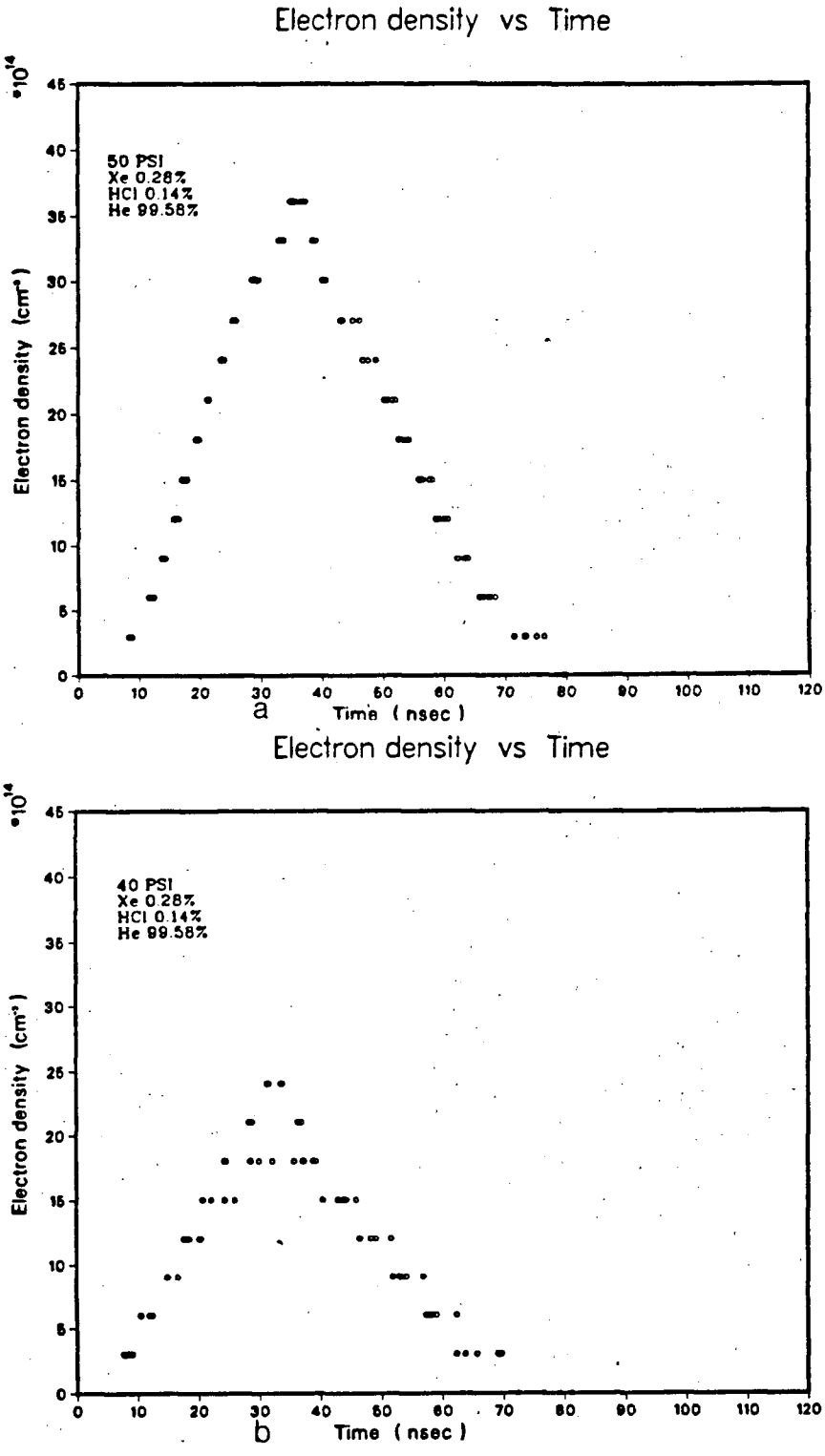

Figure 6.19: Graph of the electron density as a function of time at (a) 50 Psi, (b) 40 Psi. 30 KV, in a gas mix contained 0.28%(Xe), 0.14%(HCl), and 99.58%(He).

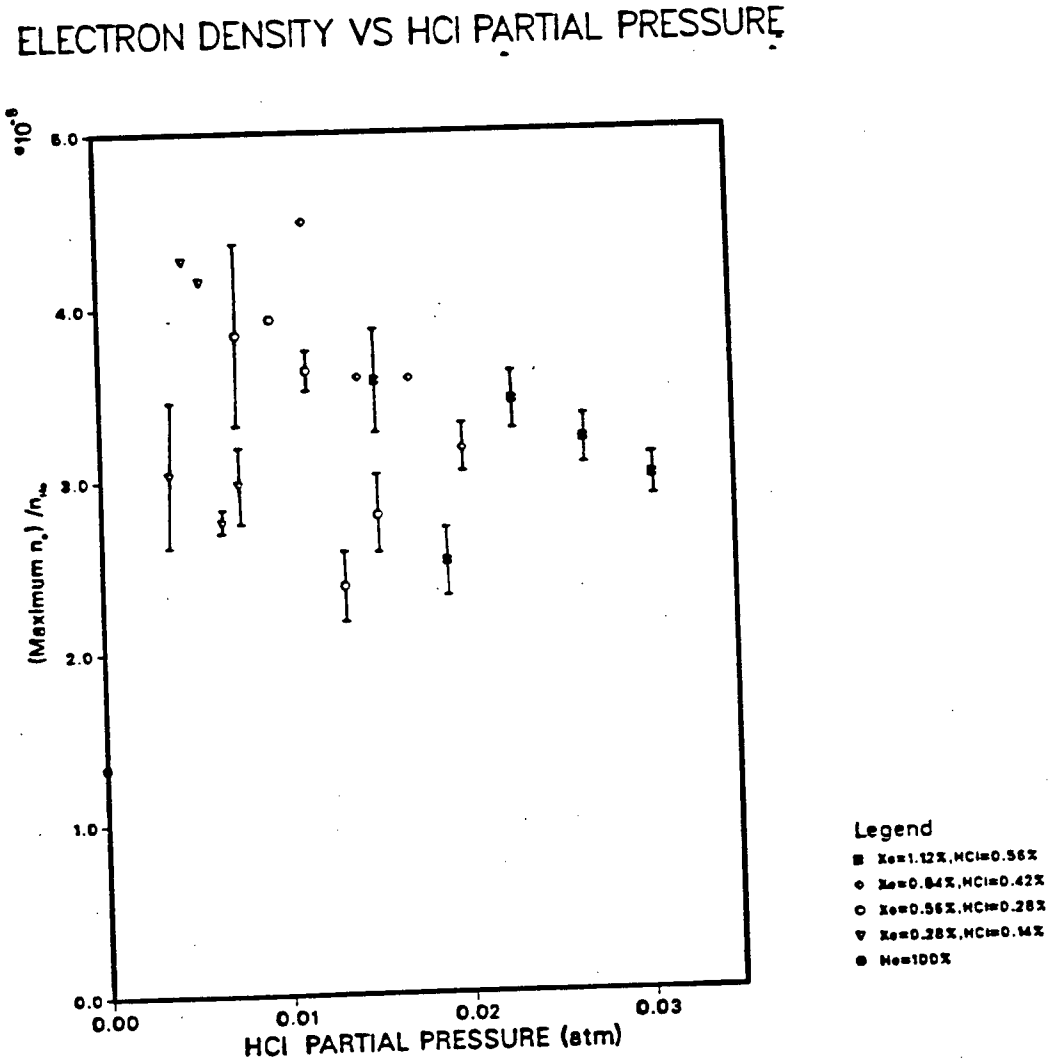

Figure 6.20: Electron density as a function of HCl partial pressure.

6.2.8 IR $XeCl^*$ Emission

By blocking the reference arm of the original Michelson interferometer, we detected an infrared emission about ten meters away from the discharge $XeCl$ laser. The same emission was first reported by Dyer et al. [65] and later by Ford et al. [1]. The laser IR pulse was observed to pass through the Ge filter, which suggests that the lasing wavelength is $\geq 2\mu m$. However, no attempt was made to measure either the wavelength or the energy. Figure (6.21) shows the IR pulse.

6.3 Electron Temperature

Measurements of the electron temperature can reveal some information on the collisional mechanisms and reactions dominating the $XeCl$ lasers.

We were able to calculate the electron temperature by the following simple analysis:

After producing the electrons in the discharge, they gain energy from the electric field. And since over 98% of the gas contains He, the electrons suffer several collisions with He atoms, with an effective collisional frequency ν_c. The electrons then reach a constant velocity (drift velocity) V_d, where they just drift along the electric field. Then the momentum change of the electrons, due to collisions, must balance the electric field's force on the electrons. That is:

$$m_e V_d \nu_c = eE \tag{6.9}$$

giving a drift velocity

$$V_d = \frac{eE}{m_e \nu_c} \tag{6.10}$$

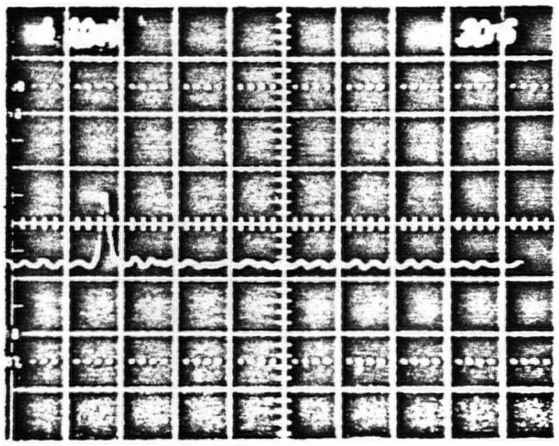

Figure 6.21: The IR emission obtained in a gas mix contained 1.12%(Xe), 0.56%(HCl), and 98.32%(He) at 80 Psi, 30 KV.

or

$$V_d = \frac{eE\tau_c}{m_e} \tag{6.11}$$

where τ_c is the average collisional time and is equal to $\frac{\lambda_c}{V_{th}}$, where λ_c is the mean free path of the electrons, and V_{th} is the thermal velocity of the electrons. Therefore, combining the expression for τ_c and equation (6.11) gives

$$V_d = \frac{eE\lambda_c}{m_e V_{th}} \tag{6.12}$$

Knowing that $\lambda_c = \frac{1}{Q_{He} n_{He}}$, where Q_{He} is the electron helium momentum transfer cross section $\approx 5 \times 10^{-16} cm^2$ [66], and, by combining the expressions for λ_c and V_d, we get

$$V_d = \frac{eE}{m_e V_{th} n_{He} Q_{He}} \tag{6.13}$$

Using the expression of the discharge resistance (5.7) in the above expression of the drift velocity gives

$$V_{th} = \frac{< n_e >_t e^2 A < R >_t}{n_{He} Q_{He} m_e d} \tag{6.14}$$

where $<>_t$ means averaging over time.

Due to the noise in the drift velocities, it was decided to average the drift velocities over time. Also, the discharge resistances were averaged over time to reduce the noise level in the measured traces.

Equation (6.14) gives an expression of the average thermal velocity, which, in turn, permits a direct calculation of the electron temperature.

6.3.1 Variations of the Electron Temperature with HCl

A plot of the electron temperature against HCl concentration (figure (6.22)) shows a noticeable decrease of the electron temperature as a result of increasing the HCl pressure

(or concentration). This behaviour can be attributed to a mechanism which results in the cooling of the electrons through collisions with the HCl molecules.

Electrons having energy above the excitation energy threshold of the HCl molecule can experience a loss of energy during inelastic collisions with the HCl molecules, with a characteristic collisional time:

$$\tau_c \approx \frac{1}{n_{Hcl} V_{th} Q_{reaction}} \tag{6.15}$$

where $Q_{reaction}$ is the corresponding reaction cross section.

Here, we will compare the relative importance of the two most likely mechanisms responsible for electron cooling: The vibrational excitation of the HCl molecules and the dissociative attachment of the HCl molecules.

In the reaction

$$e + HCl(v = 0) \longrightarrow HCl(v = 1) + e \tag{6.16}$$

the only significant vibrational excitation level is from the ground level ($v = 0$) to the first excited state ($v = 1$), where the maximum excitation cross section of such transition is $Q_{0\to1} = 17 \times 10^{-16} cm^2$, whereas the maximum cross section for ($v = 1$ to $v = 2$) at $1.5 \times 10^{-16} cm^2$, is an order of magnitude lower [67].

For $\approx$1 ev electrons and $n_{HCl} \approx 10^{18} cm^{-3}$, we get $\tau_c \approx 0.015$ $nsec$.

Next, we consider the dissociative attachment of the HCl molecules. The maximum collisional cross section for dissociative attachment [68] is $Q_{diss} = 1.95 \times 10^{-17} cm^2$; for 1 ev electrons and the same HCl density, we get $\tau \approx 1.28$ $nsec$, which is much longer than the vibrational excitation collisional time. We therefore conclude that electrons cool via inelastic collisions with the HCl molecules.

Some of the values of the electron temperature for partial HCl pressures below 0.015 atm are unphysically high for a glow discharge, which suggest that the discharge width

may not be constant (as assumed in equation (6.14)) for different Xe and HCl concentrations. But it may in fact be smaller, though the examination of the laser output profile did not indicate this.

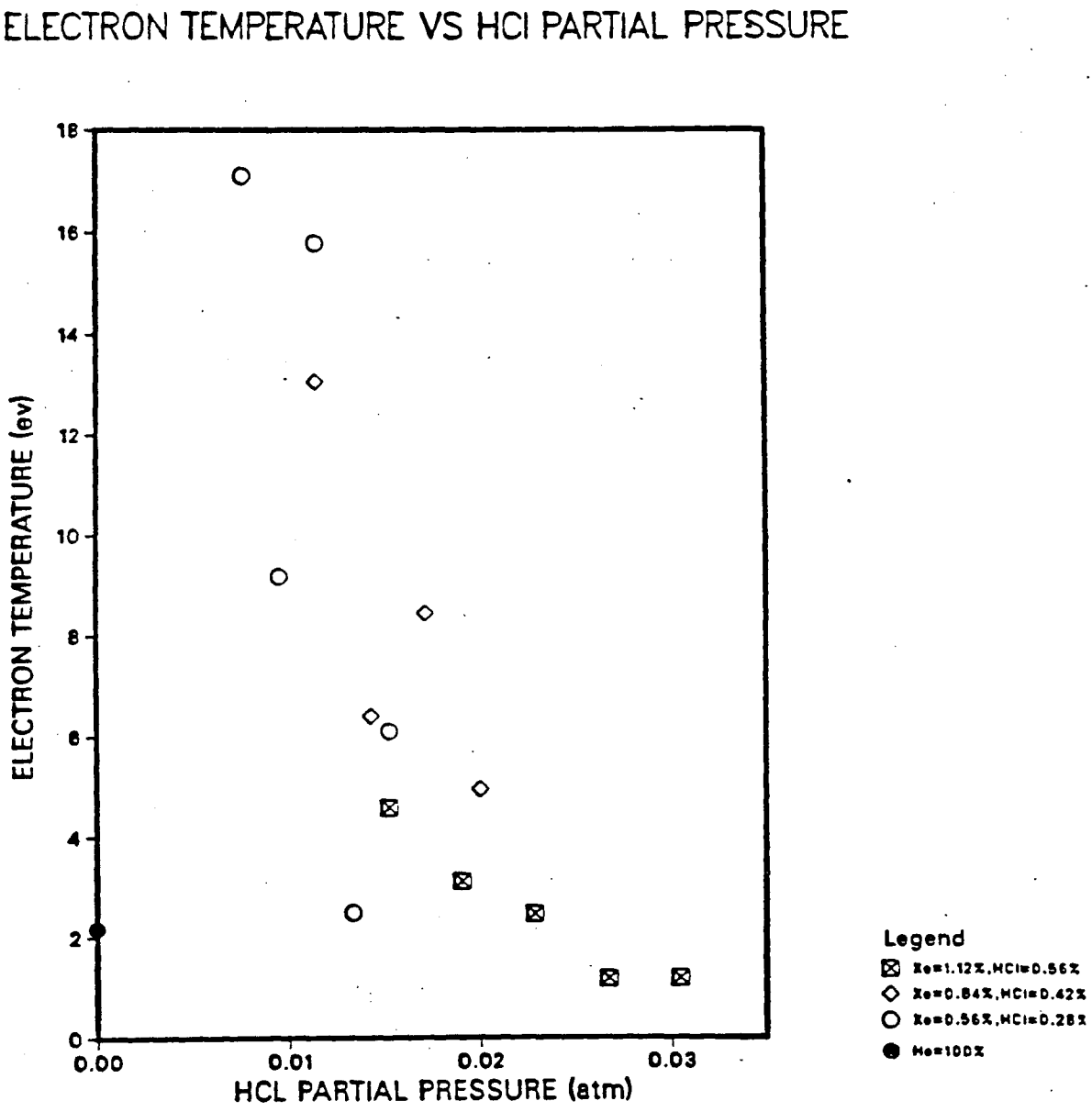

Figure 6.22: Electron temperature as a function of HCl partial pressure.

Chapter 7

Discussion and Conclusions

The performance characteristics of a u.v. preionized, high pressure $XeCl$ laser have been studied. The laser output energy was found to depend on the laser gas composition, the total filling pressure, and the charging voltage.

The typical electrical efficiency (a fraction of the energy stored in the discharge circuit ($\frac{1}{2}NCV^2$ where N is the number of the capacitors = 24) to that of the energy of the pulse) is 0.3%, and the highest extractable energy per unit volume is 3.8 J/l. These conditions were achieved in a gas mixture containing Xe (1.12%), HCl (0.56%), and He (98.32%). This optimal composition of the active lasing mixture was determined by the level of the uniformity of the discharge and the magnitude of output energy obtained from the laser. The output energy can be scaled up by increasing the total gas pressure and charging voltage. We found that if the $XeCl$ laser discharge parameters are not carefully controlled, discharge arcing will develop, leading to the termination of the laser action.

The current rise time at the optimum conditions was found to be 24 *nsec*.

Figure (7.1) shows the relative timing of the voltage, current, laser pulse, and the electron density. The graph shows that the laser output pulse starts at the peak of the current pulse. On the other hand, the density profile peaks at the maximum of the current pulse and decays back to zero as the current pulse returns to zero.

The electron density is found to increase once Xe and HCl were added to the He gas. For example, going from 100% He (at 80 Psi) to a mix containing 1.12 % (Xe),

0.56 % (HCl), and 98.32 % (He) increases the electron density from 1.81×10^{15} cm^{-3} to 4.01×10^{15} cm^{-3}, respectively. This increase in the electron density is mainly a result of the introduction of easily ionized molecules. For instance, Xe, Xe^{*}, Xe^{**}, and Cl have low ionization energies of 12.2 ev, 3.8 ev, 2.1 ev, and 13.01 ev, respectively, which are lower than that of He (24.58 ev).

The breakdown voltages for the same pressure and different Xe and HCl concentrations are found to have almost the same value. This is because the lasing gas mixture contains over 98% He. Therefore, the breakdown voltage is controlled by the pressure of the He gas. The results presented in this work provide strong evidence that the electron loss mechanism is due to the dissociative attachment of HCl molecules, and that the electron cooling mechanism is mainly due to HCl vibrational excitations. In the following paragraph, the equation governing the electron cooling mechanism is discussed.
The electron temperature conservation equation is given by:

$$n_e\frac{dT_e}{dt} = (heating\ rate) - (cooling\ rate) \tag{7.1}$$

where the electron heating required to maintain the electron temperature is due to the joule heating, that is J^2/σ, where J is the current density and σ is the electrical conductivity. The electron cooling rate is due to several mechanisms, for example, vibrational excitations of HCl molecules and the excitations of Xe and He. In the following study, we will consider only one cooling mechanism, primarily the vibrational excitations of HCl molecules. This presents an approximation for the situation when the pressure of HCl dominates the electron losses. Therefore, we write the temperature conservation equation (i.e. equation (7.1)) as:

$$n_e \frac{dT_e}{dt} = \frac{J^2}{\sigma} - n_e \nu_{HCl} \xi \tag{7.2}$$

here

$$\sigma = \frac{n_e e^2}{m_e n_{He} Q_{He} V_{th}} \tag{7.3}$$

$$\xi = \frac{2 m_e T_e \delta}{m_{HCl}} \tag{7.4}$$

and ξ is the e-HCl energy transfer per collision, δ is the energy loss factor per collision, and $\nu_{HCl} = n_{HCl} Q_{0\to 1} V_{th}$ is the e-HCl vibrational excitation collision frequency.

At equilibrium, $\frac{dT_e}{dt} = 0$, and equation (7.2) reduces to

$$\frac{J^2}{\sigma} = n_e n_{HCl} Q_{0\to 1} V_{th} \xi \tag{7.5}$$

The electron current density and the electric field are related by Ohm's law

$$J = \sigma E \tag{7.6}$$

Therefore, by using equations (7.3) (7.4) (7.5) and(7.6), we get

$$\frac{(eE)^2}{m_e n_{He} Q_{He} V_{th}} = n_{HCl} Q_{0\to 1} V_{th} \frac{m_e}{m_{HCl}} \delta T_e \tag{7.7}$$

Rearranging the above equation and using the fact that $T_e = \frac{1}{2} m_e V_{th}^2$, one can arrive at an expression relating the electron temperature to the density of HCl molecules

$$T_e = \sqrt{\frac{m_{HCl}}{4 Q_{0\to 1} Q_{He} m_e n_{He} \delta}} \frac{eE}{\sqrt{n_{HCl}}} \tag{7.8}$$

Equation(7.8) shows that the electron temperature is related to the inverse square root of the HCl density. Substituting the corresponding numerical values (m_{HCl}=6.1×10^{-26} Kg, $n_{He} \approx 10^{26}\ m^{-3}$, $E \approx 4 \times 10^5$ v/m, $Q_{0\to 1}$ = 17×$10^{-20}\ m^2$, Q_{He} = 5×$10^{-20}\ m^2$,

$n_{HCl} \approx 5 \times 10^{-20}\ m^{-3}$, and $\delta \approx 10^3$) in equation (7.7) results in an electron temperature of $4.01 \times 10^{-19}\ j$, i.e. $\approx 2.5\ ev$. Unfortunately, there is no published value of the energy loss factor for e-HCl collision; therefore, the value for e-CO_2 collision was tried [69]. With the previous numbers in mind, equation (7.8) can be reduced to

$$T_e = (2.8 \times 10^{-7}) \frac{1}{\sqrt{n_{HCl}}} \tag{7.9}$$

A plot of T_e as a function of $\frac{1}{\sqrt{n_{HCl}}}$ should give a slope of $\approx 2.8 \times 10^{-7}\ jm^{-3/2}$. The results of the experimental values are presented in figure (7.2), and the calculated slope is $2.25 \times 10^{-6}\ jm^{-3/2}$. This is larger than the predicted slope. On the other hand, using an energy loss factor of 100 gives a predicted slope $\approx 10^{-6}\ jm^{-3/2}$, which is similar to the one evaluated from figure (7.2).

From the above discussion, we find that if δ is chosen to be equal to 100, the model is consistent with the experimental results.

Finally, this laser will serve as an amplifier for a table-top, terawatt, short pulse (a few femtoseconds) laser system which will be constructed later on.

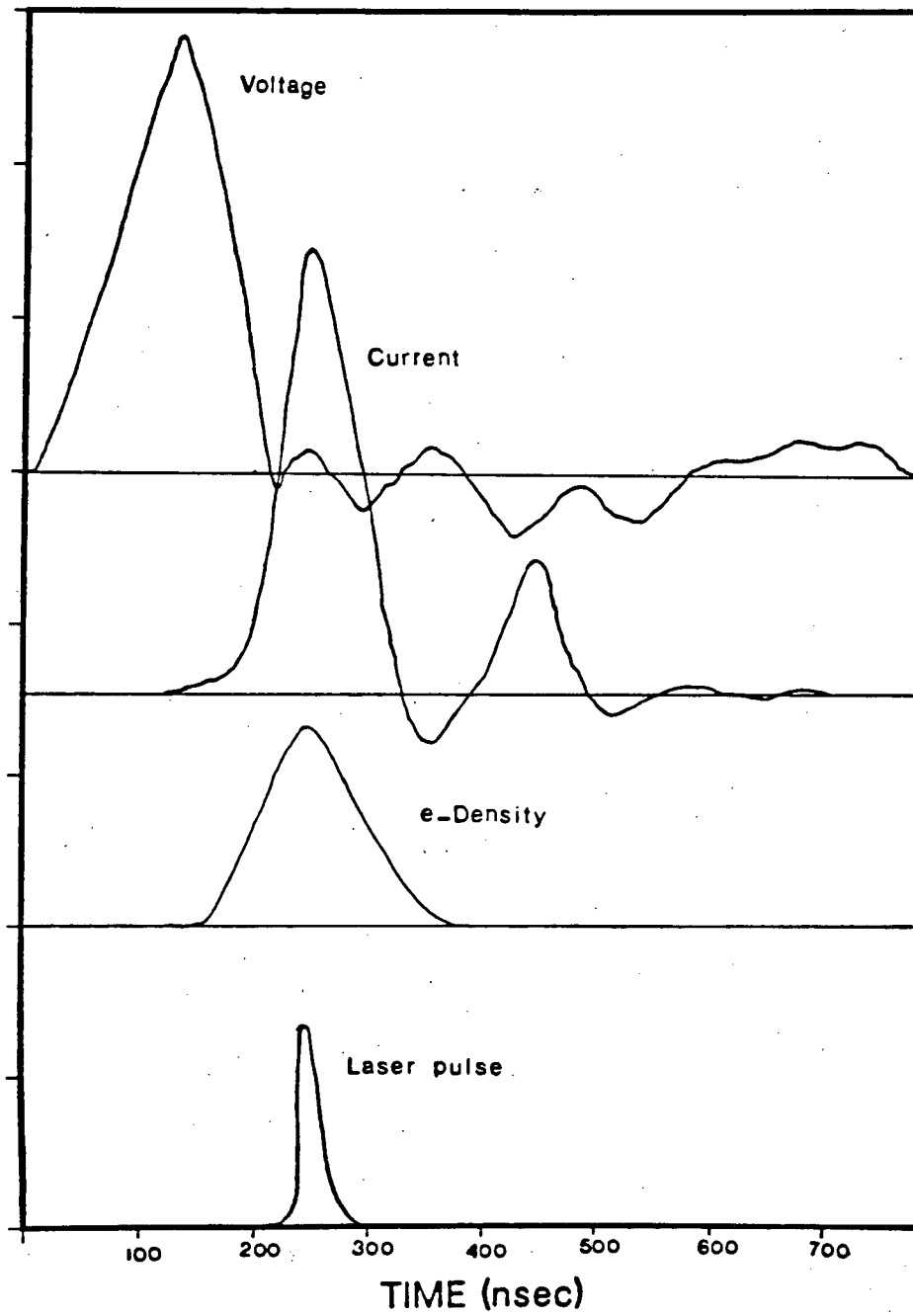

Figure 7.1: Relative timing of the laser parameters.

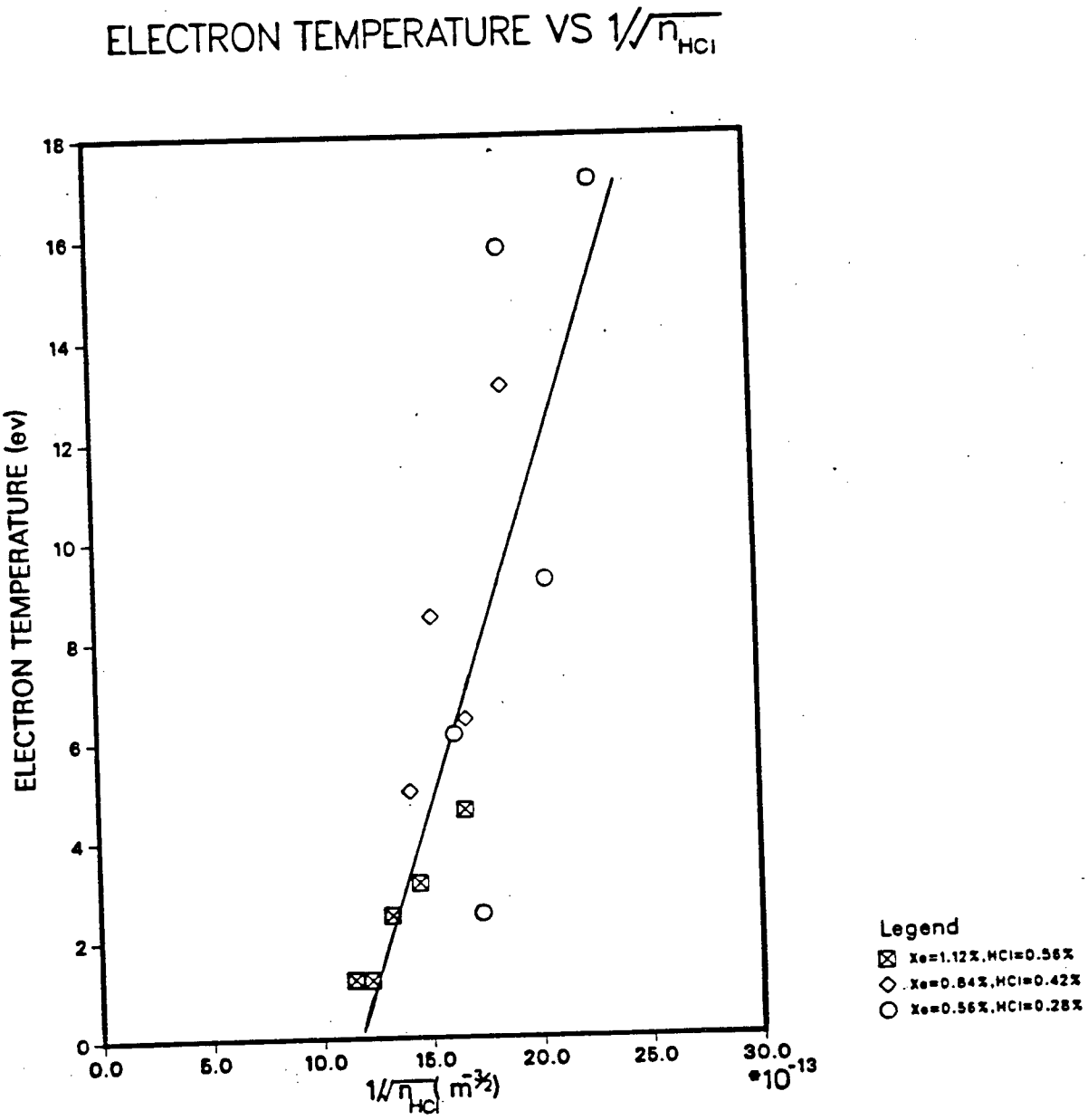

Figure 7.2: T_e as a function of $1/\sqrt{n_{HCl}}$.

Bibliography

[1] J. E. Ford, J. Meyer, and H. Houtman, Appl. Phys. Lett. Vol.48, 1639 (1986).

[2] G. Stewart, *Master Thesis, University of British Columbia,* (1986).

[3] M. Ohwa, and M. Obara, J. Appl. Phys. Vol.59, 32 (1986).

[4] H. Hokazono, K. Midorikawa, M. Obara, and T. Fujioka, J. Appl. Phys. Vol.56, 680 (1984).

[5] M. Maeda, A. Takahashi, T. Mizunami, and Y. Miyazoe, Jap. J. Appl. Phys. Vol.21, 1161 (1982).

[6] L. A. Levin, S. E. Moody, E. L. Klosterman, R. E. Center, and J. J. Ewing, IEEE J. Quantum Electron, QE_17, 2282 (1981).

[7] W. N. Hartley, and H. Ramage, R. Dublin Soc. Trans. Vol.7, 339 (1901).

[8] R. W. Wood, Phil. Mag. Vol.18, 240 (1909).

[9] S. Mrozowski, Z. Phys. Vol.76, 38 (1932).

[10] F. G. Houtermans, Helv. Phys. Acta. Vol.33, 933 (1960).

[11] R. J. Carbone, and M. M. Litvak, J. Appl. Phys. Vol.39, 2413 (1968).

[12] N. G. Basov, V. A. Danilychev, and Y. M. Popov, Sov. J. Quantum electron. Vol.1, 18 (1971).

[13] H. K. Koehler, L. J. Ferderber, D. L. Redhead, and P. J. Ebert, Appl. Phys. Lett. Vol.21, 198 (1972).

[14] S. K. Searles, and G. A. Hart, Appl. Phys. Lett. Vol.27, 243 (1975).

[15] J. J. Ewing, and C. A. Brau, Phys. Rev. A. Vol.12, 129 (1975).

[16] J. E. Velazco, and D. W. Setser, J. Chem. Phys. Vol.62, 1990 (1975).

[17] J. J. Ewing, and C. A. Brau, Appl. Phys. Lett. Vol.27, 350 (1975).

[18] R. Burnham, and N. Djeu, Appl. Phys. Lett. Vol.29, 707 (1976).

[19] D. E. Rothe, and R. A. Gibson, Opt. Commun. Vol.22, 265 (1977).

[20] A. J. Andrews, A. J. Kearsley, C. A. Webb, and S. C. Haydon, Opt. Commun. Vol.20, 265 (1977).

[21] A. J. Kearsley, A. J. Andrews, and C. E. Webb, Opt. Commun. Vol.31, 181 (1979).

[22] W. J. Sarjeant, A. J. Alcock, and K. E. Leopold, Appl. Phys. Lett. Vol.30, 635 (1977).

[23] T. S. Fahlen, IEEE J. Quantum Electron. QE_15, 311 (1979).

[24] G. S. Ernst, A. B. M. Nieuwenhuis, and K. M. Abramski, IEEE J. Quantum Electron. QE_21, 1127 (1985).

[25] V. Hansson, and H. M. Von Bergmann, Rev. Sci. Inst. Vol.50, 1542 (1979).

[26] H. Shields, A. J. Alcock, and R. S. Taylor, Appl. Phys. B. Vol.31, 27 (1983).

[27] T. Letardi, S. Bollanti, A. De Angelis, P. Di Lazzaro, I. Giabbi, G. Giordano, and E. Sabia, Il Nuovo Cimento. Vol.9D, 873 (1987).

[28] C. P. Wang, H. Mirels, D. G. Sutton, and S. N. Suchard, Appl. Phys. Lett. Vol.28, 522 (1976).

[29] R. Burnham, F. X. Powell, and N. Djeu, Appl. Phys. Lett. Vol.29, 30 (1976).

[30] J. M. Hoffman, A. K. Hays, and G. C. Tisone, Appl. Phys. Lett. Vol.28, 538 (1976).

[31] T. S. Fahlen, J. Appl. Phys. Vol.49, 455 (1978).

[32] Y. A. Kudryavtsev, and N. P. Kuz'mina, Sov. J. Quantum Electron. Vol.7, 173 (1977).

[33] V. N. Ishchemko, V. N. Lisitsyn, and A. M. Razhev, Opt. Commun. Vol.21, 30 (1977).

[34] R. Burnham, Opt. Commun. Vol.24, 161 (1978).

[35] R. Sze, and P. Scott, Appl. Phys. Lett. Vol.33, 419 (1978).

[36] R. Sze, IEEE J. Quantum Electron. QE_15, 1338 (1979).

[37] C. Jianwen, F. Shufen, L. Miaochong, Appl. Phys. Lett. Vol.37, 883 (1980).

[38] R. Sze, and E. Seegmiller, IEEE J. Quantum Electron. QE_17, 81 (1980).

[39] S. Watanabe, and A. Endoh, Appl. Phys. Lett. Vol.41, 799 (1982).

[40] A. Takahashi, M. Maeda, and Y. Noda, IEEE J. Quantum Electron. QE_20, 1196 (1984).

[41] V. Y. Baranov, V. M. Borison, D. N. Molchanov, V. P. Norikov, and O. B. Khritoforov, Sov. J. Quantum Electron, Vol.17, 978 (1987).

[42] K. Yamada, K. Miyazaki, T. Hasama, and T. Sato, IEEE J. Quantum Electron. Vol.24, 177 (1988).

[43] C. A. Brau, *Excimer lasers*, ed. C. K. Rhodes, (Berlin:Spriger) (1983).

[44] J. Tellinghusen, J. M. Hoffman, G. C. Tisone, and A. K. Hays, J. Chem. Phys. Vol.64, 2484 (1976).

[45] D. Lo, and C. Zheng, J. Phys. D. 715, (1987).

[46] T. Y. Chang, Rev. Sci. Inst. Vol.44, 405 (1973).

[47] R. Tennant, *Laser Focus,* Vol.17, 65 (1981).

[48] M. C. Gower, A. J. Kearsley, and C. E. Webb, IEEE J. Quantum Electron. QE_16, 231 (1980).

[49] P. Burlamacchi *Physics of New Laser Sources*, ed. N. B. Abraham, F. T. Arecchi, A. Mooradian, and A. Sona, Plenum Press, NY. (1984).

[50] H. Houtman, and J. Meyer, J. Appl. Phys. Vol.61, 843 (1987).

[51] R. S. Taylor, Appl. Phys. B. Vol.41, 1 (1986).

[52] J. W. Gerutsen, Appl. Phys. B. Vol.46, 141 (1988).

[53] Z. Mingchao, Chine. Phys. Lasers. Vol.14, 864 (1987).

[54] A. T. Rakhimov, and N. V. Suetin, Sov. J. Plasma Phys. Vol.13, 500 (1987).

[55] S. Lin, C. Zheng, D. Lo, J. Matsumoto, and S. Zhu, Appl. Phys. B. Vol.40, 15 (1986).

[56] D. E. T. F. Ashby, and D. F. Jephcott, Appl. Phys. Lett. Vol.3, 13 (1963).

[57] H. P. Hopper, and G. Bekefi, Appl. Phys. Lett. Vol.12, (1964).

[58] M. A. Heald, and C. B. Wharton, *Plasma Diagnostics with Microwaves*, John Wiley and sons, NY, (1965)

[59] R. C. Hollins, D. L. Jordon, and J. Coutts, J. Phys. D: Appl. Phys. Vol.19, 37 (1986).

[60] M. Hiramatsu, H. Furhashi, and T. Goto, J. Appl. Phys. Vol.60, 1946 (1986).

[61] A. De Angelis, P. Di Lazzaro, F. Garosi, G. Giordano, and T. Letardi, Appl. Phys. B. Vol.47, 1 (1988).

[62] W. D. Kimura, D. R. Guyer, S. E. Moody, J. F. Seaman, D. H. Ford, Appl. Phys. Lett. Vol.49, 1569 (1986).

[63] T. H. Johnson, and H. E. Cartland, Appl. Phys. Lett. Vol.52, 1862 (1988).

[64] J. Coutts, and C. E. Webb, J. Appl. Phys. Vol.59, 704, (1986).

[65] P. E. Dyer, and B. L. Tait, J. Phys. E: Sci. Instrum. Vol.17, 637 (1984).

[66] A. Gilardini, *Low Energy Electron Collisions in Gases*, John Wiley and sons, NY, (1972).

[67] K. Roher, and F. Linder, J. Phys. B: Atom. Molec. Phys. Vol.9, 252 (1976).

[68] L. G. Christophorou, and J. A. D. Stockdale, J. Chem. Phys. Vol.48, 1956 (1968).

[69] M. Morton, and C. H. Krugger Jr, *Partilly Ionized Gases*, John Wiley, NY, (1973).